Studies of the ATLAS Pixel Detector Module Timing with the Athena Framework

Masterarbeit
zur Erlangung des akademischen Grades
Master of Science
(M. Sc.)

dem Fachbereich Physik der
Universität Siegen

vorgelegt von
B. Sc. Michael Pontz

August 2008

Contents

Chapter 1

Introduction

1.1 Physics with the ATLAS Detector

Modern high energy physics aims for a deep understanding of elementary particles and the fundamental interactions between them. Starting in the second half of the 20th century, particle accelerators and collision experiments have become the central tools in the process of measurement.
The energy liberated in a particle collision is transformed into a multitude of new particles according to the proportionality between energy and mass, expressed by the Einstein formula $E = mc^2$. The study of all the parameters of the in- and outgoing particles probes assumptions about the inner structure of matter and the interactions at work.
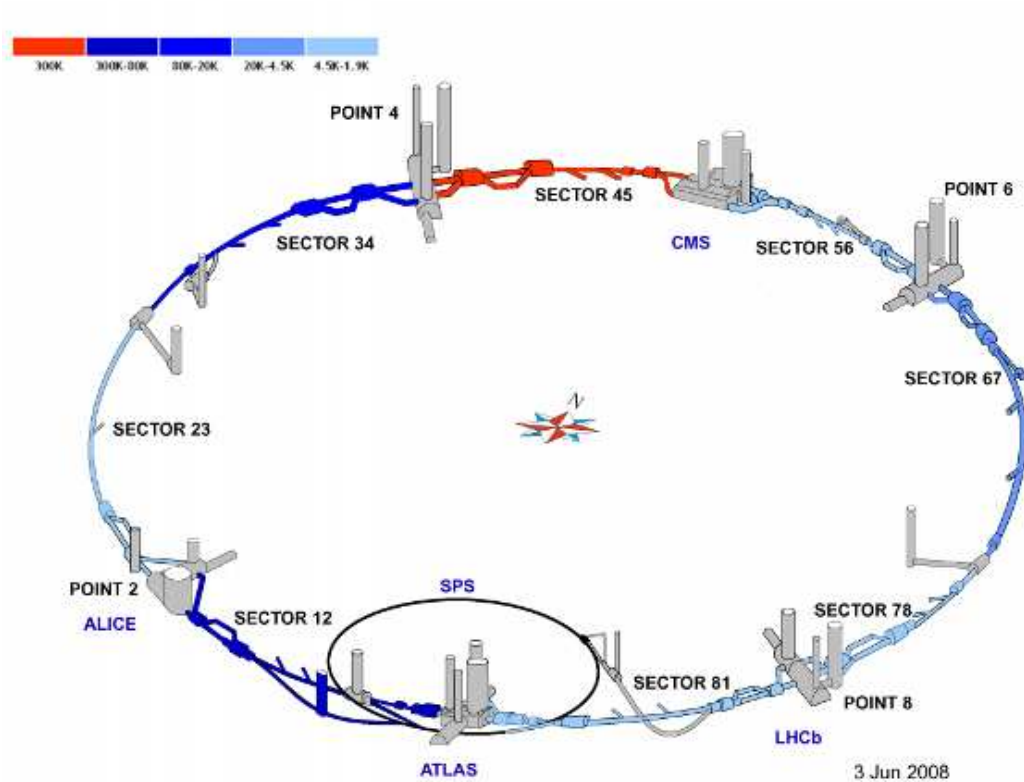
Figure 1.1: The Large Hadron Collider and the experiments at CERN [1].

At the European Organization for Nuclear Research, CERN in Geneva, an accelerator, the Large Hadron Collider (LHC), is currently being built and will probably start taking physics data in September 2008. The LHC will accelerate protons to a final energy of 7 TeV in its ring with 27 km circumference. Bunches of up to 10^{11} protons each will be accelerated in opposite directions and brought to collision every 25 ns in four interaction points. At these points, the detectors of the four experiments ALICE, ATLAS, CMS and LHCb, that are shown in Figure 1.1, are installed.

ALICE (A Large Ion Collider Experiment), CMS (Compact Muon Spectrometer) and LHCb (Large Hadron Collider beauty experiment) will not be discussed further in this thesis, whereas ATLAS (A Toroidal LHC Apparatus) is described in more detail in Chapter 2. ATLAS and CMS are the two multi-purpose detectors at LHC, LHCb is designed for B physics and ALICE will concentrate on heavy ion collisions [2, 3, 4].

The LHC will start with a few years of commissioning at low luminosity of 10^{33} cm^{-2}s^{-1}, which will then be increased to the design luminosity of 10^{34} cm^{-2}s^{-1} [5]. At the design centre of mass energy of 14 TeV, the total cross-section of pp-collisions is expected to be about $\sigma_{pp} \approx 100$ mb estimated from cosmic ray measurements and extrapolations from lower energy pp-collisions [6]. The following paragraphs shall give a brief overview over the Standard Model of Elementary Particle Physics (SM) and of the physics programme of the ATLAS collaboration. Besides, like most of the earlier experiments, ATLAS might detect unpredictable phenomena.

The Standard Model of Elementary Particle Physics

The Standard Model of Elementary Particle Physics (SM) is a theory, that describes matter as consisting of structureless fermions with spin $\frac{1}{2}$. The information given below is a brief overview of the basic statements of the theory according to [7]. The mathematical details can e.g. be found in [8]. There are two types of fermions: the leptons with electrical charge 0 or $-e$ and the quarks with electrical charges of $+\frac{2}{3} e$ and $-\frac{1}{3} e$, where e is the elementary charge.

In the SM, there are three generations of leptons, each consisting of one massive lepton with charge $-e$ and a massless neutrino ν without charge that constitute a doublet in a mathematical sense:

$$\begin{pmatrix} e^- \\ \nu_e \end{pmatrix}, \qquad \begin{pmatrix} \mu^- \\ \nu_\mu \end{pmatrix}, \qquad \begin{pmatrix} \tau^- \\ \nu_\tau \end{pmatrix}. \tag{1.1}$$

The three generations of quarks (up and down, charm and strange, top and bottom quarks), described by the SM, are arranged in the same way:

$$\begin{pmatrix} u \\ d \end{pmatrix}, \qquad \begin{pmatrix} c \\ s \end{pmatrix}, \qquad \begin{pmatrix} t \\ b \end{pmatrix}. \tag{1.2}$$

The upper component of each quark doublet carries the charge $+\frac{2}{3} e$ and the lower component carries $-\frac{1}{3} e$. Every lepton and quark has got an associated partner with the same mass and spin, but with inversed charge and magnetic moment: the antilepton or antiquark. Quarks have never been observed as free particles (unlike leptons), but always in bounded states: the hadrons. Hadrons may consist of three quarks, forming a baryon (such as n or p), or a quark and an antiquark, forming a meson (such as π or $K^\pm$). Most

of the matter in the Universe is built up of the lightest particle families, namely up- and down-type quarks and electrons.

The interactions between particles in the SM are mediated by exchange particles with integral spin, bosons, that couple to a specific charge. The SM describes the weak, the electromagnetic and the strong interaction.

The strong force interacts with all the quarks and antiquarks through massless gluons g with spin 1. The corresponding theory is the quantum chromodynamics (QCD). Quarks (antiquarks) are given colours (anticolours) and gluons are given a pair of colour-anticolour as the strong charge. Summing all colours in a hadron must lead to a neutral colour. Because of this, there must be three different colours to explain particles such as $\Delta^{--} = uuu$. Thus, eight kinds of gluons can be generated. Since the gluons carry strong charges, gluons can interact with each other, which makes the strong interaction unique amongst the other interactions.

The electromagnetic force couples to the electric charges of particles. It is mediated by the exchange of massless photons γ with spin 1. The interaction is described very precicely by the quantum electrodynamics (QED). The weak interaction is mediated by three massive gauge bosons, namely the $W^{\pm}$ and the Z^0 and may affect every particle. Since the coupling is typically about 10^5 times weaker than the coupling of the electromagnetic interaction and about 10^7 times weaker than the strong interaction, it can only be observed if these other interactions are heavily suppressed or forbidden.

In 1967/68, a combined theory of the electromagnetic and the weak interaction was presented as the electroweak interaction by S. A. Glashow, A. Salam and S. Weinberg. Encouraged by this, the search for a combined theory of all interactions is continuing.

Gravitation is the only fundamental interaction that is not included in the SM. On an atomic scale, the electromagnetic force between a proton and an electron is about 10^{38} times larger than the gravitational force, which makes the latter negligible. Massless exchange particles with spin 2, gravitons, could explain the interaction in theory, following QCD and QED, but were never detected yet.

Search for the Higgs Boson

Particle physics as it is known today can be well described with the Standard Model (see above) at scales of 10^{-18} m and particle masses up to about 200 GeV [9]. Nevertheless, the different masses of leptons and quarks violate the gauge invariance of the unextended theory and are still free parameters (six of 18 in total). Adding another scalar field, the Higgs-field to the theory, leads to three massive gauge bosons (the $W^{\pm}$ and the Z), one massless boson (the γ) and one massive scalar particle which is called Higgs boson, named after the theorist Peter Higgs [9]. This Higgs boson has not been observed yet. The mass of leptons and quarks is then produced by a Yukawa-coupling of these particles to the Higgs-field.

Experiments so far exclude values below 114.4 GeV as possible masses for the Higgs [10] and theoretical assumptions limit the mass window to 1 TeV at the most [6]. With a centre of mass energy of $\sqrt{s} = 14$ TeV, the LHC covers all possible Higgs masses [6, 9]. Therefore, the Higgs particle is very likely to be detected at the LHC, if it exists.

Precision measurements in the Standard Model

Every new experiment needs to confirm, disprove or improve existing results from former experiments. The experiments at LHC will be used to perform high statistics measurements on known particles and their interactions and therefore probe the Standard Model on the high energy frontier [9]. The high luminosity and the large centre of mass energy allow high statistics investigations on the W bosons and heavy quarks (t and b). Even at low luminosity of 10^{33} cm^{-2}s^{-1} there will be about 25000 $t\bar{t}$-pairs produced per day [4] allowing the precise measurement of the top mass and the production cross-section $\sigma_{t\bar{t}}$ as well as the study of rare decay channels.

B Physics

The emphasis in B physics is set on the study of CP-violation in the B^0-system, which is connected to the measurement of the complex phase in the Cabibbo-Kobayashi-Maskawa matrix (CKM matrix). The number of $b\bar{b}$-pairs is expected to be about 12 000 per year [4]. In order for CP-violation to take place, a complex phase needs to be inserted into the Standard Model (as a consequence of the unitarity of the CKM matrix), and at least three generations of quarks are needed. The search for a (possible) fourth family of quarks or leptons is another goal of the LHC.

Physics beyond the Standard Model

The search for one common theory for all fundamental interactions leads to theories such as Supersymmetry (SUSY), Grand Unification Theory (GUT) or string theory. Some of these predict a variety of new particles at the TeV scale and might be supported by results from the experiments at the LHC.
Furthermore, there will be searches for new gauge bosons with masses larger than the W or Z mass, new quarks, charged leptons and massive neutrinos as well as for a possible inner structure of quarks and leptons [9].

1.2 Basic Principles of Semiconductor Detectors

This thesis presents an analysis of data recorded with the ATLAS Pixel Detector. Therefore, the basic principles that allow for the use of silicon as the active detector material, and the basic physics effects of particles interacting with matter are presented in this section. Particles passing through matter lose energy through inelastic scattering with electrons of the atomic electron shell, elastic scattering with the atomic nucleus, bremsstrahlung in the Coulomb field of an atom, Cherenkov radiation and nuclear reactions [11]. High energetic electrons and positrons lose their energy mainly through bremsstrahlung due to their low masses. For heavier particles, inelastic collision and therefore ionisation and excitation dominate the energy loss. The mean energy loss (not considering bremsstrahlung and nuclear reactions) is described by the Bethe-Bloch formula and illustrated in Figure 1.2. The curve shape is dominated by a $1/\beta^2$ increase at low energies. The minimum can be calculated at $\beta\gamma \approx 3.5 \Leftrightarrow \beta \approx 0.96$ and is called the minimum of ionisation. Particles with a momentum at that minimum value are minimum ionising particles (MIPs). For higher energies, dE/dx increases logarithmically and therefore very little at high momenta,
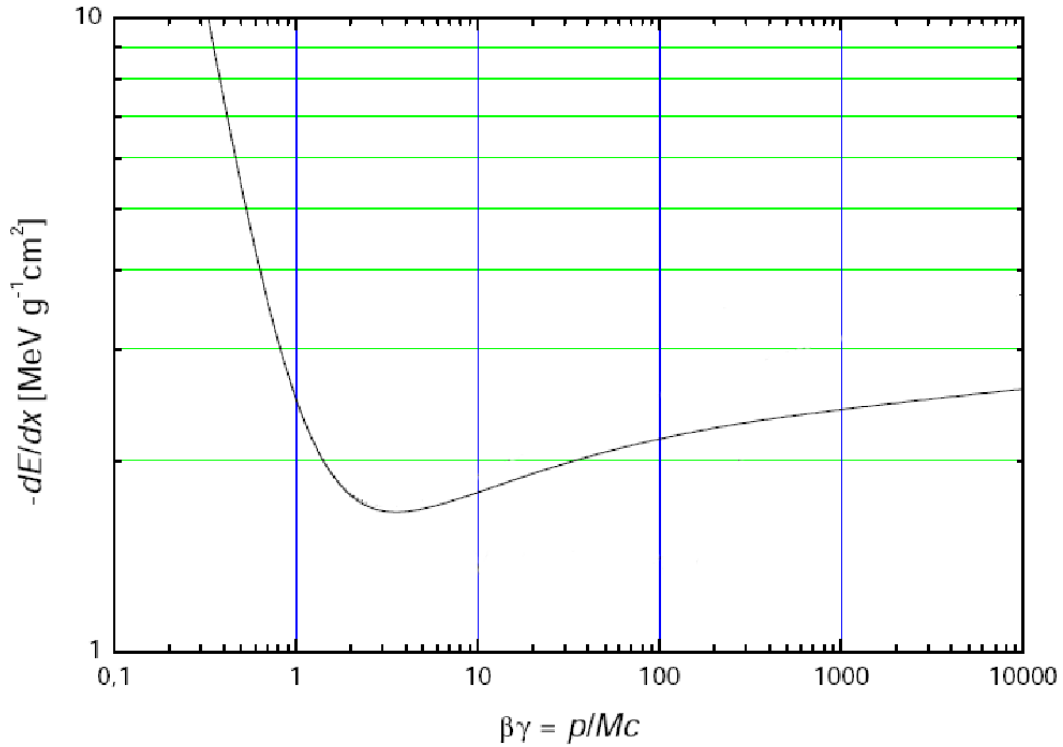
Figure 1.2: Energy loss of heavy charged particles as a function of $\beta\gamma$ in silicon as described by the Bethe-Bloch formula [12].

reaching the Fermi plateau due to the density effect [11].

In thick absorbers (in terms of the multiplicity of ionising processes), the energy loss is Gaussian-distributed. In thin absorbers, the probability of high energy transfers decreases and the curve shape of the energy loss becomes Landau-distributed, since energy transfers at the low energy end are more likely to take place.

In semiconducting material, ionisation leads to the creation of electron-hole pairs alongside the trajectory of the traversing particle. To avoid a recombination of the pairs, an external electric field separates electrons and holes and attracts them to the anode and cathode. Since the mean energy loss can be assumed as constant in thin absorbers and for high energetic particles (see Section 1.3), the number of liberated charges is proportional to the deposited energy and can be detected with charge sensitive amplifiers.

Semiconducting materials like silicon are very much suited for the use as particle detectors, which provide exact vertex and track information. Some properties of silicon leading to this primacy shall be briefly listed here. The low ionisation energy of 3.6 eV causes a traversing particle to create a large number of electron-hole pairs and it therefore provides a high charge signal to the amplifiers. The high density of silicon $\rho_{Si} = 2.33$ g/cm^3 allows for the construction of thin detectors and the high mobilities of electrons and holes in silicon permit charge collections at high rate. Furthermore, the replacement of a comparatively small number of silicon atoms in the lattice structure with impurities is feasible (doping techniques) and offers a possibility to change the electrical properties of the sensor material.

Not least, the use of silicon is widespread in consumer electronics and permits to combine sensor and electronics directly and to have large-scale productions at affordable expenses. Although custom designs for sensor and readout chips were developed for the ATLAS detector, the knowledge from consumer electronics could be used.

Nevertheless, pure silicon cannot be used as a particle detector yet, since the amount of electron-hole pairs produced by thermal excitation is at the signal level. The (intrinsic) density of electrons in pure silicon can be calculated with the Fermi-Dirac statistics. To manipulate this electron density and to increase the signal-to-noise ratio, doping techniques need to be performed. Pentavalent materials, replacing silicon atoms, lead to n-type doped material. The additional electrons brought into the lattice structure contribute to the conductivity. Trivalent impurities inserted into the silicon bulk result in a p-type doped material with additional holes.

A junction between p- and n-type material lets free electrons diffuse towards the p-material and free holes towards the n-material. Holes then capture electrons from the n-side. The ionised donator atoms at the junction form a contact potential, that attracts the free charges contrary to the diffusion processes. Thermal equilibrium is reached at 0.7 V in silicon. Now, no mobile charge carriers exist any more within a depletion zone. Electron-hole pairs, that are created within this depletion zone, will be separated by the external electric field and give a clear signal to the connected electronics. Thus, the depleted region is the drift volume and can therefore be understood as the active region of this type of particle detector. Applying an external positive (high) voltage to the n-doted part of the pn-junction (reverse-bias mode) leads to an enlargement of the depletion zone to a possible size of up to 1 mm [13]. Such a thick active detector layer provides a high signal-to-noise ratio. On the other hand, tracking detectors need to have as little mass as possible in the overall detector volume in order to avoid an energy loss of passing particles and multiple scattering processes. In the ATLAS Pixel Detector, a compromise between these two opposites was found with a sensor thickness of 250 μm (see Section 2.2.1).

Due to the close position to the interaction point, the ATLAS Pixel Modules will be exposed to high radiation. This will lead to radiation damage in the sensor material. The effects on the doping are well understood and the design is prepared for a type inversion of the n-type material in the sensor layer (see Section 2.2.2).

1.3 Cosmic Rays

This thesis mainly contains an analysis of test run data, that were taken by a particular part of the ATLAS Pixel Detector (see Section 2.3). This test run recorded cosmic particles passing through the detector. For that reason, it is required to know which kind of particles are expected to arrive at ground level. A short introduction into the physics of cosmic rays is given in this section.

Ionising cosmic radiation was discovered in the early 20th century when it became clear from balloon experiments, that there is a part in the ionising radiation, that grows stronger with increasing altitude.

Cosmic radiation is produced in sources in and beyond our Galaxy. These sources generate primarily protons and electrons but as well every other charged nuclei. The primary particles are accelerated and start to propagate through space. It is also possible, that they interact within the source, producing a number of secondary particles, which start propagation then. Unstable secondary particles are likely to decay into stable particles such as photons ($\pi^0 \rightarrow \gamma\gamma$) or neutrinos ($\pi^+ \rightarrow \mu^+\nu_\mu$). Fractions of both, the primary and the secondary radiation, can reach the Earth.

The description of the charged components of the primary cosmic particles, that reach the atmosphere of the Earth, is emphasised in this section. With 85%, protons form the largest fraction of these cosmic rays, followed by α-particles (12%) and heavier nuclei with $Z \geq 3$ (3%). The sources, the chemical composition of high-energy cosmic rays ($> 10^{25}$ eV) and the acceleration mechanisms are still under study.

Figure 1.3 schematically illustrates the processes that lead to a cosmic shower originating from an incoming proton. This schematics already shows, that the main part of the shower reaching the surface consists of muons. The processes involved are discussed below.

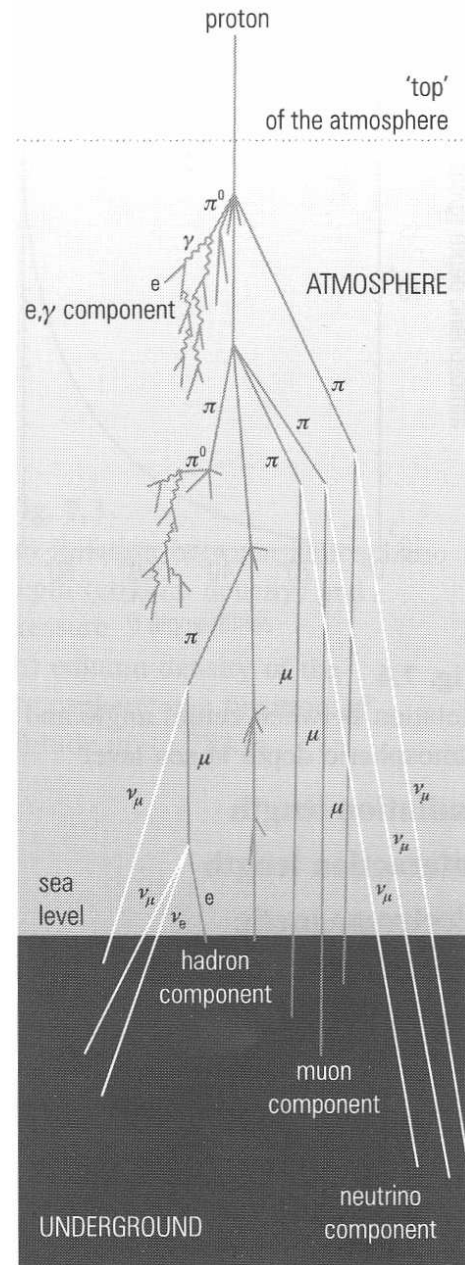Figure 1.4 quantitatively illustrates the momentum spectra of protons and muons at var-

Figure 1.3: Transformation of primary cosmic rays in the atmosphere [11].

ious altitudes in the atmosphere. At each altitude, the number of muons exceeds the number of protons. As can be read off from Figure 1.5, the muon flux at sea level is $\Phi_\mu \approx 10^{-2}$ 1/(cm^2 s sr) and thus it is two orders of magnitude higher than the proton flux.
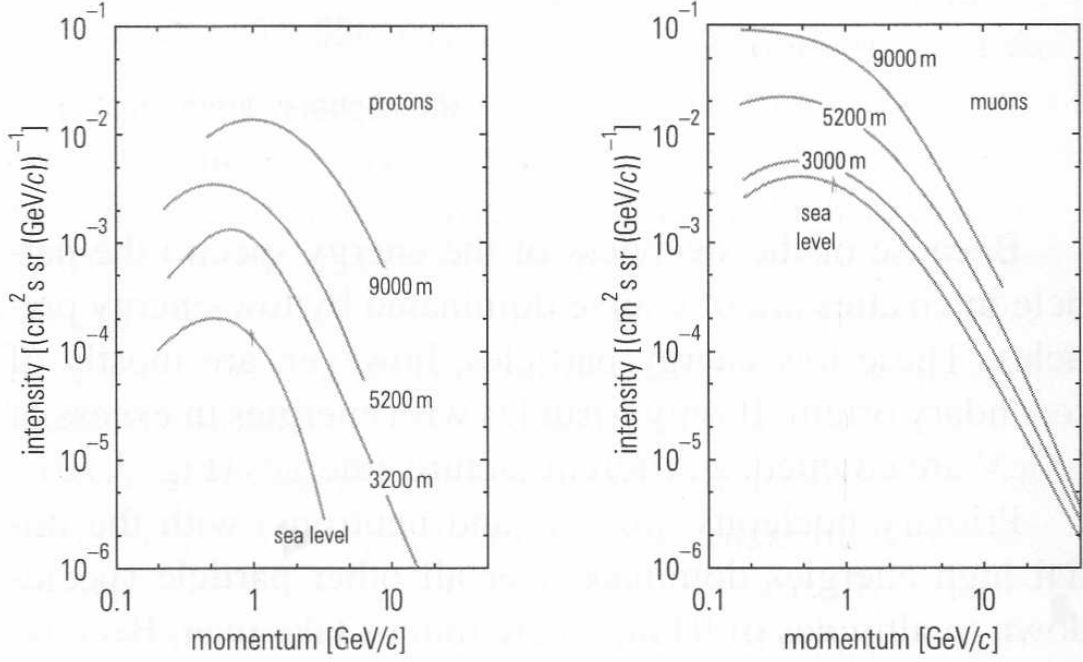

Figure 1.4: Momentum spectra of protons (left) and muons (right) at various altitudes in the atmosphere [11].

The radiation length is introduced as a density independent unit for the average distance that an electromagnetically interacting particle can travel in matter due to its lifetime. It is defined as the distance of travel through the material, in which the energy of a high-energetic electron is reduced by a factor of e by bremsstrahlung. The radiation length of photons and electrons in air is $X_0 = 36.66$ g/cm^2. The characteristic collision length for hadrons in matter is the interaction length $\lambda = 90$ g/cm^2. Since the atmospheric depth is about 1 000 g/cm^2 at sea level, it means, that practically no primary cosmic particle will make it through the whole atmosphere. Instead, the primary particles will interact in the atmosphere and initiate electromagnetic and hadronic cascades already in the 100 mbar layer (about 13 km in altitude). Particles created in these showers are the secondary particles. Pions as the lightest hadrons will be contained in nearly every hadronic decay. Kaons are produced at 10 % of the pion rate. These light hadrons may initiate further interactions or decay dependent on their energies. Neutral pions decay into two photons with a branching ratio of nearly 99 %. These photons contribute to the soft component of the cascade and will easily be absorbed by the atmosphere. Practically all charged pions (more than 99.9 %) decay into a muon and a muon-neutrino via the leptonic channel:

$$\pi^+ \rightarrow \mu^+ \nu_\mu \text{ and } \pi^- \rightarrow \mu^- \bar{\nu}_\mu \ . \tag{1.3}$$

About two third of the charged kaons (63.4 %) also decay into these muonic channels. The
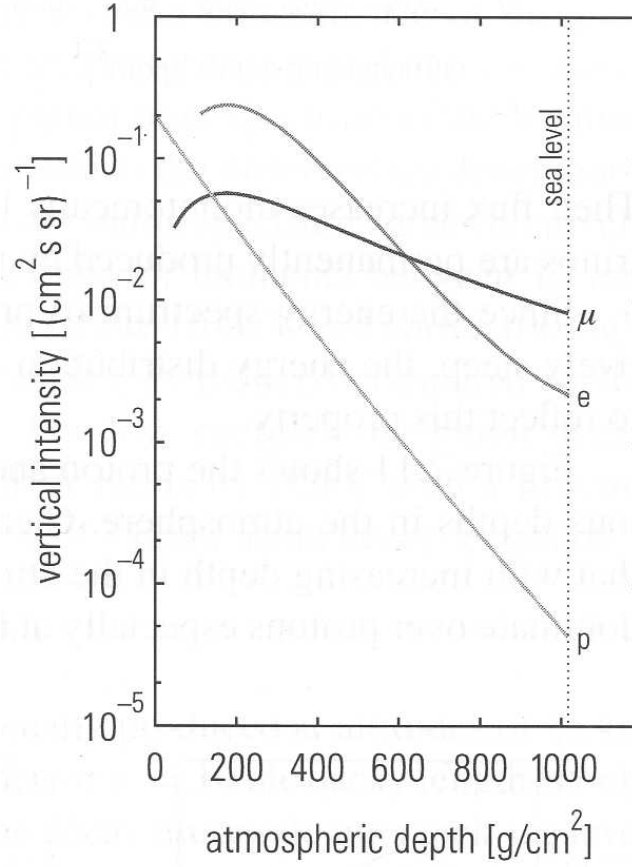
Figure 1.5: Particle composition in the atmosphere as a function of atmospheric depth [11].

muons created can themselve decay via $\mu \rightarrow e\nu_\mu \bar{\nu}_e$ and the decay products contribute to the soft components of the shower. High-energetic muons however may reach ground level [11].

The energy loss by ionisation and excitation of high-energetic charged particles (like muons, protons or nuclei, not electrons) passing through matter is described by the Bethe-Bloch formula (see Figure 1.2). It reflects the mean value of the energy loss. This loss is distributed around the most probable value by a Landau distribution with a tail to high energies (see Section 1.2). The total energy loss of cosmic muons in the atmosphere is due to ionisation, direct production of e^+e^- pairs, bremsstrahlung and photonuclear interactions. The total energy loss of cosmic muons in matter can be expressed as (see Figure 1.2 for high momenta):

$$-\frac{dE_\mu}{dx} = a + bE_\mu \; , \tag{1.4}$$

with the ionisation energy a and the fractional energy loss bE_μ of the three radiation processes mentioned above. For small energies E_μ ($a \gg bE_\mu$), the ionisation process dominates the energy loss. In the atmosphere, Equation 1.4 then becomes a constant loss of:

$$-\frac{1}{\rho} \cdot \frac{dE_\mu}{dx} \approx 1.82 \ \frac{\text{MeV}}{\text{g/cm}^2} \ . \tag{1.5}$$

For all materials with $Z/A \approx 0.5$, a constant energy loss of $2 \ \frac{\text{MeV}}{\text{g/cm}^2}$ approximately holds [13], which will be used in Section 2.2.2 and 3.1.1. The lateral spread of a cosmic particle shower is determined by multiple scattering processes of electrons and positrons in electromagnetic cascades and by the transverse momentum of the primary particle in hadronic cascades. To summarise, besides the hadronic and the soft component of a cosmic particle shower, high-energetic minimum ionising muons reach the Earth, with the constant energy loss in matter as described in Equation 1.5. The mean energy of these muons at the ground is approximately 4 GeV and the flux can be estimated at $1 \ \text{cm}^{-2}\text{min}^{-1}$ for muons with momentum above 1 GeV for horizontal detectors [6].

1.4 Scope of the Thesis

Once the LHC is running with full performance, there will be a proton-proton bunch crossing every 25 ns. In this situation, due to the constraints of the electronics, the Pixel Detector (see Section 2.2.2) will not allow for reading out more than the data assigned to one bunch crossing any longer. Nevertheless, pixel hits from the same event can be assigned to different bunch crossings for several reasons: e.g. a particle passing a Pixel Module in the barrel part of the detector has to travel a shorter way than a particle passing one of the endcaps. This will result in different time of flights. The electronics then may lead to different transit times of signals for each module. Also, the cable lengths differ for modules in different regions of the detector. Furthermore, every Pixel Module and, to be precise, every single pixel of a module, can be tuned separately and differently in terms of the Time Over Threshold signal (see Section 2.2.2). As a feature of the Front End electronics of a Pixel Module, the time between a particle passage through the sensor and the signal generation in the read-out electronics is dependent on the energy deposited in the sensor (timewalk, see Section 2.2.3) and may also lead to a wrong assignment. For particles, that deposit very little energy in the pixel sensor, the electronics will take longer to create a signal than for particles that liberate a larger number of charges in the sensor. Although the Pixel Modules offer a method (implemented in the hardware) to assign low signal values to both the current and the last bunch crossing at the expense of a higher data rate (hit-doubling), this feature will probably not be used, since it has not been tested sufficiently until now [14]. In case of cosmics data, there is no correlation between the moment of the transit of a particle and the 40 MHz clock, that drives the modules, unlike for *pp*-data. Cosmic particles hit the detector at any time within the 25 ns of a bunch clock interval.

In summary, different modules may assign concurrent hits to different bunch crossings. In order to assign as many hits as possible to the correct bunch crossing, it is necessary to calibrate a module in a way that high-charge signals, which do not suffer from timewalk, rise at the very beginning of a 25 ns readout window. This is what is called timing calibration of the Pixel Modules in this thesis. A perfect timing of all modules would minimise the number of hits, that are assigned to the wrong bunch crossing. The aim of this study is to determine the exact position of the high-charge signals within the nominal 25 ns with

a resolution in the order of 1 ns and compare it to the results from earlier studies [15].

In December 2006, one endcap of the Pixel Detector was operated in one of CERN's laboratories. It was used for commissioning and testing purposes but also cosmic data were recorded [16] (see Section 3.1.1). The low hit rate of cosmic particles allowed for reading out the full data assigned to 16 consecutive bunch crossings in the endcap cosmic run. This ensured, that all particle tracks were recorded and no hit signal was lost. Thus, also data from mis-timed Pixel Modules are included and could be analysed for a later correct adjustment of the timing.

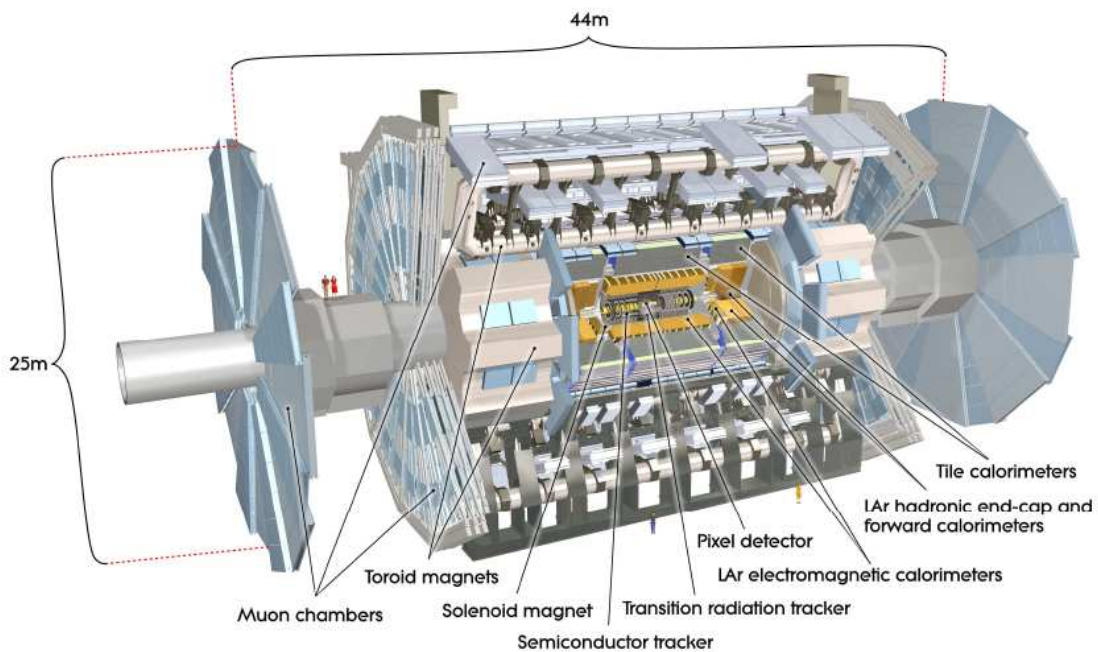# Chapter 2

ATLAS Detector

Figure 2.1: The ATLAS detector [17].

The ATLAS detector is the largest of the four detectors at the LHC. With a length of about 44 m, 25 m diameter and an overall weight of about 7 000 tons, it nearly fills the whole cavern that was excavated 92 m below ground.

Figure 2.1 shows a schematic view of the detector. It reflects the typical layout of a collision experiment with an almost total solid-angle coverage around the collision point. The Inner Detector's purpose is the reconstruction of tracks and decay vertices of charged particles. The electromagnetic and hadronic calorimeters measure the energy of particles originating from collisions and the outer spectrometer is built for the detection of penetrating muons [18, 17].

The following chapter describes the different detector parts and their functions in more detail.

2.1 Coordinate System

Within ATLAS, the coordinate system is defined such, that its origin is located in the nominal interaction point inside the detector. The z-axis points anti-clockwise with respect to the LHC ring, the x-axis is defined as pointing towards the centre of the LHC ring, leaving the y-axis to point upwards to form a right-handed system. The azimuthal angle ϕ is measured perpendicular to the z-axis and with respect to the x-axis. The polar angle θ is the angle of any vector in the coordinate system with respect to the z-axis. With $\eta = -\ln \tan \frac{\theta}{2}$, the pseudorapidity is defined as another scale for the polar angle, ranging from $\eta(0) = +\infty$ to $\eta(\pi) = -\infty$ with the advantage, that differences $\Delta\eta$ in the pseudorapidity form a Lorentz-invariant quantity.

2.2 Inner Detector

The ATLAS Inner Detector consists of three subdetectors as shown in Figure 2.2. Starting from the inside, these are the Pixel Detector, the Semi Conductor Tracker (SCT) and the Transition Radiation Tracker (TRT). Their purposes are to provide precise track and vertex information whilst relatively little mass is used to minimise the effect of multiple scattering of particles in the detector volume.

The Pixel Detector is described in more detail in Section 2.2.1. The SCT consists of four double layers of silicon strips, 80 μm $\times$ 12 cm in size. The TRT consists of 36 layers of straw tubes with 4 mm diameter. By using two different thresholds for the recording of hits, the TRT can distinguish signals from electrons and photons, since only photons from transition radiation pass both thresholds [18]. All three subdetectors are contained in a magnetic field of 2 T produced by the Central Solenoid. Including the information from the Pixel Detector, the Inner Detector provides up to about 40 space points with high resolution along a typical track.
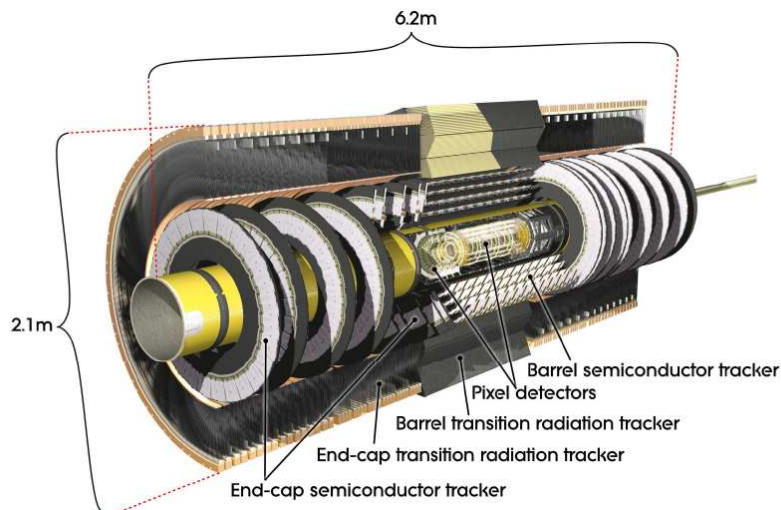

Figure 2.2: The Inner Detector of ATLAS [17].

2.2.1 Pixel Detector

The innermost subdetector of the ATLAS experiment is a silicon pixel detector (see Figures 2.2 and 2.3). Its aims are high precision tracking of particles, and taking advantage of this, exact primary and secondary vertex reconstruction. With about 80 million channels, it provides about half of all the readout channels of the ATLAS detector.

Since the detector was inserted into the ATLAS system in June 2007, it has not been accessible. Because this was known beforehand and because a selection of the modules for the different locations in the detector had to be made, its components were studied very precisely during production and assembly. Furthermore, cosmics data were taken using one endcap of the detector at CERN's laboratories [16]. Data resulting from these runs are studied in Chapter 3 of this thesis with respect to the Pixel Module timing.

The Pixel Detector consists of three coaxial cylindrical barrel layers at radii of 50.5, 88.5 and 122.5 mm from the beam axis and three discs each in the forward and backward directions. The distance of these discs in the z-direction from the nominal point of collision is 495, 580 and 650 mm either side. With this layout, the detector provides at least three space points per charged particle track and event in the region of $|\eta| \leq 2.5$.

A B-meson, that is produced in a collision, will decay, due to its lifetime, at a secondary vertex, separated from the point of collision. The reconstruction of both the primary and the secondary vertex requires precise track information from as close as possible to the beam pipe. This need is satisfied by the innermost barrel layer, which is the B-Layer [19]. The outer layers are Layer 1 and Layer 2. Each layer consists of carbon-fibre staves, which are equipped with 13 Pixel Modules each. The Pixel Modules are the active detector elements and are described in Section 2.2.2. In order to avoid dead areas at the edges of the modules and to form overlap regions, the modules are inclined by 0.9° in z-direction and by a tilt angle of 20° (see Figure 2.3). These overlap regions can also be used for alignment studies. In total, the B-Layer consists of 286 modules, Layer 1 of 494 and Layer 2 of 676 [5].

Within one operational year (10^7 s) at high luminosity of 10^{34} cm^{-2}s^{-1}, the Pixel Detector will be radiated with over 300 kGy of ionising radiation at the B-Layer. This corresponds to a neutron equivalent dose of over 5×10^{14} neq (where 1 neq = 1 neutron with 1 MeV per cm^2) [20]. Due to the high radiation, that the B-Layer has to withstand, being close to the interaction point, its lifetime is expected to be approximately three years at low luminosity of 10^{33} cm^{-2}s^{-1} plus one year at high luminosity of 10^{34} cm^{-2}s^{-1}. For the following period, a B-Layer replacement is discussed. Layers 1 and 2 are expected to function for up to 10 years.

Like the other support structure elements, the staves are made of carbon composite material. The use of carbon minimises the amount of passive material in the detector and also provides high stiffness and a near zero thermal expansion coefficient [21]. Integrated aluminium cooling pipes mounted under each stave guarantee a constant temperature for the Pixel Modules. Evaporative cooling is performed with chlorofluorocarbon C_3F_8. Two staves are grouped together to form a bi-stave as the smallest mechanical unit in the barrel part [21].

The discs are named as Disc 0, Disc 1 and Disc 2 further on in this thesis. The smallest mechanical unit here is a sector with three modules mounted on the front and three on the back forming overlap regions to cover all ϕ. A disc carries 48 modules in total.

The Pixel Detector is enclosed by a support tube that ensures a complete environmental

isolation from the rest of the ATLAS system. This way, all modules are kept in an optimal environment with respect to temperature and humidity as studied during production and assembly tests at all times. Furthermore, the support tube includes the beam pipe and the first three metres of services (power supply lines, fibres for data transmission and cooling lines) on each side [21].
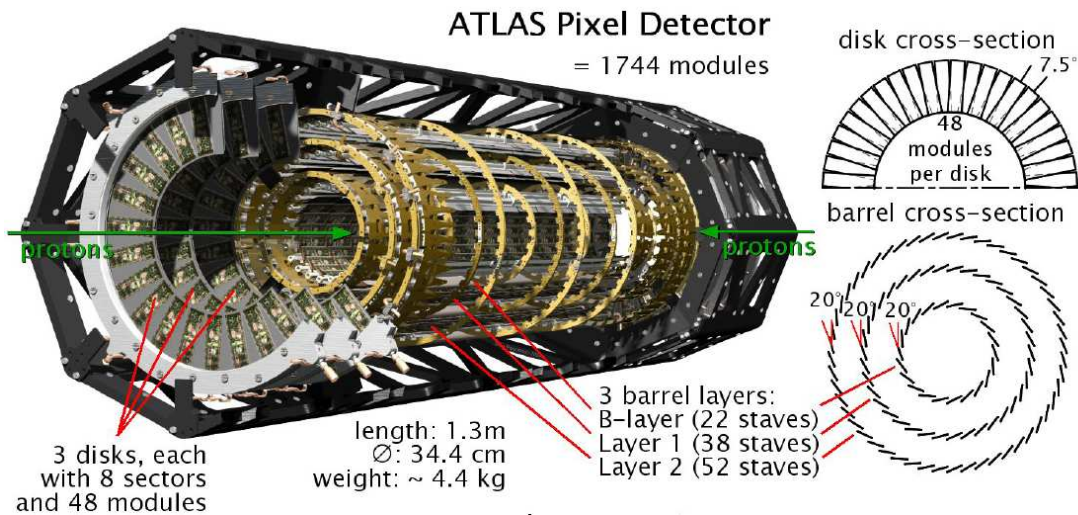

Figure 2.3: The Pixel Detector of ATLAS [17, 22].

2.2.2 Pixel Module - Mechanical Assembly

Each Pixel Module consists of three parts: the flex hybrid, the pixel sensor and the Front End electronics (see Figure 2.4). A Pixel Module has to withstand high radiation at a working temperature of about -7 ° C and also needs to be as thin as possible to avoid multiple scattering in the detector volume. A detailed description of the Pixel Module can be found in [5]. In this thesis, the basic parts will be introduced to give an insight into the functionality of a Pixel Module.

Flex Hybrid

The flex hybrid is a 50 μm thick flexible circuit board. As can be seen in Figure 2.4, the flex hybrid carries passive SMD components, a radiation hard NTC to monitor the temperature, the active Module Control Chip (MCC) and a pigtail as the connection to the off-detector electronics and the readout chain behind.
The flex hybrid is fixed to the MCC and the stave structure (Thermal Management Tool TMT) with thermally conductive glue. The electrical connection to the Front End chips (FEs), the pigtail and the Module Control Chip (MCC) is achieved with wirebonds (diameter 25 μm), that are attached to the pads by ultrasonic soldering. In order to avoid weak wirebonds breaking, because of resonance excitation in the magnetic field of the Central Solenoid, each connection uses several wires of different length.
Each module is supplied with two low voltages and one high voltage. The low voltages for

the digital and the analogue electronics are filtered by capacitors and then fed down to the FEs.

2.2.3 Pixel Module - Readout Chain

A particle, passing the sensor material, liberates charges (see Figure 2.5). These free charge carriers are separated by an electric field and led into the amplifying electronics of the Front End chips. After the digitisation of the signal, the data from all Front Ends, belonging to one Pixel Module and associated to one event, are passed on by the Module Control Chip (MCC) after a trigger request arrived. The data is then fed into the off-detector Readout Buffers (ROBs) mainly via optical fibres, processed by further trigger algorithms and possibly written to storage devices [17]. Signal generation and the readout chain up to the MCC are described in the following section. Additionally, the dependence of the time behaviour of the output signal on low-energy deposits (timewalk) is introduced. The timewalk constitutes a basic feature of the analysis presented in Chapter 3 of this thesis.

Pixel Sensor

The Pixel Detector needs to provide a spatial resolution of 12 μm in r-ϕ- and of 100 μm in z-direction. These requirements can be satisfied by a basic pixel unit with a typical size of $50 \times 400 \ \mu\text{m}^2$. The pixels are arranged in a matrix consisting of 18 rows and 164 columns. There are extended pixels of $50 \times 600 \ \mu\text{m}^2$ in the boundary regions between two adjacent Front End chips to avoid dead areas in the detector. Each pixel in the pixel sensor works as a diode driven in reverse-bias mode as described in Section 1.2. It is made of high purity n^+np^+ type material, which has been chosen to ensure its functionality after irradiation. Irradiation will lead to a type inversion of the n-layer to p-doped material. Before type inversion, the depletion zone starts to grow from the p- to the n-material with increasing bias voltage. Afterwards, the depletion zone will grow from n to n^+. Since the patterned structure is located at the n^+-side, it will be surrounded by depleted silicon in either case [23]. Figure 2.5 schematically illustrates a single pixel in profile view and a supervision on an array of pixels. The sensor material is directly connected to the first part of the readout electronics by a small metal bowl, the bump bond.

The sensor material is 250 μm thick. On the one hand, it needs to be thick enough to provide a high charge signal to the first amplifier of the readout chain, which is charge sensitive. On the other hand, it needs to be thin enough to reduce the effect of multiple scattering of particles in the Pixel Detector. In order to calculate the number of electrons liberated by a minimum ionising particle (MIP), Equation 1.5 has to be used, taking into account the density of silicon $\rho_{\text{Si}} = 2.33 \ \text{g/cm}^3$ and its ionisation energy $I_{\text{Si, ion}} = 3.6 \ \text{eV}$. The mean number of liberated electrons is:

$$N_e = \frac{dE_\mu}{dx} \cdot x_{\text{sensor}} \ / \ I_{\text{Si, ion}} = 106 \ \text{keV} \ / \ 3.6 \ \text{eV} \approx 29\,500.$$

Scaling this with a factor of 0.7 in order to get the most probable value in a Landau-distrubution yields $N_{e, \ m.p.} \approx 20\,000$.

Front End Electronics

The first elements of the readout electronics are 16 Front End chips (FEs) per module, that are mounted directly to the sensor (see Figures 2.4 and 2.5). Each of the 16 FEs houses 2880 pixel unit cells. A pixel unit cell covers one pixel in the sensor material and it therefore also has a typical size of $50 \times 400 \ \mu m^2$. The electrical connection was achieved by bump bonds between the surfaces of the two elements. Two techniques were employed: one using solder bump bonds, the other one using indium bump bonds [5]. Each of the pixels in the sensor is connected to a pixel unit cell in the FE chip by one bump bond.

The power consumption of a Pixel Module is 35 mA at 1.6 V (560 mW) for the analogue part and 75 mA at 2.0 V (150 mW) for the digital part. The components of such a unit cell are schematically shown in Figure 2.6. Electrons, that are liberated in the sensor material, will firstly build up a voltage over the pixel gap, which already leads to a current. Secondly, the liberated charges will drift to the anode of a pixel (diagram (a) in Figure 2.7), pass the bump bond material (displayed by the black disc in Figure 2.6) and then be amplified by the first analogue charge-sensitive amplifier. The signal of this amplifier loads a 6 fF capacitor, that is then discharged by a constant feedback current. The outgoing signal is fed into a second-stage amplifier, followed by a differential discriminator (see Figure 2.6). The charging and discharging of the feedback capacitor forms an almost triangular pulse (diagram (b) in Figure 2.7) with its amplitude proportional to the charge collected in the sensor and therefore proportional to the deposited energy. The steepness of the falling edge of the pulse can be tuned via a local Feedback Digital to Analogue Converter (FDAC, 3 bit), that regulates the feedback current. The threshold of a pixel unit cell can be adjusted by a FE-wide Global DAC (GDAC, 5 bit) and more finely by a pixel-specific Trim DAC (TDAC, 6 bit). All adjustments affect the width of the discriminator output signal (diagram (c) in Figure 2.7), which is the Time Over Threshold (TOT) and which is counted in 40 MHz clock cycles (or Bunch Clock Intervals BCIs).
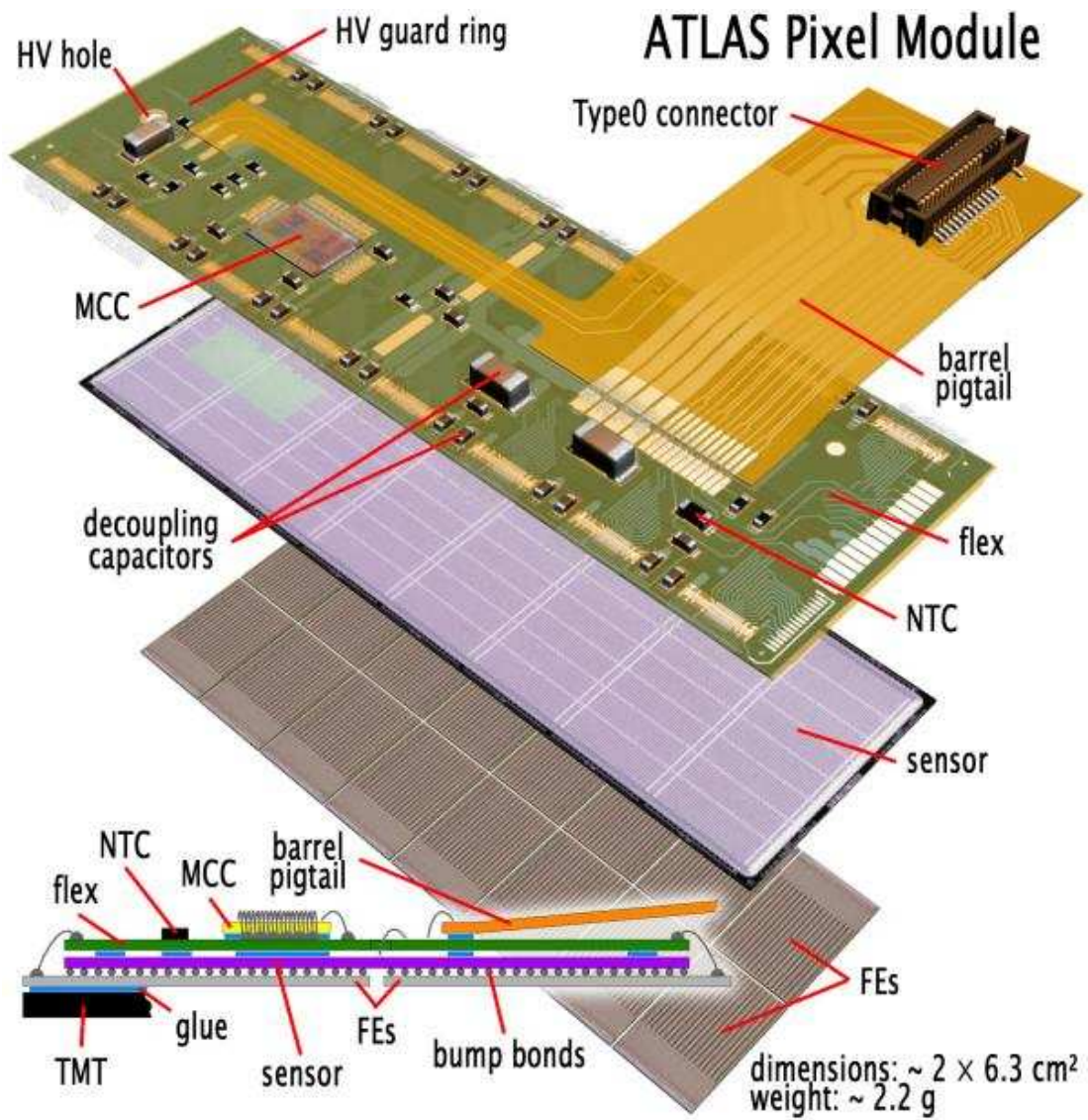
Figure 2.4: Exploded and cross-sectional view of an ATLAS Pixel Detector Pixel Module [17].
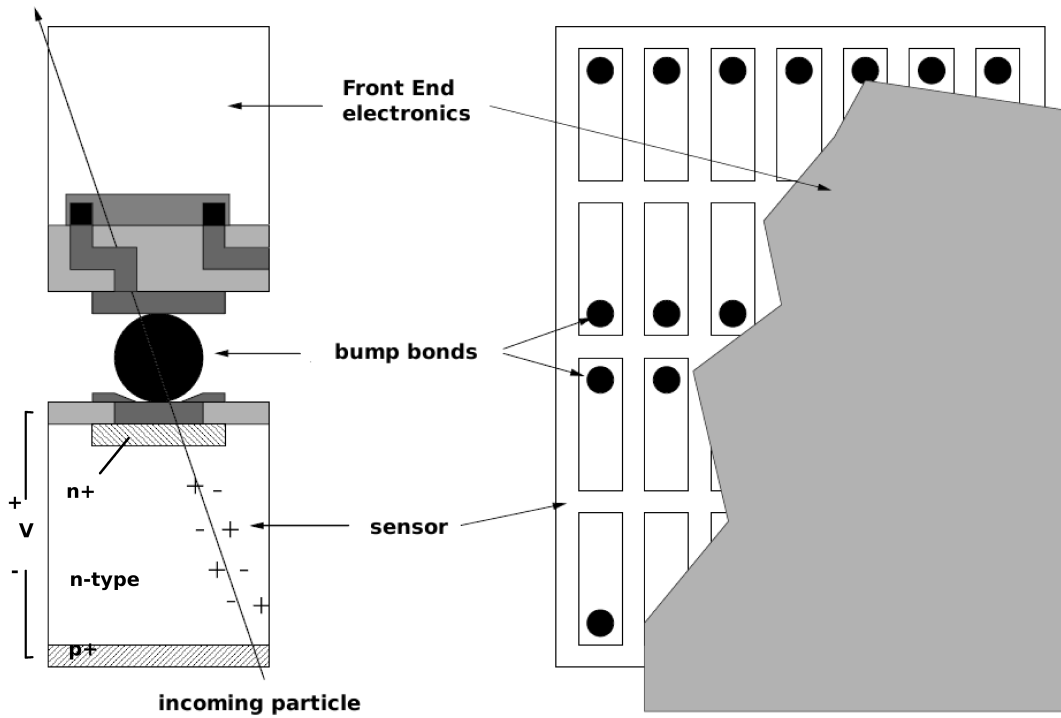
Figure 2.5: Schematic profile view of a pixel and the Front End electronics connected by a bump bond (on the left side) and a supervision on an array of pixels (on the right side). A particle passing through the sensor material will liberate charges, that are then separated by an externally applied electric field and led into the Front End electronics through the bump bond [23].
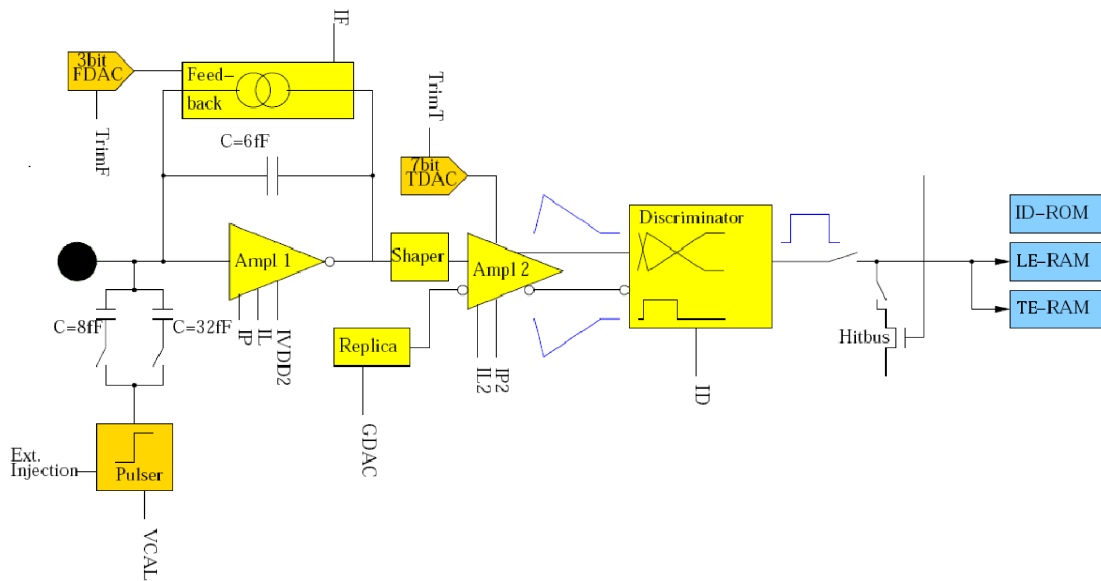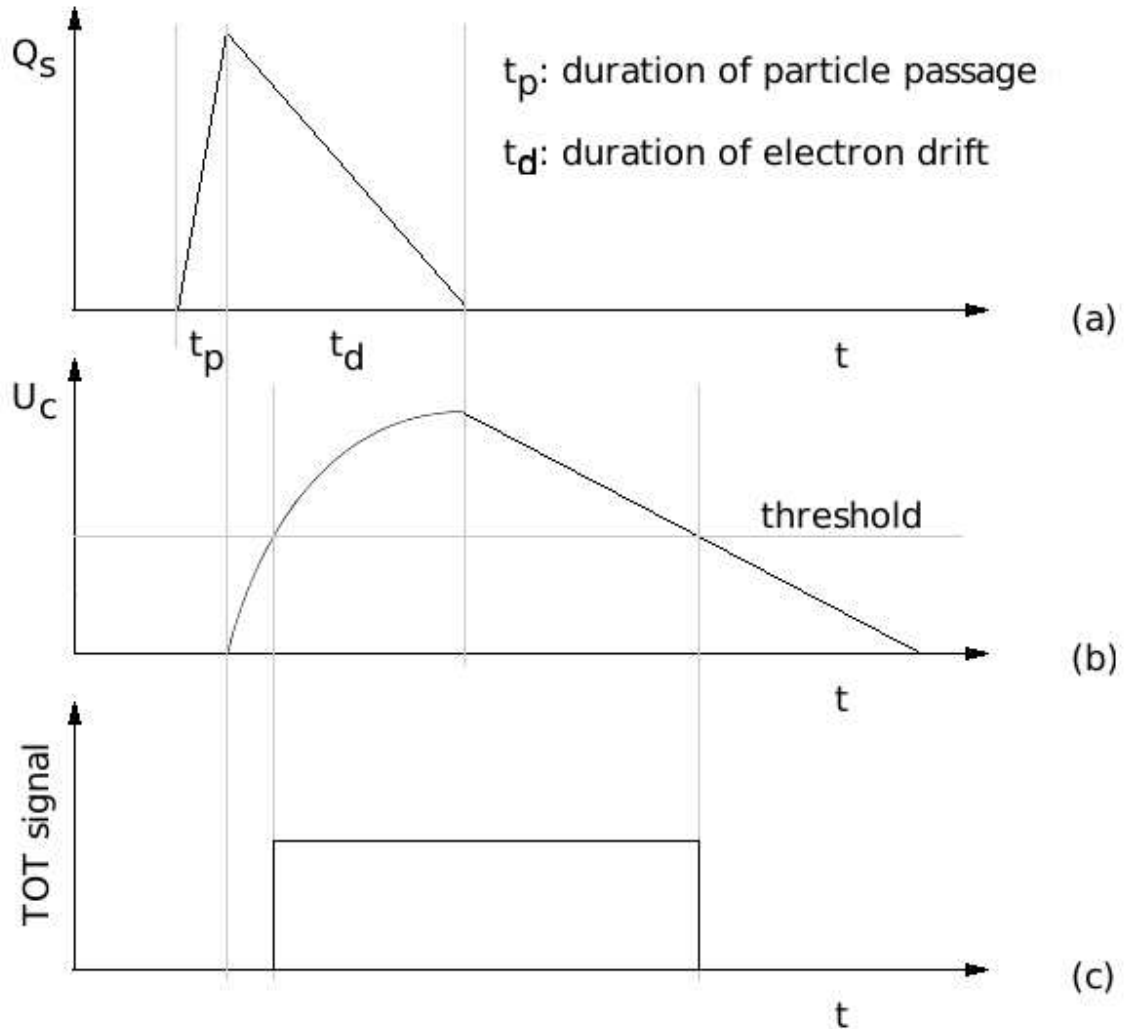

Figure 2.6: Schematics of a pixel unit cell [19].

Figure 2.7: Schematics of the signal generation process. The topmost diagram (a) shows the amount of liberated charge Q_s in the sensor. It increases for the time t_p, in which a particle creates electron-hole pairs while passing the material. It decreases for the time t_d, in which the electrons drift to the anode and are being absorbed. Diagram (b) illustrates the resulting voltage U_c at the capacitor, which is loaded as long as there are electrons left to drift. The capacitor is discharged with a constant current. This pulse is fed into the discriminator. As long as U_c is above the threshold, a TOT signal is uphold (diagram (c)).

Due to the triangular pulse shape, that is fed into the discriminator, and the constant feedback current, combined with the proportionality between separated charge and deposited energy, the width of the TOT signal is proportional to the energy deposited in the sensor material. Triggered by each leading and trailing edge of a TOT signal, the cell ID (row number) and a time stamp are stored (LE-RAM and TE-RAM in Figure 2.6). The latter is provided by a Gray-coded 8-bit counter. The counter is driven by the 40 MHz bunch crossing clock and therefore gives unique timing information for every $255 \; (\hat{=} \; 8 \; \text{bit}) \times 25$ ns $= 6.4 \; \mu$s. Within that time, the data need to be requested by the trigger system or will be deleted, since the timing information would become ambivalent.

The pixel cells are grouped together in nine double columns with 160 rows per column. One double column is connected to 64 End Of Column (EOC) buffers. The length of the TOT signal is given by the difference between the timestamps assigned to its edges. The signal is processed by a pipelined TOT processor and written to one of the EOC buffers with the ID of the row in which it originated. The processor may reject TOT signals below a certain value or even assign short TOT signals to the previous bunch crossing.

The transfer of the signal leaves the pixel free for the next measurement and the data in the EOC buffer will remain there until a trigger signal arrives or until the latency time expires. If the former happens and the leading edge timing matches the trigger timing information, the data will be forwarded to the readout chain. The time comparison is done with a second clock signal delayed with respect to the first one by a programmable latency. The second clock signal is used to monitor the age of the hits in the EOC buffers. If there is no matching between hit and trigger, the hit is deleted. A FE chip may process up to 16 trigger decisions in parallel by using a 16-word trigger memory (First In First Out type, FIFO) to buffer forwarded trigger requests by the MCC [24].

Furthermore, each pixel cell has a mechanism to inject analogue charges (see Figure 2.6) for tests, tuning and calibration. This feature was used at the CERN pixel test setup (Toothpix) and at the module test setup at the University of Siegen for further timing studies [25].

Module Control Chip

The Module Control Chip (MCC) is the interface between the Front End chips and the readout chain of the ATLAS detector. Its tasks are controlling the 16 FEs, loading of configuration data into the FEs, module event building from the fragments, that are recorded in the FEs' buffers, and sending the data to the Readout Drivers (RODs).

The MCC receives a bi-phase marked (BPM) encoded signal of the 40 MHz clock and serial commands from the RODs. The Module Port needs to decode this combined signal and distributes the clock signal to the Clock Tree and the commands to the Command Decoder block. The other way round, the Module Port is used to encode data signals coming from the module with the clock signal and to send it back via up to two 40 Mbit/s data lines. The Clock Tree is employed to provide a common synchronous clock signal to the whole Pixel Module, including the MCC. The Command Decoder distinguishes between fast and slow commands. Fast commands are used to commit Level 1 trigger signals (see Section 2.5), slow commands involve instructions like read and write operations to the FE or MCC registers. While slow commands are processed, all data acquisition is stopped by the Command Decoder, since these data would originate from modules in unknown configuration states. The Register Bank of each MCC is equipped with 16 general purpose 16 bit-wide

registers, that are used to set the status of a Pixel Module. It is possible to mask off different FEs or to set the work mode of the MCC, which can be configuration mode, run mode or transparent mode. The latter is used to bypass all the functions of the MCC and to access the FEs directly for configuration and testing purposes.

The Event Builder keeps track of all event fragments from the FEs in a scoreboard. If a trigger signal from Level 1 is distributed through the Trigger Timing and Control (TTC) block to the FEs, the Event Builder formats the fragments to a structured event and transmits it to the RODs. The TTC block is also capable of blocking trigger commands from the RODs, if the Event Builder is still busy with encoding. At last, the Front End Port and the 16 Receiver Channels form the interface between MCC and FEs [5].

The MCC can be programmed such, that it will send back not only the event data associated to one bunch crossing, but the data of up to 16 consecutive bunch crossings. These consecutive 25 ns-wide time-windows will be called Level 1 Accept (LVL1A) windows of the Pixel Modules further on in this thesis.

Timewalk

Particles, that deposit very little energy in the sensor, will lead to a low charge signal, entering the preamplifier. The capacitor is less charged than when there is a high charge deposited. The time, that passes until the full charge is reached, however, is the same for all energy deposits. So, very low charge signals cause the amplifier to pass the threshold later than high charge signals (see Figure 2.9(a)). This flattens the rising edge of the triangular pulse for low charges and may result in the fact, that this very edge is recorded with the following bunch clock cycle rather than with the present one. This behaviour is called timewalk and it is used in the timing studies presented here.
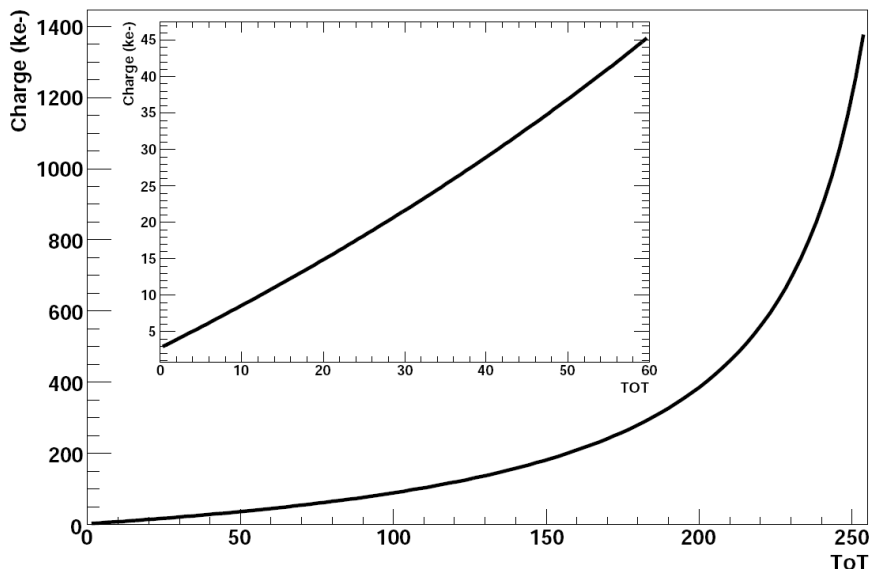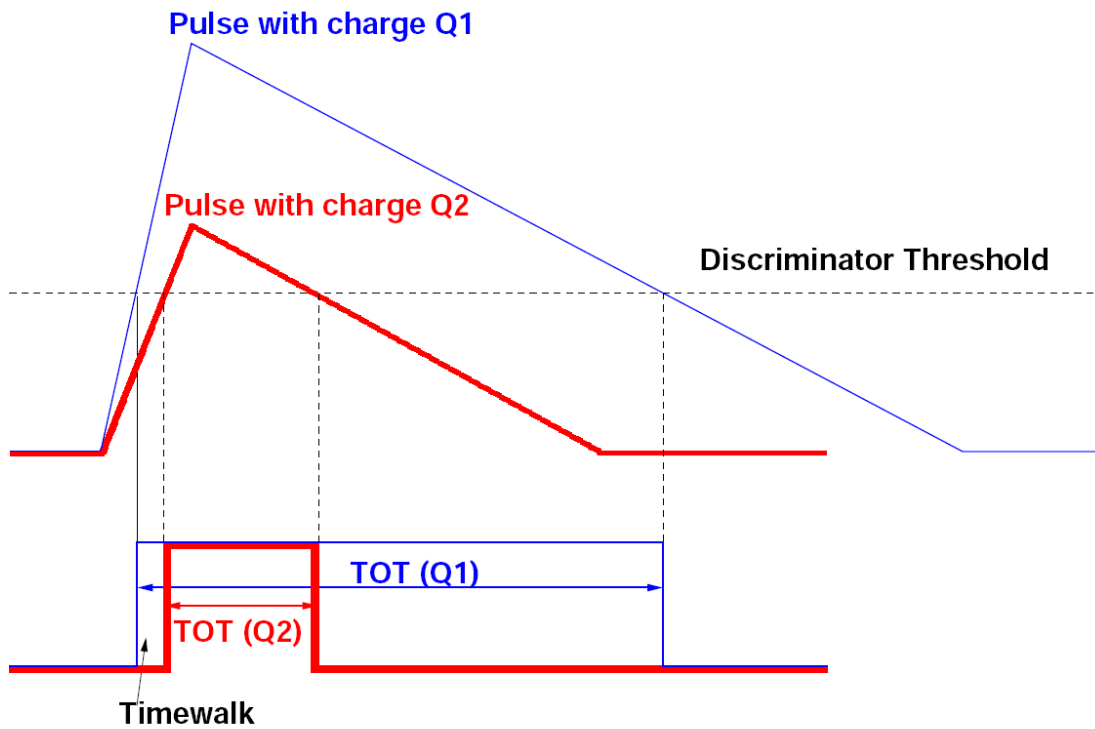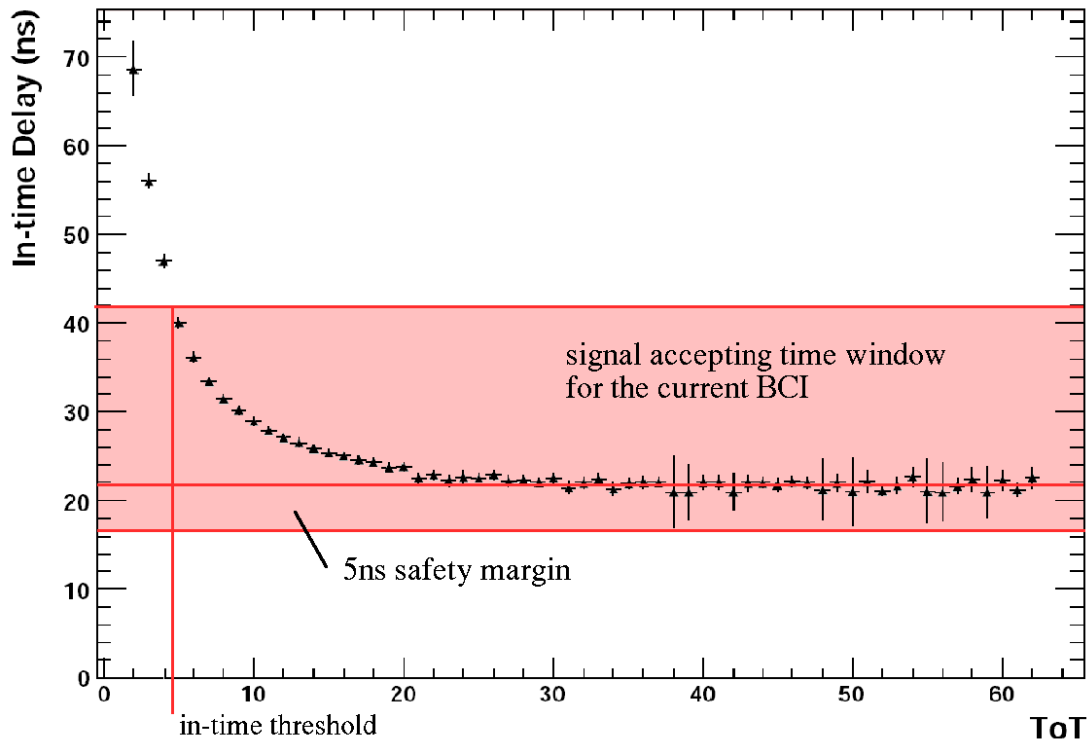

Figure 2.8: Typical relation between the calculated TOT and the charge, liberated by passing particles [19].

(a) Reason for the timewalk. Particles, that deposit little energy in the sensor (bold red curve), cause the TOT signal to pass the discriminator threshold later and may be assigned to the following bunch crossing.

(b) Delay setting for in-time registering versus the TOT of module 510909. This measurement was performed during the combined testbeam with detected testbeam particles in 2004 [19]

Figure 2.9: Timewalk characteristics and results from measurements in 2004 [19].

The effect of the timewalk on the in-time delay is illustrated qualitatively in Figure 2.9(b). The in-time delay is the time, that passes from the instant of a particle passage through the sensor until the discriminator sends a signal to the hitbus (see Figure 2.6). If this period is below 20 ns, the hit arrived in-time, which means, that it is assigned to the correct bunch crossing. High charges and therefore high TOT injections form a plateau in the in-time delay, which serves as the beginning of a trigger window. It is located at an offset of 22 ns in Figure 2.9(b). The in-time delay increases with decreasing TOT values. The minimum TOT, that can be detected within the current BCI, can be read off from the plot by finding the TOT that causes a delay of 22 ns + 20 ns = 42 ns and is the in-time threshold. A TOT value of 4 to 5 BCIs fulfills this requirement. Timing information and minimum TOT should be highly correlated. Section 4.3.2 describes an analysis in which, however, a correlation could not be observed using simple methods. The 20 ns mentioned are used under the assumption, that the high charge signals should rise after 5 ns and not at the very beginning of a BCI to allow for statistical fluctuations in that in-time offset.

Low charges are produced, if a particle passes through the intermediate region between two or perhaps even more adjacent pixels. In this case, the energy is deposited in up to four pixels which is called hit sharing. To reconstruct the original energy, the TOT information of the cells, involved within this cluster, has to be summed. If a MIP causes a signal of about 20 000 electrons, a maximally shared signal is of the order of 5 000 electrons and needs to be detected reliably.

Figure 2.8 represents the typical relation between charge and TOT. The minimum TOT value of 4 to 5 BCIs, that was read off from Figure 2.9(b), corresponding to the in-time delay, can be translated with that relation into 5 000 to 6 000 electrons. These are liberated in the sensor material. MIPs should not result in a lower amount of charges and so, all particles passing the sensor should give a signal that can be detected. Nevertheless, after irradiation of the detector, the collection efficiency will decrease the number of charges liberated by a MIP and very low charge signals will be lost. One option for partial recovery is to decrease the safety margin at the beginning of a readout window.

2.3 Calorimeters

The primary aim of a calorimeter is to provide energy information of an entering particle. All ATLAS calorimeters employ the sampling technology, which means that there are alternating layers of passive absorber material and active detector material. Dependent on the position in the detector, the techniques employed must be chosen such, that they can withstand the different strengths of radiation. If primary particles enter the dense absorber layer, they will interact with the material and create particle showers comparable to the cosmic showers discussed in Section 1.3. The energy measurement will be performed most exactly, if all secondary particles, belonging to the shower, are stopped in the absorbers. These interactions, in the detector layers inbetween the absorbers, lead to signals that are fed to the calorimeter readout electronics.

The calorimeters of the ATLAS system (illustrated in Figure 2.10) cover a region of up to 4.9 in pseudorapidity $|\eta|$. Additional to the energy measurement, they are used to obtain position information with a coarse spatial resolution, to calculate the missing transverse energy E_T^{miss} and to help to identify particles by separating γ from π^0 and $e^{\pm}$ from $\pi^{\pm}$ [18].
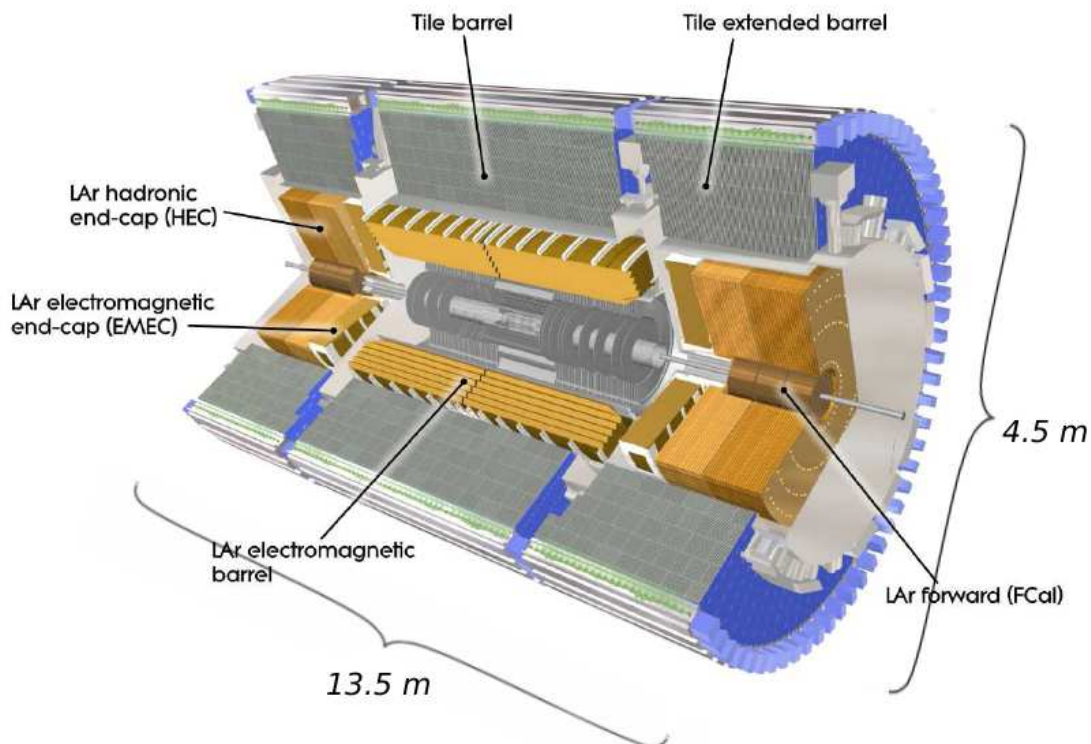
Figure 2.10: The calorimeter system of ATLAS [17].

2.3.1 Electromagnetic Calorimeter

An electromagnetic calorimeter is used to measure the energy loss of those particles, that lose their energy mainly in electromagnetic interaction processes. These particles are electrons and positrons as well as γs.

The ATLAS electromagnetic calorimeter uses lead as passive medium and liquid Argon (LAr) as active medium. It consists of the barrel calorimeter, which itself is made of two half barrels separated at $z = 0$, covering $|\eta| < 1.475$, and the two endcaps consisting of two coaxial wheels each. The inner wheel covers the region $1.375 < |\eta| < 2.5$ and the outer wheel covers the region $2.5 < |\eta| < 3.2$. In order to avoid insensitive detector regions, an accordion structure was employed for the electromagnetic calorimeter.

Expressed in units of the radiation length X_0 of the electromagnetic calorimeter, the barrel detector is more than 24 X_0 and the endcap detector is more than 26 X_0 thick. In order to provide precise position information in the spatial area of the Inner Detector, the first 6 X_0 are made up of 4 mm strips with granularity $\Delta\eta \times \Delta\phi = 0.003 \times 0.1$. The next approximately 18 X_0 are transversally segmented into $\Delta\eta \times \Delta\phi = 0.025 \times 0.025$ and the last 2 to 12 X_0 are segmented into regions of $\Delta\eta \times \Delta\phi = 0.05 \times 0.025$. Thus, the resolution is best in the middle part, where the particle shower is most widely spread.

Before a particle reaches the calorimeter, it loses energy in the Inner Detector, the Central Solenoid and the cryostat which is about 2.3 X_0 thick at $\eta = 0$. A finer segmented thin presampler is installed in front of the calorimeter over $|\eta| < 1.8$. The spread of multiple scattering of incoming particle showers is recorded with this preamplifier. From this infor-

mation, the energy loss, before the calorimeters are reached, can be calculated.

The preamplifier readout electronics is located outside the cryostat and the total number of channels of the electromagnetic calorimeter is about 190 000 [18].

2.3.2 Hadronic Calorimeter

A hadronic calorimeter measures the energy loss of particles that interact mainly in strong processes. It needs to contain all of the parts of a shower, which may occasionally already start in the preceding detector parts, to reduce the punch-through of hadronic particles to the muon spectrometer. The calorimeter is positioned outside the electromagnetic calorimeter since hadronic particles are more deeply penetrating [18].

The ATLAS hadronic calorimeter is divided into three sections: one central barrel ($|\eta| < 1$), two extended barrels ($0.8 < |\eta| < 1.7$) and two endcaps. The barrel parts consist of 3 mm-thick plastic scintillator plates (tiles) between 14 mm iron absorbers. In azimuth, there are 64 modules, which provide a granularity of $\Delta\eta \times \Delta\phi = 0.1 \times 0.1$. Wavelength-shifting fibres in the scintillators direct the signals to photomultipliers. The total thickness of the barrel at $\eta = 0$ in terms of the interaction length λ of the electromagnetic and the hadronic calorimeter together is 9.2 λ, where the electromagnetic calorimeter corresponds to 1.2 λ. For comparison, the interaction length in iron (density ρ_{iron} = 7.87 g/cm^3, λ_{iron} = 132.1 g/cm^2) is λ / ρ_{iron} = 16.8 cm^{-1} for hadrons near room temperature [6]. The hadronic calorimeter spans from r = 2.28 m to 4.23 m and thus, the interaction length yields 24.4 cm^{-1}, from which can be concluded, that its mean density is about two third of the density of iron.

The endcaps are made of two independent wheels each. These consist of alternating layers of parallel plates of 25 mm copper and 8.5 mm-wide liquid Argon gaps for the wheel closest to the interaction point, followed by 50 mm thick copper and 8.5 mm liquid Argon in the outer wheel. In the gaps between the plates, three high voltage electrodes are installed, forming four smaller gaps, to employ the concept of an electrostatic transformer [26]. 32 identical modules constitute one endcap in azimuth and correspond to a granularity of $\Delta\eta \times \Delta\phi = 0.1 \times 0.1$ to 0.2×0.2. The hadronic calorimeter altogether provides about 10 000 readout channels to the data acquisition system.

2.3.3 Forward Calorimter

The coverage of $|\eta| < 3.2$ of the hadronic endcap calorimeters overlaps with the coverage of the forward calorimeters, which have $|\eta| > 3.1$. Each of the latter consists of an electromagnetic forward calorimeter and two sections of hadronic calorimeters, which are all included in the same cryostats as the hadronic endcap calorimeters. Copper and liquid Argon are used in the first (electromagnetic) section of the forward calorimeter and tungsten and liquid Argon are used in the second and third (hadronic) parts. Matrices made of longitudinal channels, filled with concentric tubes parallel to the beam pipe, provide 3 584 data channels for both sides of the forward calorimeter. The small gaps ($\sigma(100\mu\text{m})$) between tubes and rods permit short drift times and therefore high readout rates. A passive copper plate behind all forward calorimeters is installed to ensure a total thickness of about 10 λ in all regions $|\eta| < 4.9$. This shields the muon spectrometer from punch-through particles.

2.4 Muon Detector System

The ATLAS muon detector system is built to serve different purposes: bunch crossing identification, the supply of Level 1 trigger decisions and the supply of track coordinates in both ϕ- and η-direction. Derived from the track information, a precise calculation of the transverse momentum p_T of passing muons can be performed. Because these needs cannot be satisfied with one type of detector, four technologies are used to perform both the high-precision tracking and the triggering.

The muon spectrometer system determines the dimensions of the experiment (see Figure 2.1). The barrel part of the muon system is equipped with three cylindrical layers around the beam pipe at radii of 5, 7.5 and 10 m and with four discs at each endcap at a distance of 7, 10, 14 and 21 to 23 m from the interaction point. The region of $|\eta| < 1$ is covered by the barrel, $1 < |\eta| < 2.7$ by the endcaps. The innermost layer of the barrel part at regions of high rates (the very forward direction $2.0 < |\eta| < 2.7$, [27]) consists of Cathode Strip Chambers (CSC), that provide a higher precision in track measurement than the Monitored Drift Tubes (MDT), which are used in all the other parts of the muon system. Closer to the interaction point, the particle flux is higher, which requires a faster technology to be employed. The maximum drift time for the CSCs is about 30 ns, whereas it is about 700 ns for MDTs. The spatial precision is of the order of tens of micrometers for both cases. All chambers provide information in the η-direction. Additionally, the innermost barrel layer provides information on ϕ, as a second set of chambers is used there, orthogonal to the first set. The trigger part of the muon system is made of Resistive Plate Chambers (RPC) in the barrel region. There are two RPCs within the field of the toroid magnets and one directly behind it. Each RPC consists of two independent detector layers with stereo angle to obtain two coordinates per hit. For the endcaps, three layers of Thin Gap Chambers (TGC) serve as trigger stations, all outside the magnets. Furthermore, the anode signal of the CSC is used to contribute to the trigger forming process. Trigger chambers provide spatial information on η and ϕ.

MDT, CSC and TGC are sets of single-wire proportional drift tubes [18]. The RPC, in contrast, is a gaseous parallel electrode-plate detector without wires [27].

2.5 Trigger System

At full performance, the interaction rate in the ATLAS detector will be of the order of 10^9 Hz. It is technically feasible to record data with a rate of maximally 100 Hz to permanent storage devices.

The trigger system, therefore, needs to select events of interest with a high efficiency, while at the same time providing a rejection factor of about 10^7 for events, that are already well-understood and do not contribute to answering the open questions. The ATLAS trigger system consists of three consecutive levels of online selection systems, each refining the decisions made at the previous stage. At Level 1 (LVL1), fast decisions are made using coincidences and vetos from hardware devices. Level 1 may trigger on muons in the muon system, electrons and photons as well as hadronic jets in the calorimeter systems, on missing transverse energy E_T^{miss} and events with a certain amount of transverse energy E_T or momentum p_T.

Level 2 (LVL2) and the Event Filter (EF) form the ATLAS High Level Trigger (HLT) and

are implemented in software running on computer farms. A schematic view of the trigger system can be seen in Figure 2.11 [28].
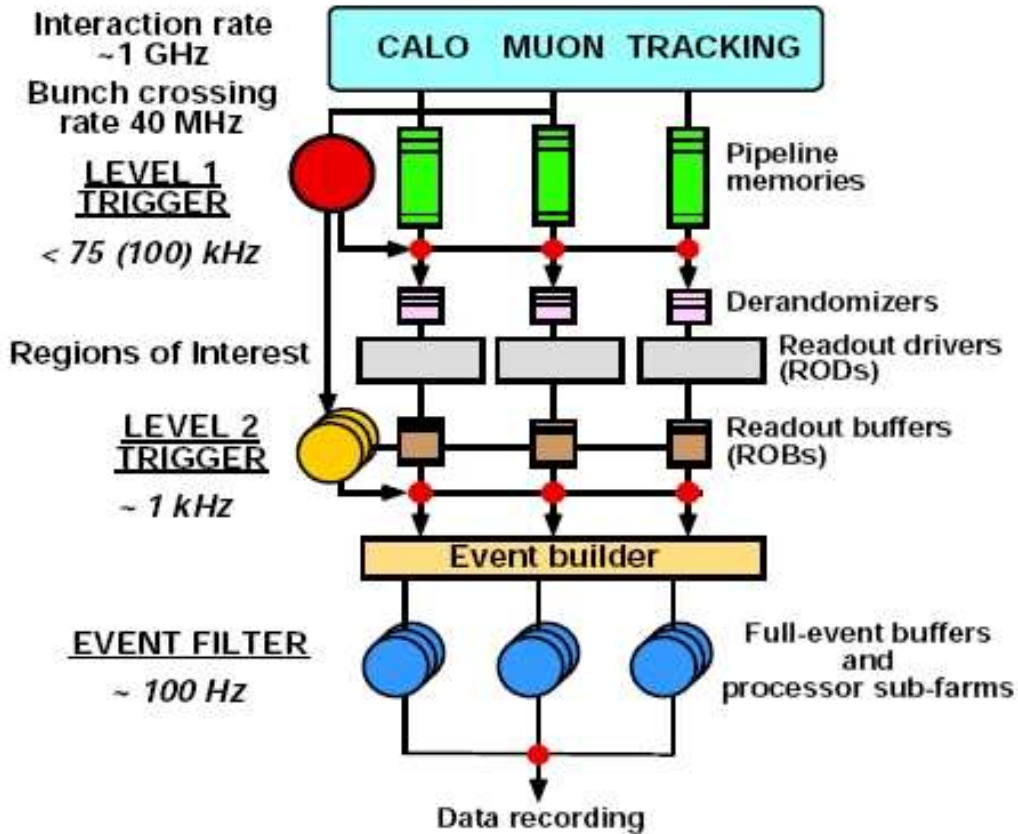

Figure 2.11: Block diagram of the trigger/data acquisition system [28].

2.5.1 Level 1 Trigger

Because the maximum input rate, that can be handled by the ATLAS Front End electronics, is about 75 kHz (upgradable to 100 kHz), the first selections on Level 1 must be such, that the total Level 1 output rate is of that order. To take into account uncertainties in the calculation, the trigger menus are set up in a way, that the expected rate of events passing the Level 1 trigger is about half of the maximum rate. Rate reduction in general is possible by increasing thresholds and relying more heavily on larger numbers of coincidences and vetos (multiobject triggers).

The time to form and distribute a trigger decision (latency time) needs to be as short as possible, since the information for all detector channels has to be kept in pipelined memory buffers, that are limited in depth. The target latency time was 2.5 μs with 0.5 μs as a safety margin. The Level 1 system finally needs to identify the bunch crossing ID and to add it to the recorded event data [28].

2.5.2 High Level Trigger

If an event is selected by Level 1, the (still) fragmented event data is read into Readout Buffers (ROBs) by the Readout Drivers (RODs). It is held in the ROBs until a decision is made at Level 2, which is either the decision to reject the event (and consequently the deletion of the event data) or the decision to pass Level 2 and to transfer the data to the Event Filter and, if all conditions are fulfilled, to storage devices.

In order to speed up the Level 2 decision making, the Level 2 algorithms use a Region of Interest (RoI) based evaluation of data. The RoIs are formed by the η- and ϕ-coordinates as well as by the p_T and E_T values of elements, such as a high p_T muon, e/γ or jets, the E_T^{miss} vector or the E_T scalar, that are used in the trigger. Only the information that is required by Level 2 is transferred from the ROBs to the computing farms.

It may happen, that the Level 2 trigger requires RoI objects (secondary RoIs) in addition to those that formed the Level 1 decision (primary RoIs). Therefore, the Level 1 system is capable of providing all the needed RoI information to Level 2.

The output rate of Level 2 needs to be less than 1 kHz and the Level 2 latency should be below 10 ms on average per event, whereas on Event Filter level, the algorithms may take up to 1 s to make a decision. The Event Filter algorithms are based on code from offline analysis. Unlike the Level 2 trigger, which works on event fragments, the Event Filter has access to the fully reconstructed event (reconstructed by the Event Builder in Figure 2.11) [28].

Chapter 3

Timing Studies – Endcap Cosmics Run

In this chapter, the analyses performed on the data of cosmics run 1129 in 2006 are discussed. In the beginning, the system test setup is described. For the determination of the module timing, simulated and measured data are compared. The different production steps of the simulation and the software packages used for the analyses are outlined. A method for the estimation of the uncertainties comes along with the development of an algorithm for the determination of the Pixel Module timing. A comparison with the results of existing studies [15] is given at the end.

3.1 Real Data

3.1.1 System Test Setup

In December 2006, a complete endcap of the Pixel Detector, composed of three discs and equipped with 144 Pixel Modules, was set up with the full readout chain in one of CERN's clean rooms. The system was driven under pit operation conditions in dry air and was cooled down to the operational temperature of -17°C by the evaporative cooling system [16]. At that time, this endcap was the largest part of the Pixel Detector running as a full system (8.3 %). As well as performing tests and commissioning tasks on the readout chain, data from cosmic particles were recorded.

The endcap was positioned with its discs orientated horizontally in order to maximise the flux of cosmic muons through the detector and to enlarge the number of muon tracks with at least three hits in the detector. As shown in Figure 3.1, a trigger system made of four scintillators was constructed around the endcap. The minimum requirement for triggering was a coincidence signal from the top and bottom scintillators 3 and 4 in Figure 3.1. A $\Delta x = 12$ cm thick iron layer ($\rho_{iron} = 7.87$ g / cm^3) excluded particles with a kinetic energy of less than 145 MeV from being detected by the bottom scintillator. This value follows from Equation 1.5 by calculating the mean energy loss in the iron layer (taking into account the approximation for materials with $Z/A \approx 0.5$):

$$\Delta E = -\frac{dE_\mu}{dx} \cdot \Delta x = 2 \; \frac{\text{MeV}}{\text{g/cm}^2} \cdot \rho_{iron} \cdot \Delta x = 145 \text{ MeV}.$$

Muons with such low energies mainly result from multiple scattering processes. In order to exclude muons with higher energies, the iron layer would have required to be thicker. This was not possible, because the setup could not carry a heavier load. As can be seen in the schematics in Figure 3.1, there will be some muons that pass both scintillators 3 and 4 but not the endcap. This will result in the recording of underlying noise. Two more scintillators, 1 and 2, were set up below the system, away from the endcap axis, to allow
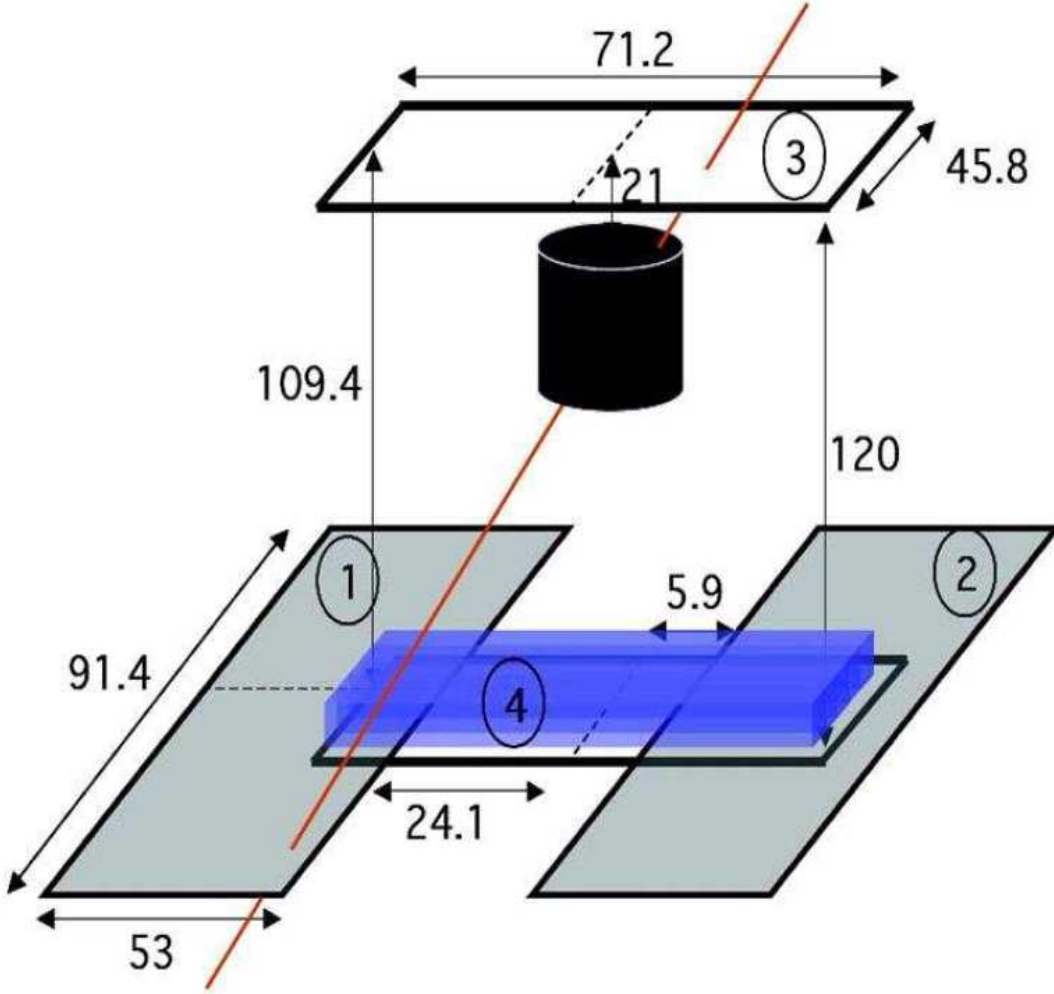
Figure 3.1: Schematics of the pixel endcap A cosmics setup [16]. All dimensions
are given in cm.

the recording of muons coming in at oblique angles. The trigger system then required a
hit in the top scintillator and an associated signal in one of the three bottom ones [16].

The position of a Pixel Module in the ATLAS detector is defined by the coordinates η and
ϕ, that describe the centre of a module. The first module is positioned at $3.75°$ in ϕ, every
other module is rotated by $7.5°$ in the $r\phi$-plane with respect to the previous module. For
the endcap cosmics run, new coordinates were introduced. A module is classified by its
layer (Disc 0, 1 or 2) and a φ index ranging from 0 to 47 where

$$\phi[\text{rad}] = (\varphi + 0.5) \cdot 7.5 \cdot \pi/180°.$$

Modules with even φ are mounted on the bottom side of the disc, which would be closer
to the interaction point in collision runs, and modules with odd φ on the other side. In
this configuration, there are overlap regions and dead detector areas are avoided.

3.1.2 Cosmics Data Reconstruction

Information about data-taking runs for the pixel system are given in [29], including those runs that form the basis of the analysis discussed in this thesis. Primarily, run 1129, which provides data from about 15 hours of recording, is used. The data files can be found at [30]. The trigger signal, produced by the trigger system, described in Section 3.1.1, was repeated 15 times. Thus, 16 LVL1A windows (see Section 2.2.3) were read out from the Pixel Modules for each trigger signal.

During data taking, 29 of the 144 Pixel Modules of the endcap were switched off from the beginning due to technical problems such as a disconnected cooling loop, a malfunctioning opto board, a missing high voltage or temperature monitoring. A noise map was created with run 1131: An external trigger, driven from 10 Hz up to 15 kHz and back to 10 kHz, was employed and resulted in 14 147 494 events. The occupancy is defined as the number of hits in a pixel, divided by the number of pixels per module (46 080) and by the number of events in the run. Ignoring those modules, that were disabled during run 1131, the average occupancy was calculated to $2.5 \cdot 10^{-7}$. Pixels with an occupancy greater than 10^{-4} were labeled as being potentially noisy. This reduces the average occupancy of the endcap to $4.8 \cdot 10^{-9}$. Excluding two modules (module IDs 510853 and 512876) with unusually high noise levels, the occupancy decreases to the order of 10^{-10}. A comparison of the recorded noise pattern with pixels, that had been marked as notable during production tests (for example if the threshold was not tunable), showed, that 93 % of the noisy pixels had already been marked. The noise is dominated by fixed pattern noise and can therefore easily be excluded from the data. Random noise is at very low level and can be neglected for most applications. The pixel maps, employed in the offline analysis on the data of run 1129, are listed below [16].

- `PixelEndcapACosmics-00`: This map was created to disable modules, that had technical problems during the endcap runs.

- `NoiseMap-run1131-00`: This map excluded pixels, that were noisy during noise run 1131.

- `PixMap-Assembly-00`: This map marks pixels, that were known as non-functional or noisy from assembly tests.

In Figure 3.2, the LVL1A distribution of module 511665 is given. This can be taken as an example, showing, that after performing a track based reconstruction (only those hits are accepted that are assigned to a cluster and then to a track) and by using the maps mentioned above, all noise could be excluded from the sample. If there was noise present, it would appear in each of the 16 LVL1A bins. Actually, only the bins, in which the signal was expected to lie, are populated. The trigger signal was delayed until most hits were seen in LVL1A bin number 5. Therefore, the optimal setting for the Pixel Module timing is to measure the high energy hits at

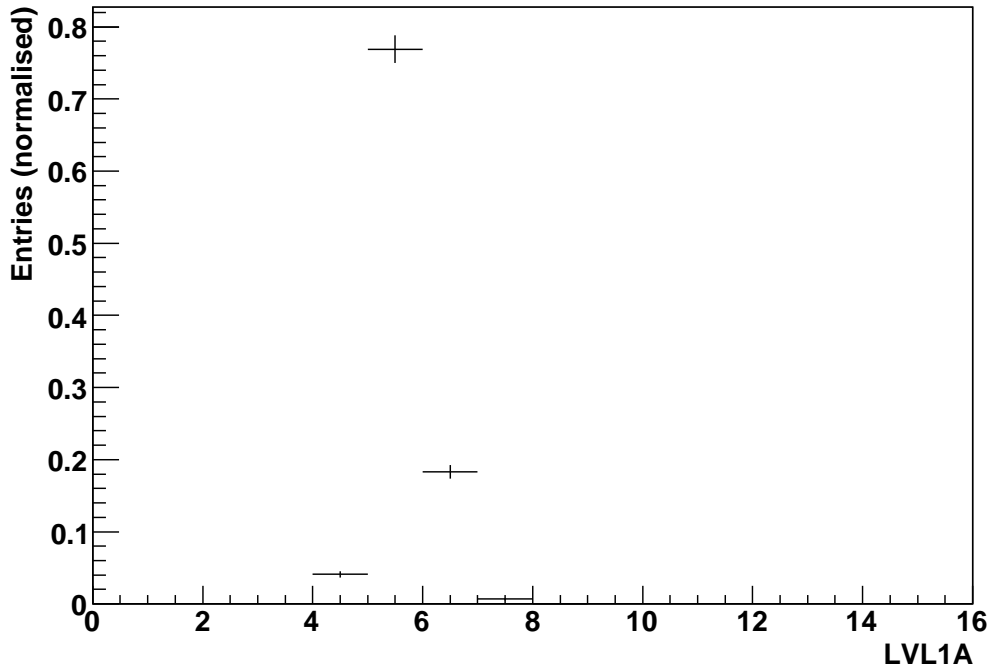$$t_{\text{optimal}} = 5 \times 25 \text{ ns} + 5 \text{ ns} = 130 \text{ ns}. \tag{3.1}$$

.

Figure 3.2: LVL1A distribution of module 511665 with hits from tracks only from cosmics run 1129.

3.2 Simulated Data

Before physics data are taken, the ATLAS computing framework Athena [31] is used to generate Monte Carlo (MC) data and precisely simulate the ATLAS detector. The particles generated are propagated through the detector, interacting with the detector material. Simulated hits in the active parts of the detector are then digitised, the underlying events are reconstructed and data in the same format as real data is produced. With this setup, a common analysis code can be run on simulation and real measurements. From the reconstruction onward (see Figure 3.3), the analysis chain can be the same. Also for later collision runs, the evaluation of real data will be based on a comparison of the real data with the outputs of the simulation.

3.2.1 Generation of Cosmics Data and Detector Simulation

In the MC generation, particle four-momenta from specific physics processes or events are produced (HepMC in Figure 3.3). The particles are passed through a GEANT4 simulation of the detector [32]. GEANT4 calculates the energy loss of each particle on its way through the detector material (G4 Hits in Figure 3.3). In this analysis, the whole chain, consisting of event generation, detector simulation, hit digitisation and reconstruction, was based on the software packages for Athena release 13.0.20. The basic procedure of simulation and reconstruction of cosmics data for the endcap setup is described at [33, 34].
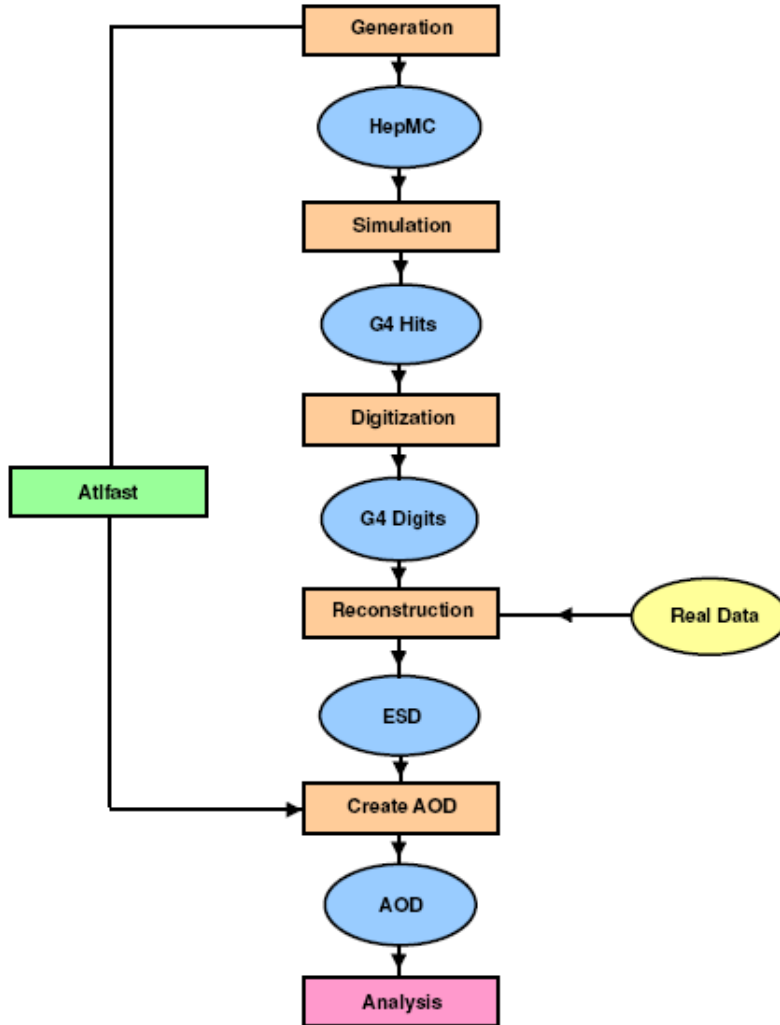
Figure 3.3: Schematics of the data flow through the analysis [31].

Over an area of 458 mm $\times$ 712 mm, at a distance of 295 mm from the top disc of the endcap, a million muons were generated with the `CosmicGenerator` package of Athena. The energy range of these muons varied from 500 MeV to 200 GeV: the lowest energy allowed was larger in simulation than in the real measurement. For the endcap cosmics simulation, a special detector description was used (see job option file `PixelEndCap_DigitisationTst.py` [33]): The whole Inner Detector (consisting of the beam pipe, the Pixel Detector, the SCT, the TRT and the Beam Condition Monitor BCM) was disabled, i.e. it did not exist in the GEANT4 detector simulation. Also, the calorimeters and the muon system were disabled. Then, only the Pixel Detector was enabled again in the software. In the Pixel Detector, barrel layers and endcap C, pixel support tubes, frame and services had to be removed [16]. In this way, only endcap A remained of the full Pixel Detector geometry as implemented in the `PixelGeoModel` package of Athena [35]. The scintillators were added to the detector

layout (`G4AtlasApps` package [36]). When a muon passed a virtual scintillator, the energy loss along that track was computed and a hit was flagged, if the energy loss was above zero. That means, that no hit can be lost due to the constraints of the scintillators' resolutions. The scintillator logic is implemented in the `InDetCosmicSimAlgs` package [37]. Only those hits that match a chosen trigger strategy are passed to the digitisation. Finally, the magnetic field was switched off.

All these changes were activated by using the `IDET-cosmic-PixelEC` detector description in simulation and `ATLAS-InDetEndcapA-00` in digitisation.

3.2.2 Digitisation

The digitisation describes the interaction of simulated particles with the active detector parts and produces values such as times and voltages, as they will be seen in the raw data from real data taking (G4 Digits in Figure 3.3).

The standard digitisation algorithm from Athena release 13.0.20 was used without major modifications. However, the job options were not used in standard mode [33]. A Front End specific timewalk behaviour (see Section 2.2.3) of every Pixel Module is stored in the Conditions Database. These data were produced during production and assembly tests and can now be used for digitisation (job option `UseCalibCondDB = True`). The algorithm `PixelMonitoring` was switched off for the digitisation run, since it was still under development in 2007.

Efficient tracking algorithms should reduce the amount of thermal and random noise recorded to almost zero. The low statistics on the measurement of cosmic particles and the high tracking efficiency allowed for switching off the simulation of thermal and random noise (job options `ThermalNoise` and `RndNoiseProb`) in this specific case.

Cosmic particles arrive randomly in the detector. The pixel modules are driven with a 40 MHz clock. As there is no correlation between the scintillator trigger and the clock, an uncertainty of 25 ns has to be simulated. This is achieved by adding a jitter of $\pm\frac{25}{2}$ ns (job option `TimeJitter`) to the arrival time of the particles in the Pixel Modules.

With regard to the analysis, the time per bunch crossing (job option `TimePerBCO`) was set from the nominal 25 ns to 0.25 ns. Then, instead of reading out 16 LVL1A windows, 255 windows were read out (`TimeBCN`) to monitor a time window of about 64 ns. Effectively, the clock frequency was increased by a factor of 100.

Different times of flight for the generated muons to the detector volume (G4Time), timewalk and the TimeJitter led to the distribution of the hit recognition time as shown in Figure 3.4 and described in Equation 3.2. The offset in the timing (job option `TimeZero`) was set to 15 ns. This is the number that is to be reconstructed in order to obtain the Pixel Module timing. It is notable, that Figure 3.4 is the sum of all finely binned LVL1A plots of the Pixel Modules:

$$\text{timing} = t_{\text{hit recognition}} = \text{TimeZero} + \text{TimeJitter} + \text{timewalk} + \text{G4Time}. \qquad (3.2)$$

Below, the changes to the job options of the digitisation are listed:

- `PixelDigitization.TimeJitter = 25 ns (default:  0)`,

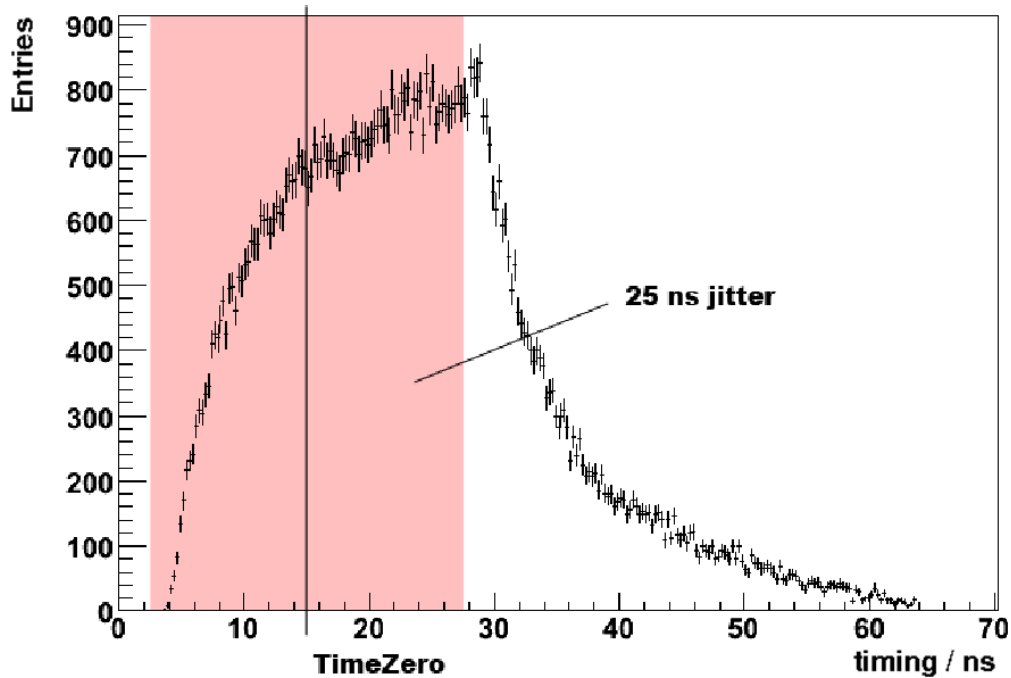- `PixelDigitization.TimeZero = 15 ns (default:  0)`,

Figure 3.4: Distribution of the simulated, finely binned hit recognition time. Summed over all modules. TimeZero set to 15 ns.

- `PixelDigitization.TimePerBCO = 0.25 ns` (default: 25 ns),

- `PixelDigitization.TimeBCN = 255` (default: 16),

- `PixelDigitization.ThermalNoise = 0` (default: 220 e^-),

- `PixelDigitization.RndNoiseProb = 0` (default: $5 \cdot 10^{-8}$),

- `PixelDigitization.RndDisableProb = 0` (default in Athena release 13.0.20),

- `PixelMonitoring` switched off.

3.2.3 Reconstruction

The Raw Data Object (RDO) from simulation, or equivalently the bytestream from real measurements, are processed by the reconstruction algorithms. These algorithms look for hit clusters, particle tracks, etc. in the data and store them in Event Summary Data (ESD), with those hits and clusters connected, that are associated to a single event. The ESD can then be reduced to the Analysis Object Data (AOD) (see Figure 3.3) and ROOT ntuples [38]. Because not every hit is stored with the full information, an AOD file is much smaller than an RDO or an ESD file. The final analysis proceeds on AOD files.

For this part of the analysis, the reconstruction package for release 13.0.25 was used. The only changes in the job options, notwithstanding those which are already noted in [34],

were to switch off `PixelMonitoring` and `InDetCosmicMonitoring` and to call for at least three track points in a track (job option `InDetAmbiTrackSelectionTool.minHits=3`). The default value is four, which is a very loose constraint when using the whole Inner Detector (see Section 2.2) but a rather strong one when using just one pixel endcap.

The reconstruction algorithms produced combined ntuples (CBNT), which were accessed with stand-alone ROOT (version 5.12/00e [38]) macros for further analysis. The development of these macros constitutes the main part of this thesis.

Chapter 4

Timing Studies – Analysis of Cosmics Data

In this chapter, the data form cosmics run 1129 is analysed. A representative example of a module, module 511665, located on Disc 2 at $\varphi = 37$, will be used to explain the method of calculating the timing. The results will be discussed in the following sections together with a study on determining the errors on the results. Finally, a comparison with existing results [15] is presented.

4.1 TOT Distribution

Scripts based on `track_navigation.C` [34] were written to extract the TOT and the LVL1A distribution for each module from the data. The pixel tuning was such, that minimum ionising particles should result in a TOT of 30 and the trigger was delayed such, that most cosmic hits were seen in LVL1A bin number 5. As particles can pass through the sensor in the border area of a pixel, hit-sharing is likely to occur. In this case, the charge, that is liberated by one particle, will be partitioned between up to four neighbouring pixels. Several entries with low TOT will be seen in the TOT spectrum instead of one entry corresponding to all the deposited energy. Figure 4.1 shows the TOT distributions of module 511665 on the left-hand side as recorded and the corrected version on the right-hand side. To obtain the latter, TOT entries from the original recording, that were assigned to one cluster, were summed. Because the deposited charge as a function of the particle's energy is approximately linear for low energies (see Figure 2.9(b)), the shape of the TOT distribution mirrors the Landau distribution of the energy spectrum of cosmic muons, losing energy in matter (see Section 1.3). The peak at low TOT values from the left plot almost completely vanishes when these entries are summed to clusters and a distinct peak can be seen, consistent with 30 BCI. The number of entries is reduced from 2 116 to 1 058 due to the summation for module 511665.

Figure 4.2 shows the TOT distributions for module 511665 produced by the simulation. Here, a peak near 30 BCI can also be observed after the summation of hits from clusters. The number of entries decreases from 571 hits to 313 clusters. The Landau function fits to the two TOT distributions of real data and simulation. The fits give different most probable values, namely $\mathrm{mpv_{data}} = 28.18 \pm 0.23$ BCI for the real data and $\mathrm{mpv_{sim}} = 26.4 \pm 0.4$ BCI for the simulation. The conversion between liberated charge Q in the pixel sensor and the TOT value is performed with

$$\mathrm{TOT} = A \cdot \frac{Q + E}{Q + C} \pm (p1 + p2 \cdot \mathrm{TOT}). \tag{4.1}$$

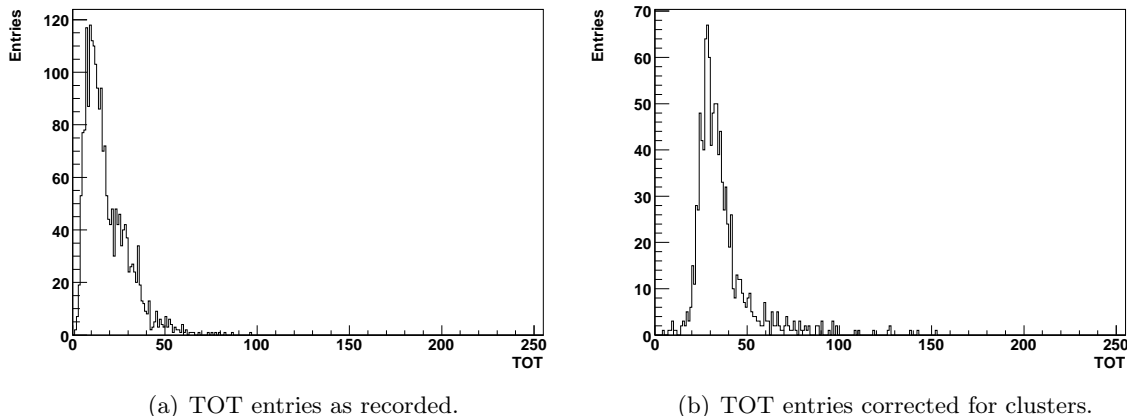(a) TOT entries as recorded.   (b) TOT entries corrected for clusters.

Figure 4.1: TOT distributions of module 511665.

The parameters A, C and E were taken from the calibration database [39]. The calibration data was taken during assembly test and it is stored in the database for each of the 16 Front End chips of the Pixel Modules. The dispersion on the TOT value can be estimated by using the typical values in the module calibration. These are $p1 = 0.4$ BCI and the contribution of $p2$ being similar to the contribution of $p1$ at TOT=20 BCI, which results in an estimate of $\sigma_{(\text{TOT}=20)} = 0.8$ BCI increasing with the TOT values. This uncertainty needs to be added quadratically to the most probable values given by the Landau fit and brings simulation and real data into agreement.

(a) Simulated TOT entries not summed to clusters.   (b) Simulated TOT entries corrected for clusters.
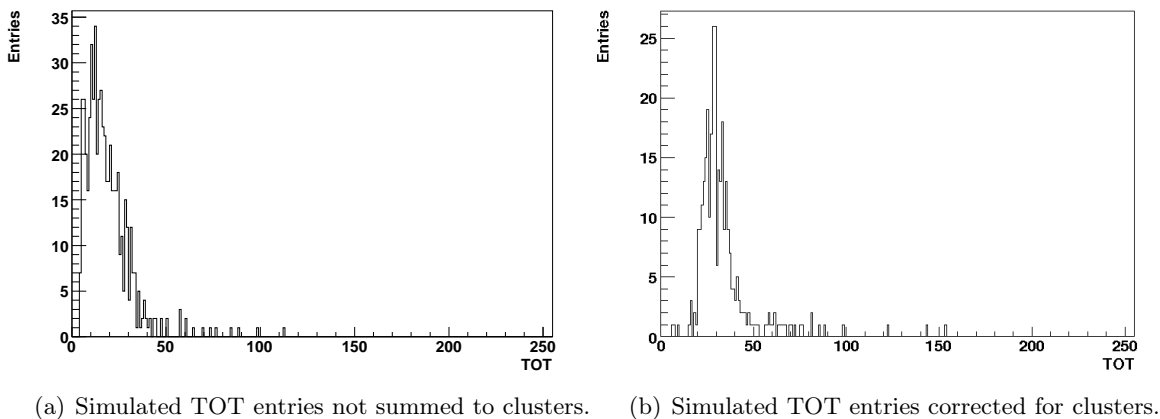
Figure 4.2: Simulated TOT distributions for module 511665.

Looking at the shape of the distributions in Figure 4.1, it is possible to confirm that the recorded data contain cosmic muons. This is the case, if the distribution shows a Landau shape with its peak consistent with 30 BCI. A comparison of Figures 4.1 and 4.2 provides a check on whether the simulation ran properly and whether it described the physics and the detector well.

Figure 4.3 shows another check on the operation of the reconstruction process on the data. The total number of clusters, the distribution of the number of clusters per track and the
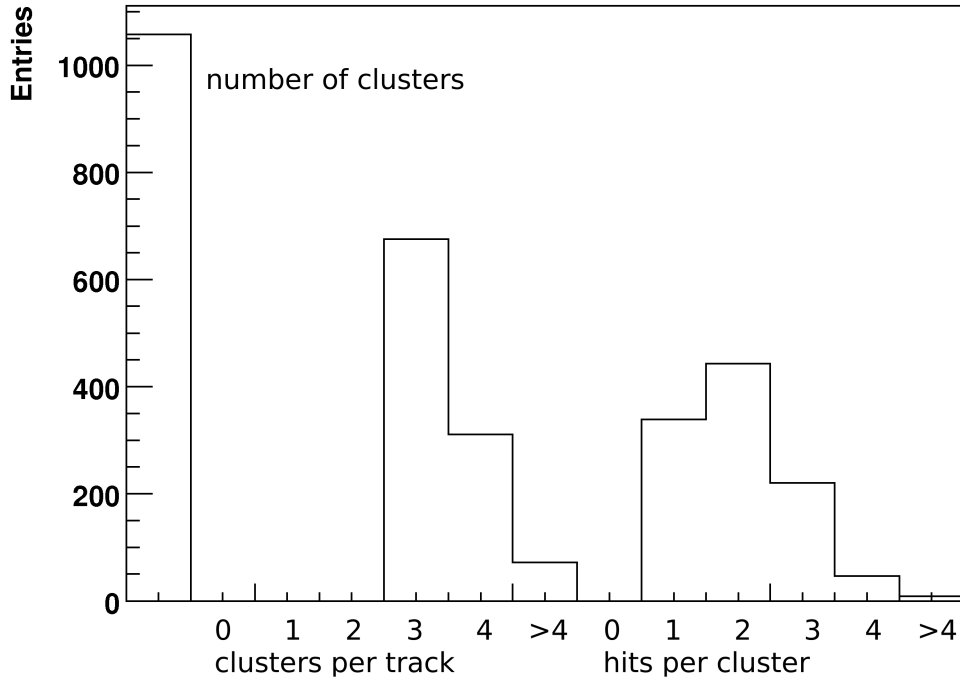
Figure 4.3: Information from the data about tracks and clusters for module 511665.

distribution of the number of hits per cluster are presented. All three parts of the histogram are normalised to the total number of clusters. For example, a four-cluster track results in four entries in bin number four in the plot of clusters per track. The number of clusters per track is at least three. Tracks with less than three clusters were excluded from the track finding. Particles may cross more than three Pixel Detector layers only in the overlap regions of the Pixel Modules that are mounted on the front- and back-side of a disc. As expected, the distribution shows most entries at three clusters per track. A cluster itself consists of at least one pixel hit. Since a pixel cell has a rectangular shape with an aspect ratio 8:1, the probability to have two hits per clusters is expected to be significantly larger than the probability of having more. Clusters with more than four hits originate from particles at oblique angles of incidence. A comparison with the simulation (see Figure 4.4) shows, that the data have fewer two-hit clusters and more clusters with three or more hits than expected. Apart from that, the simulation is in agreement with the measurements.

4.2 Minuit-based Calculation of the Pixel Module Timing

After receiving a trigger signal in run 1129, the MCC (see Section 2.2.3) was programmed to send back the recordings of 16 consecutive bunch clock cycles. In this way it is certain, that, in case a hit was assigned to a wrong bunch crossing, it will be seen in the data nevertheless. These 16 bunch crossing intervals are henceforth called LVL1A windows (see also Section 2.2.3).
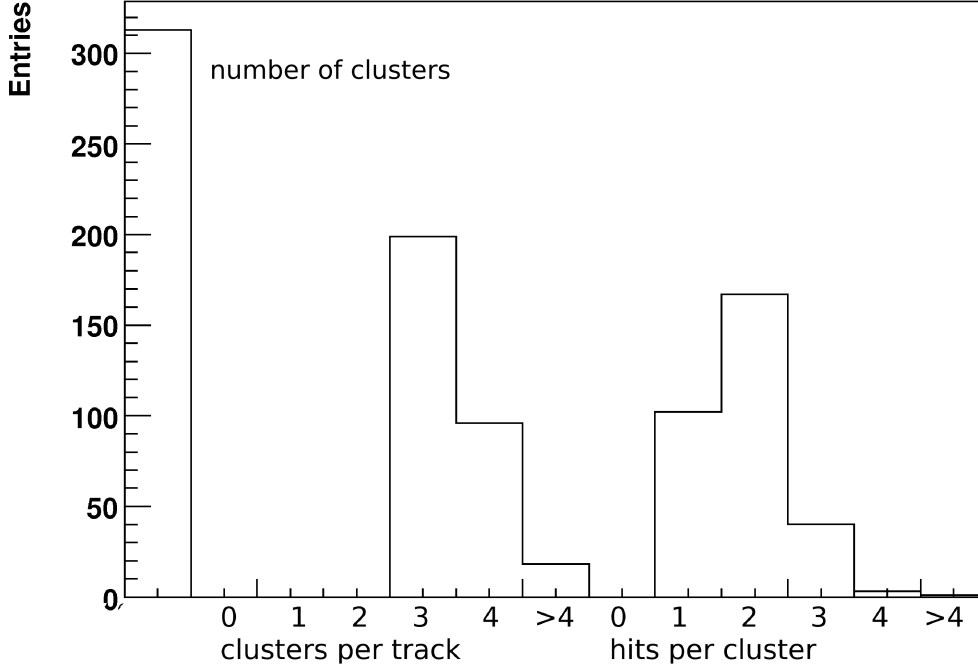
Figure 4.4: Information from simulation about tracks and clusters for module 511665.

The readout of more than one LVL1A window is only possible because the cosmic hit rate is very low compared to later collision runs. In about 15 hours of data taking in run 1129 [30], 77 850 clusters were recorded. From the data, 24 989 tracks could be reconstructed out of these clusters, which leads to an event rate of 0.46 Hz or about 28 hits per minute. This rate has to be compared with the 400 ns (equivalent to 2.5 MHz) readout duration for 16 LVL1A windows. When recording cosmic data, it is possible to read out all the LVL1A windows from the Pixel Modules. The expected number of muons passing the active detector parts can be estimated by calculating

$$N_{\mu \text{ passing the detector}} = \phi_{\text{ground level}} \cdot A_{\text{active pixel area}} \cdot t_{\text{data taking}} \approx 410\,000,$$

where $\phi_{\text{ground level}} = 1 \text{ cm}^{-2}\text{min}^{-1}$ is the approximate muon flux at ground level and the active detector area is $A_{\text{active pixel area}} = \pi \cdot (R^2_{\text{max}} - R^2_{\text{min}}) = 455 \text{ cm}^2$ (with $R_{\text{max}} = 14.96$ cm and $R_{\text{min}} = 8.88$ cm describing the minimal and maximal radius, that is covered by active sensor material on the endcap discs [17]). Thus, the track reconstruction efficiency is about 24 989 / 410 000 $\approx$ 6 % for the setup presented, which is in agreement with the existing calculations [16].

In the simulated data, there are 14644 tracks reconstructed from 1000000 generated muons. There are eight events with two tracks and none with more tracks per event. This is a further difference between simulation and real data, as in the latter, 97 two-track events were reconstructed and even 13 events with more than two tracks.

The module timing can be deduced from the shape of the LVL1A distribution (compare also with [15]). In Section 3.2.2, it was stated, that for simulation the clock frequency was raised by a factor of 100. Because of this, the binning of the LVL1A distribution for each module was decreased from 25 ns to 0.25 ns without which the following analysis would not have been possible. Figure 4.5 shows only those entries from Figure 3.4 that correspond to module 511665. Henceforth, this will be called the finely binned LVL1A distribution for module 511665.
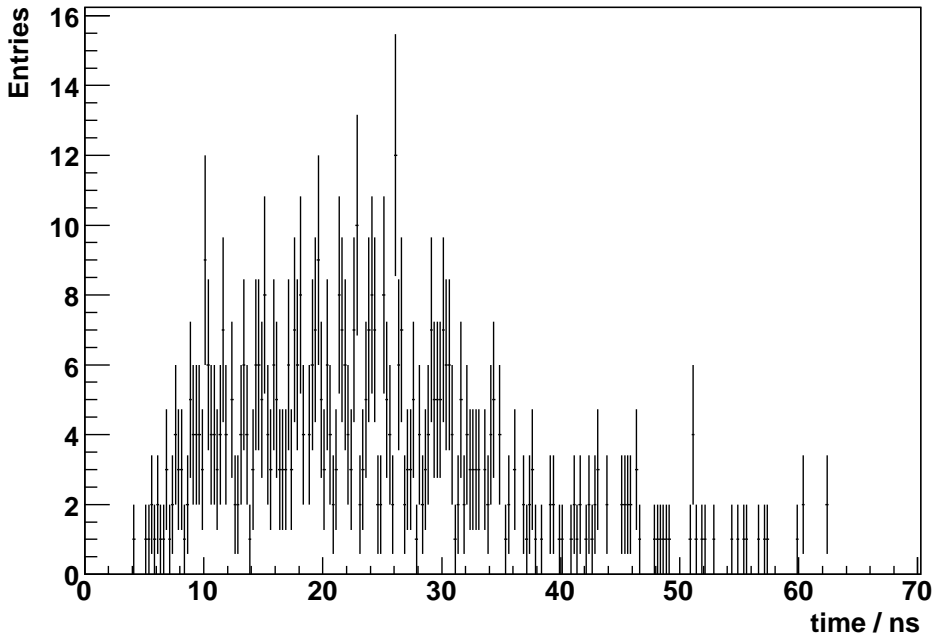
Figure 4.5: Finely binned LVL1A distribution for module 511665. After applying the special settings mentioned in Section 3.2.2 to the digitisation job, this histogram is written to the output file as a BCID distribution for the named module.

In Figure 4.6, the distribution from Figure 4.5 is rebinned into 25 ns-wide bins and it therefore reflects the detector output for module 511665 with TimeZero set to 15 ns. The finely binned LVL1A distribution from the simulation (Figure 4.5) is used to generate a set of fit functions for the LVL1A distribution from the real data (Figure 3.2). The fit functions are obtained by applying a certain time shift to the finely binned LVL1A distributions and rebinning the result into 25 ns-wide bins. Figure 4.7 illustrates four possible fit functions with different TimeZeros. The shape of the distribution depends strongly on the TimeZero value.
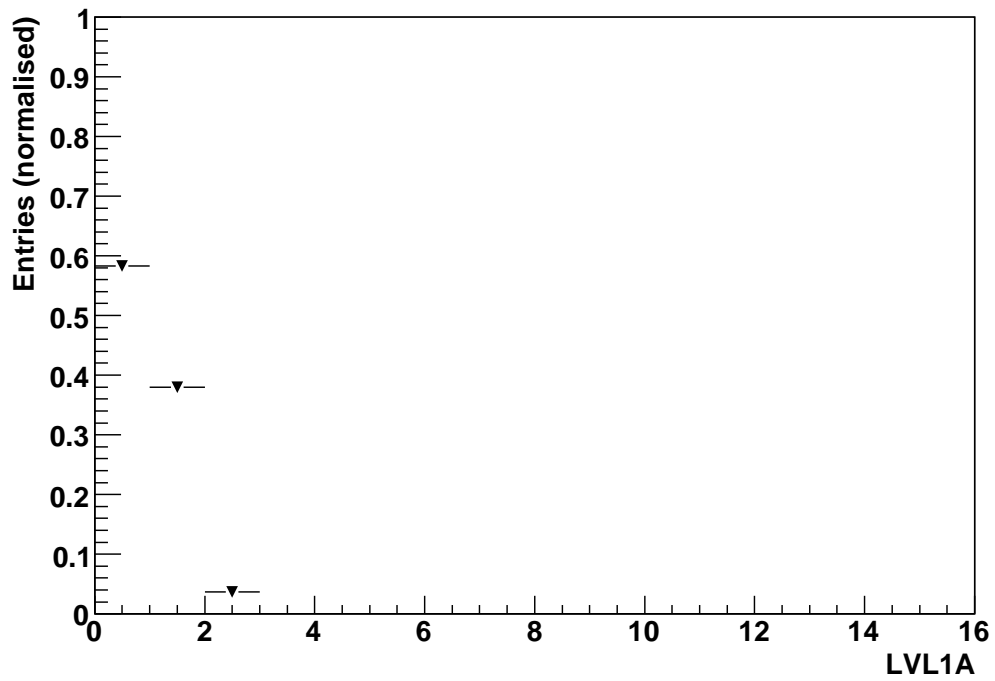
Figure 4.6: Finely binned LVL1A distribution for module 511665 (see Figure 4.5) rebinned into 25 ns bins. Unshifted output from simulation with TimeZero set to 15 ns.
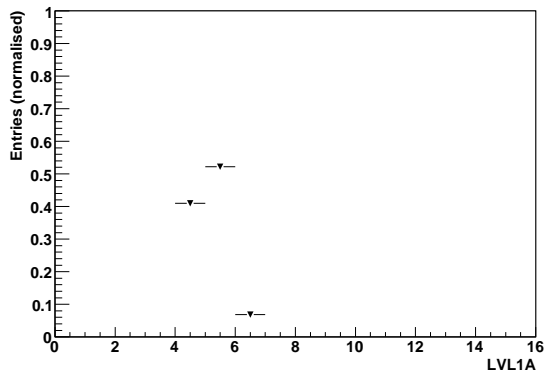
(a) TimeZero = 120 ns.
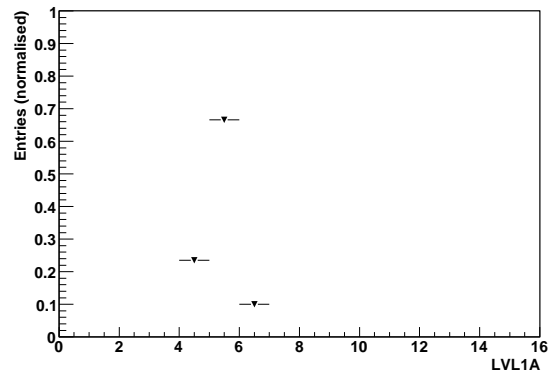
(b) TimeZero = 125 ns.
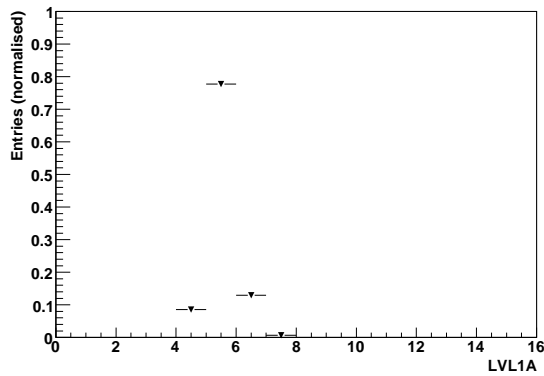
(c) TimeZero = 130 ns.
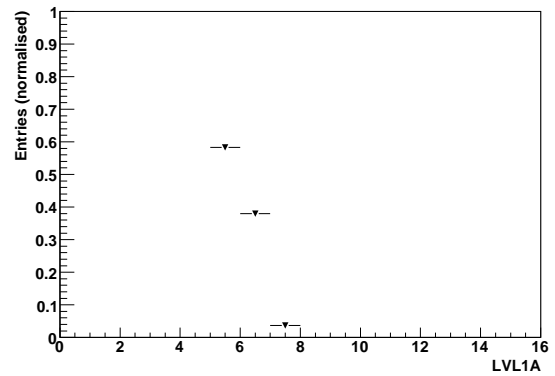
(d) TimeZero = 140 ns.

Figure 4.7: Finely binned LVL1A distribution for module 511665, shifted to different positions and rebinned into 25 ns bins. The resulting histogram has to be compared with the measured LVL1A distribution in Figure 3.2.

Simulation and data are compared using a χ^2-fit. If N_i is the number of entries in the LVL1A distribution from the data, $\Delta N_i = \sqrt{N_i}$ is the statistical error on the bin entry i. $N_{i,\text{shifted}}$ and $\Delta N_{i,\text{shifted}} = \sqrt{N_{i,\text{shifted}}}$ are the number of entries in the shifted LVL1A distribution from simulation and the associated bin error for bin i after the 25 ns-rebinning. The combined error is $\widetilde{\Delta N_i} = \sqrt{(\Delta N_i)^2 + (\Delta N_{i,\text{shifted}})^2}$ and the χ^2-function becomes:

$$\chi^2 = \sum_{\substack{\text{all LVL1A bins,} \\ i=0}}^{16} \left(\frac{N_i - N_{i,\text{shifted}}}{\widetilde{\Delta N_i}}\right)^2 = \sum_{\substack{\text{all LVL1A bins,} \\ i=0}}^{16} \frac{(N_i - N_{i,\text{shifted}})^2}{N_i + N_{i,\text{shifted}}}, \qquad (4.2)$$

where bins with $N_i = 0$ were ignored.

The fit routine uses the TMinuit package of ROOT [38, 40]. Several calls of the SEEK algorithm search for the χ^2-minimum in a wide range of the fit parameter, which is the offset TimeZero in the timing in Equation 3.2. The number of calls for SEEK was set to 100, the initial starting position was set arbitrarily to 137 ns. The MIGRAD algorithm is then used to find the exact position of the minimum by evaluating Equation 4.2, starting with the best result from the SEEK routine. Minuit's IMPROVE algorithm, which should perform a refined search for the minimum, was tested but did not result in any improvements. The reason is given below.
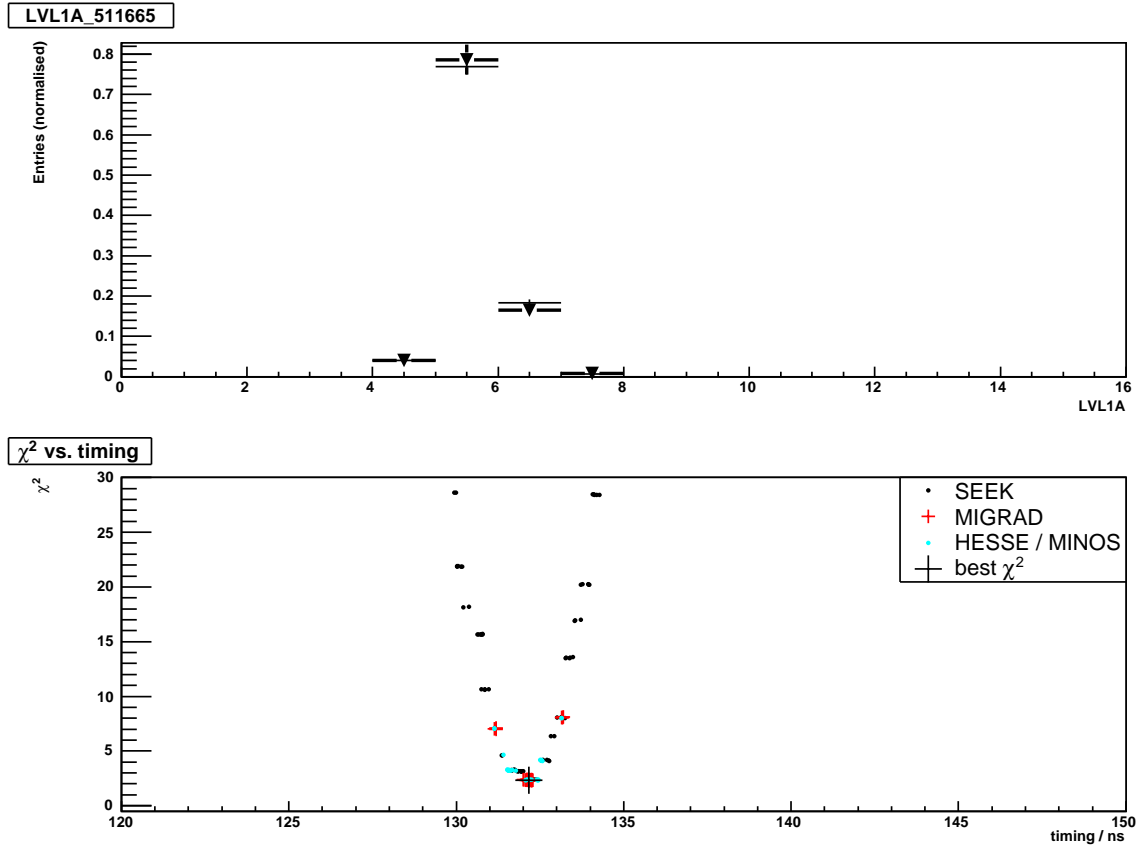
Figure 4.8: Fit result for module 511665. The data, overlayed with the best fit histogram for the LVL1A distribution (upper plot), the corresponding χ^2-distribution (lower plot).

In Figures 4.8 and 4.9, the fit on module 511665 is shown. The upper plot shows the LVL1A distribution taken from the data overlayed with the fit function at minimum χ^2 (bold lines). The plot below illustrates the operation of the fit routine. Each calculation of a χ^2 during the fit (by SEEK, MIGRAD or the error calculation algorithms HESSE and MINOS) is shown by one point. Zooming into the minimum (see Figure 4.9) shows clearly the 0.25 ns steps, that are expected from the binning of the finely binned LVL1A distribution from the simulation. This specific structure of the χ^2-function will be called step function henceforth and the 0.25 ns-wide intervals will be called levels of the function. Shifting the fit function by less than 0.25 ns (as Minuit does) can not lead to a different value in χ^2 and hence the fit quality does not change. Because the minimum step had already been found by the MIGRAD routine, IMPROVE had to fail and was no longer used, since no smaller χ^2 could be calculated around the MIGRAD minimum.
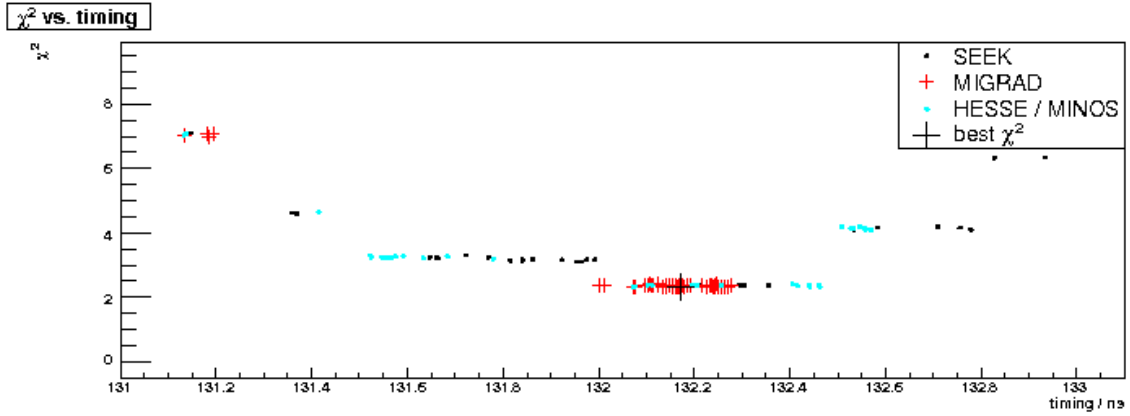
Figure 4.9: Fit result for module 511665. Zoom into the χ^2-minimum. The structure of a step function is clearly visible.

The number of degrees of freedoms (ndf) for the fit is equal to the number of filled bins in the LVL1A distribution decreased by one, since there is one parameter to be fitted. The distribution of the ratio χ^2/ndf should show most entries around one. In Figure 4.10, the distribution of this ratio is presented and such a peak can be seen. Thus, the fit-function 4.2 seems to be chosen correctly.

The error on the fit parameter was calculated by calling the HESSE algorithm by default after performing the MIGRAD minimisation. HESSE calculates the full second-derivative matrix of the χ^2-function with respect to the free parameters by finite differences. This second derivative matrix is evaluated with those parameter values, that were calculated for the minimum of the function. It is then inverted to obtain the error matrix. In other words, the curvature at the minimum is calculated and a parabolic shape of the χ^2-distribution is assumed [41]. The MINOS algorithm was explicitly executed after HESSE to obtain a more exact error. This algorithm searches for the value of the fit parameter that leads to a χ^2 which is the minimum χ^2 increased by one and thus corresponds to one standard deviation in the fit parameter (see Equation 4.2). Different values for the positive and negative error can usually be obtained [41]. If any of the error finding algorithms terminates successfully,

this error is taken, otherwise the last (and assumed best) estimate is stored.

Since the χ^2 is a step function in this case, the second derivative is hard to calculate by HESSE and $\chi^2 + 1$ is likely not to be found by MINOS and hence, both algorithms would abort, which indeed happened in most cases. The distribution of the final errors calculated by the algorithms is presented in Figure 4.11. Since there were severe problems in calculating them, these errors were not taken as the uncertainties of the timing results: another method (simplifying the HESSE idea) was sought for and this revised algorithm for the error determination is presented in Section 4.3.

The true minimum position could not be found within the lowest level since the χ^2-values do not differ within a level. For this reason, all the results, calculated directly with the Minuit-based algorithm, need to be given a systematic error of 0.25 ns.

A more exact estimation on the best TimeZero is done by finding the centre of the lowest χ^2-level and applying the statistical uncertainty of 0.25 ns / $\sqrt{12} \approx 0.072$ ns to it: The probability $p(t)$ of finding the true χ^2-minimum on the lowest level (with width Δt) of the χ^2-function is uniformly distributed along this level ($p(t) = const = c$). Thus, the expectation value $\bar{t}$ and its variance $\sigma_{\bar{t}}$ can be calculated:

$$
\begin{aligned}
1 \quad &= \int_0^{\Delta t} c \, dt \quad = c \, \Delta t \;\Rightarrow\; c = \frac{1}{\Delta t} \quad \text{(normalisation)}, \\
\bar{t} \quad &= \int_0^{\Delta t} \tfrac{1}{\Delta t} \, t \, dt \quad = \frac{1}{2} \, \Delta t = t_{\text{centre}} \quad \text{(centre of a level)}, \\
\sigma_{\bar{t}}^2 \quad &= \overline{t^2} - \bar{t}^{\,2} \quad = \int_0^{\Delta t} \frac{1}{\Delta t} \, t^2 \, dt \; - \; \frac{1}{4} \, (\Delta t)^2 = \frac{1}{12} \, (\Delta t)^2, \\
\Rightarrow\; \sigma_{\bar{t}} = \sigma_{\text{centre}} \quad &= \frac{\Delta t}{\sqrt{12}}.
\end{aligned}
\tag{4.3}
$$

The uncertainty from Equation 4.3 needs to be assigned to each central value, that is calculated.
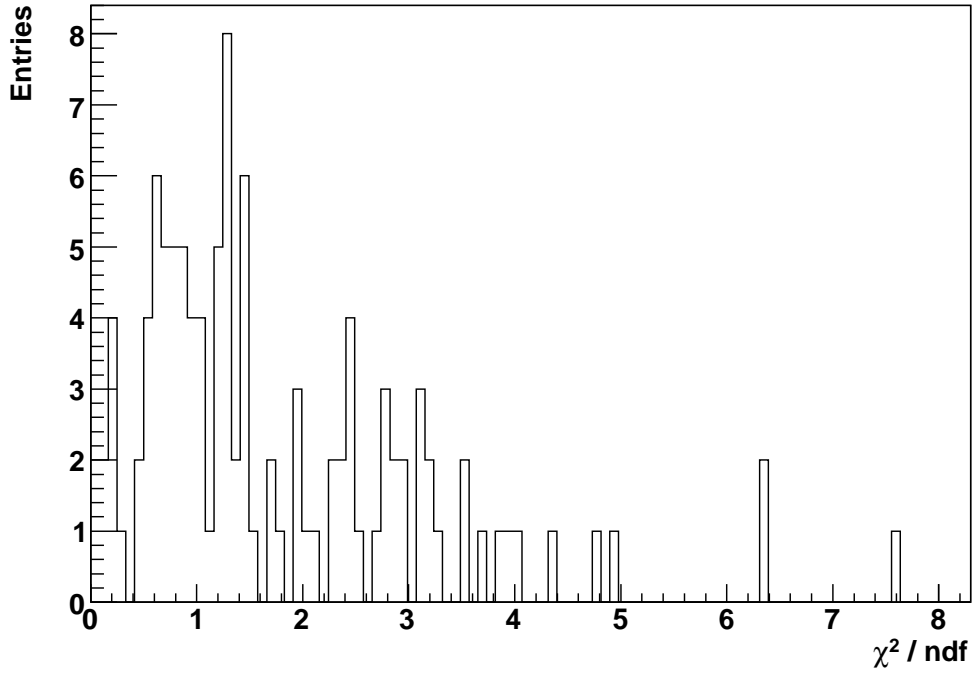
Figure 4.10: Ratio of the minimum χ^2 to the number of degrees of freedom. The distribution contains the ratios of all modules that could be fitted successfully.
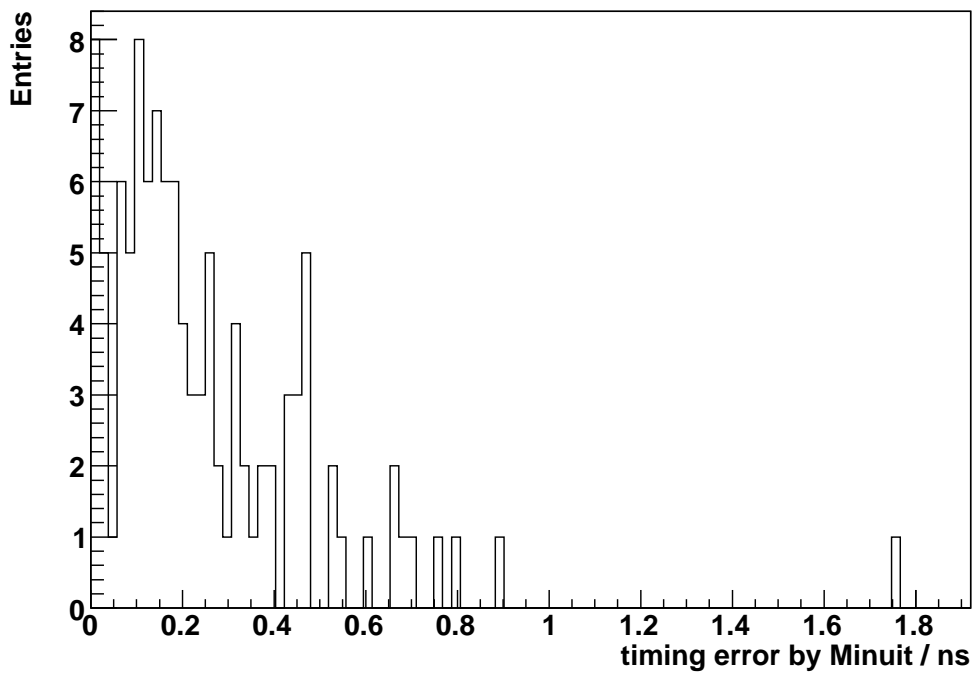

Figure 4.11: Distribution of the error on TimeZero as directly calculated by Minuit.

4.2.1 Dependence of the Timing Results on the Fit Run

In order to check whether the fit routine based on Minuit reliably finds the χ^2-minimum, another fit run was performed. In the SEEK routine, a random number generator is employed to arbitrarily choose points in a wide region in the parameter space. In this way, the approximate location of the χ^2-minimum is estimated. The only applied condition, which was the random seed, was changed from the initial $450\,000\,000$ to the value of $12\,345$ as a check in this second fit run.

The differences in the timing results are presented in the Figures 4.12(a) and 4.12(b). Except but two entries (where one is not shown), all differences are smaller than 0.25 ns in Figure 4.12(a), which illustrates the direct output of Minuit's calculation for the position of the minimum. This leads to the conclusion that for both fit runs, the same minimum χ^2-level was found. Since the function has the shape of a step function, the parameter value (the timing result) may vary within the width of one χ^2-level.

The two entries with a difference greater than 0.25 ns were checked and it was found that in one of the fit runs compared, the SEEK method did not cover the minimal χ^2-level, which means that the MIGRAD algorithm did not search in that region at all. Running the fit routine more than one time with different seeds or increasing the number of calls for the SEEK routine in the Minuit random generators appears to be an adequate method to exclude this problem.

In Figure 4.12(b), the central values, calculated from the entries that form the smallest χ^2-level, are compared. The distribution is significantly smaller than the non-centered results in Figure 4.12(a), as expected. Ideally, the distribution of the differences for the central values would be a needle at zero. Because Minuit does not necessarily calculate the $\chi^2_{\mathrm{minimum}}$ values at the very edges of the lowest level, its width is likely to be underestimated and therefore the distribution of the central values is smeared out in a Gaussian shape, with its centre consistent with zero. A scan of the χ^2-function, which is based on a random number, reveals a problem: the full parameter region around the χ^2-minimum will probably not be covered densely enough for some modules. For this reason, the algorithm was altered slightly, which will be described in the next section.

The algorithms of Minuit SEEK, MIGRAD and HESSE/MINOS were employed to use the usual sequence in Minuit. If a continuous function is used in the fit rather than a step function, MIGRAD will probably lead to better results and a correct error estimation. A continuous fit function can be extracted from the data by writing the hit recognition times to the logfile during the digitisation step, as it was already performed [15]. Binning the fit histogram into bins with bin widths of less than 0.25 ns would require an increase of the `TimeBCN` to more than 255, which is not possible since this variable has only 8 bits in the software framework.

So, to estimate the errors, the final and assumed to be the best values for the errors, calculated by Minuit, from each of the two fit runs, were compared. Figure 4.13 shows the difference between the errors from the fit run with the random seed set to $12\,345$ and those of the fit run with the random seed set to $450\,000\,000$. It was found, that the deviation in the errors is up to 0.75 ns for most Pixel Modules. This additional error was added in quadrature to each of the uncertainties calculated directly by Minuit.
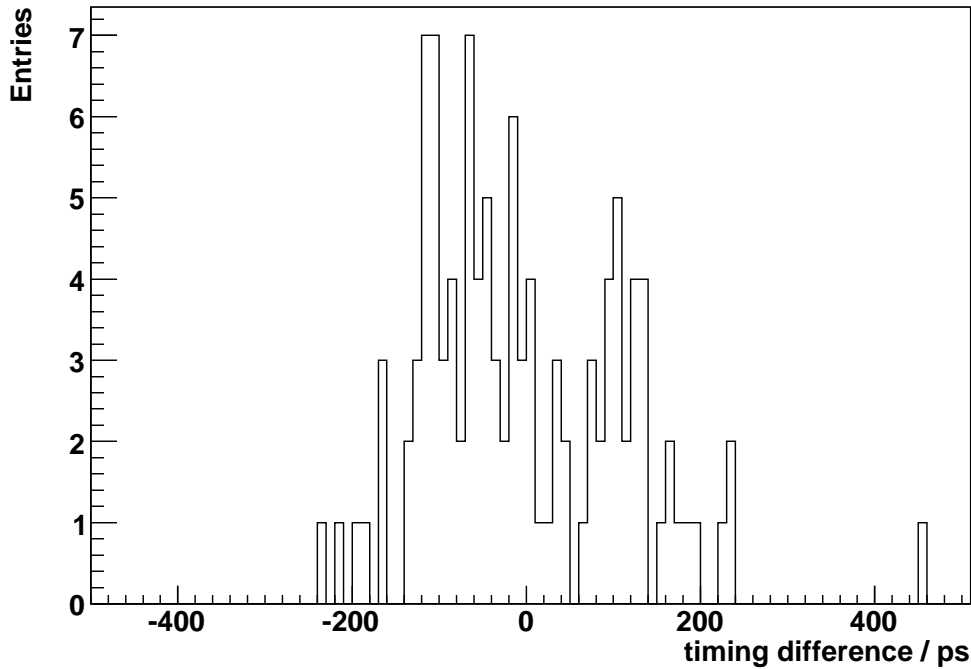
(a) Differences in the timing results as directly computed by Minuit for two different seeds in the random generator of the minimisation algorithm.
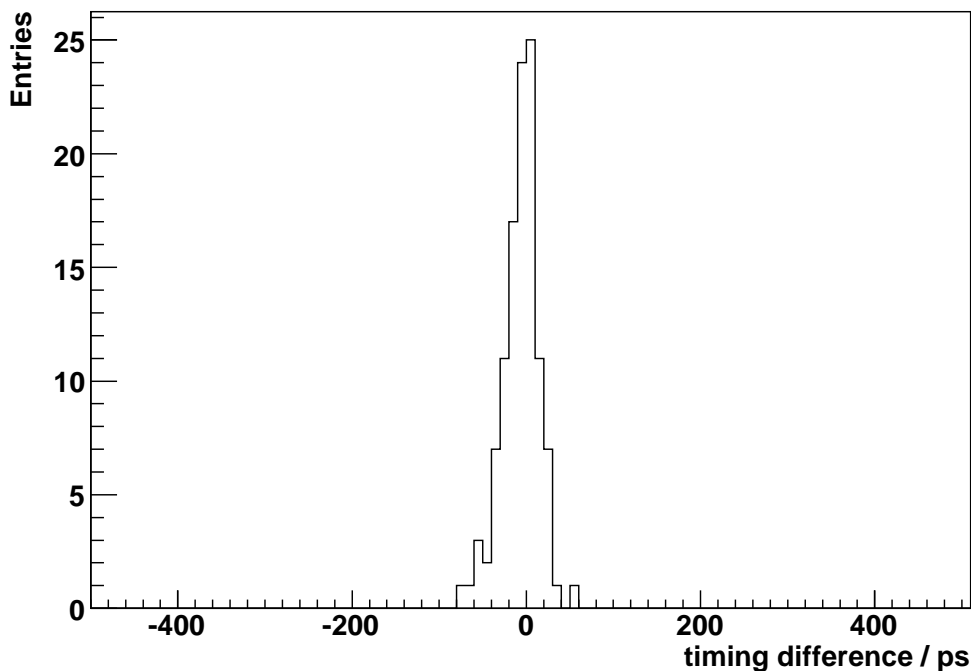
(b) Differences in the timing results after processing the centre-finding algorithm for two different seeds in the random generator of the minimisation algorithm.

Figure 4.12: Dependence of the fit result on the seed of the random generator used by Minuit. The differences between the timing results (delay (a) and central value (b)) from two runs calculated with different seeds are shown.
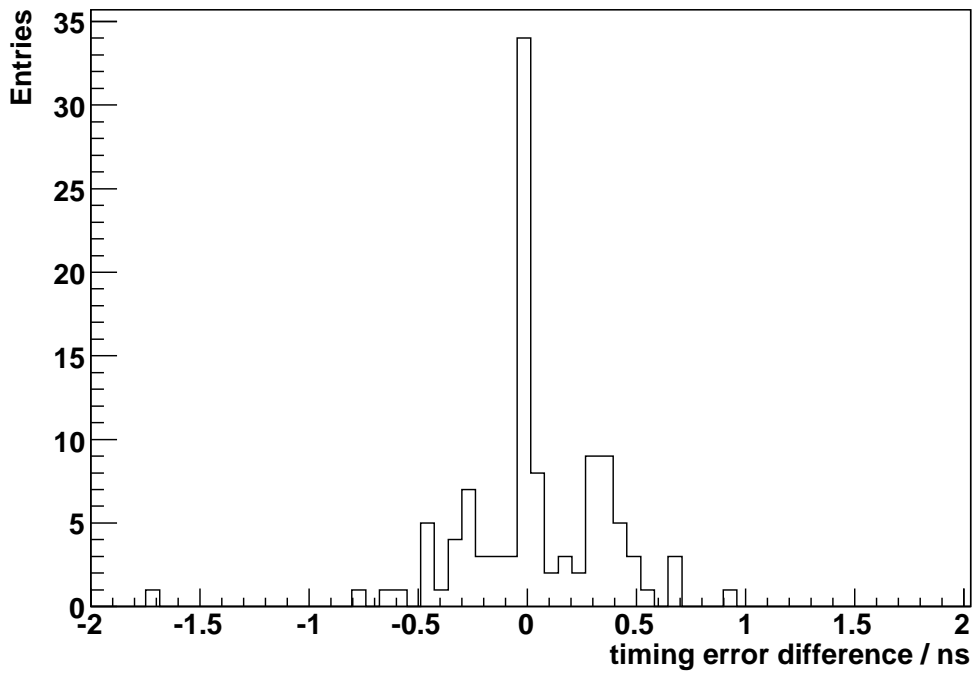
Figure 4.13: Differences of the timing errors, calculated by Minuit, for different random seeds in the random generator of the minimisation algorithm.

4.2.2 Dependence of the Timing Results on the Bin Width of the Fit Histogram

The LVL1A fit functions originate from the finely binned LVL1A distributions from simulation (Figure 4.5 and Section 4.2). The dependence of the bin widths of these finely binned histograms on the timing results will be discussed in this section. To investigate further, another two runs of the fit algorithm were performed. One step was added in computing the χ^2-value: before the finely binned LVL1A histogram from the simulation was shifted and rebinned into 25 ns-wide bins, it was first binned into larger bins (0.5 ns-wide and 1.0 ns-wide bins). The differences between the central values computed are shown in Figures 4.14(a) and 4.14(b) (central value results from the coarse binning minus central value results from the small binning). A 0.5 ns-wide bin may touch up to three 0.25 ns-wide bins. Therefore, three peaks are expected in the differences at intervals of 250 ps. Because the bins of minimum χ^2 are not always fully covered by the Minuit algorithm, their widths are likely to be underestimated. The detected central values may then vary around the true central values like Gaussians. Thus, the differences between the results from the two runs will have a Gaussian smearing, too. This is all confirmed by the analysis (Figure 4.14(a)). The same conditions hold for the fit run with an additional 1.0 ns-wide binning of the finely binned LVL1A function. Five 0.25 ns-wide bins can be touched by one of the wider bins and therefore, five Gaussian smeared peaks are expected and can be detected (Figure 4.14(b)). Nevertheless, in both plots, a shift of the peaks to positive values in the difference can be observed (the timing results from the coarse intermediate binning are biased to larger values than the results for the 0.25 ns-wide initial binning). This was assumed to be due to a preference of Minuit while scanning the parameter space but could not be clarified at this point (therefore see Section 4.3).

For each intermediate binning, there were two modules with a larger difference in the timing results than expected. For the additional 0.5 ns-wide binning these were 512705 and 510776 and for the additional 1.0 ns-wide binning 510945 and 510346. A closer look at these modules showed that the χ^2-functions each had a subsidiary minimum, that could not be seen in the coarser resolution. This subsidiary minimum originated from the low statistics in the simulation. So, these effects can be detected by increasing the intermediate bin width and executing another fit run.

As with the uncertainties in the fit runs with different seeds, here again the differences in the errors were calculated in order to confirm the systematic uncertainty, caused by the abortions of the error finding algorithms (HESSE and MINOS). The distribution of these differences is shown in Figures 4.15(a) and 4.15(b). The deviation of the differences also varies in a region of up to 0.75 ns in this comparison and thus, an additional systematic uncertainty of $\sigma_{\mathrm{syst.}} = 0.75$ ns seems to be justified, when working with the results with the coarse intermediate binning.
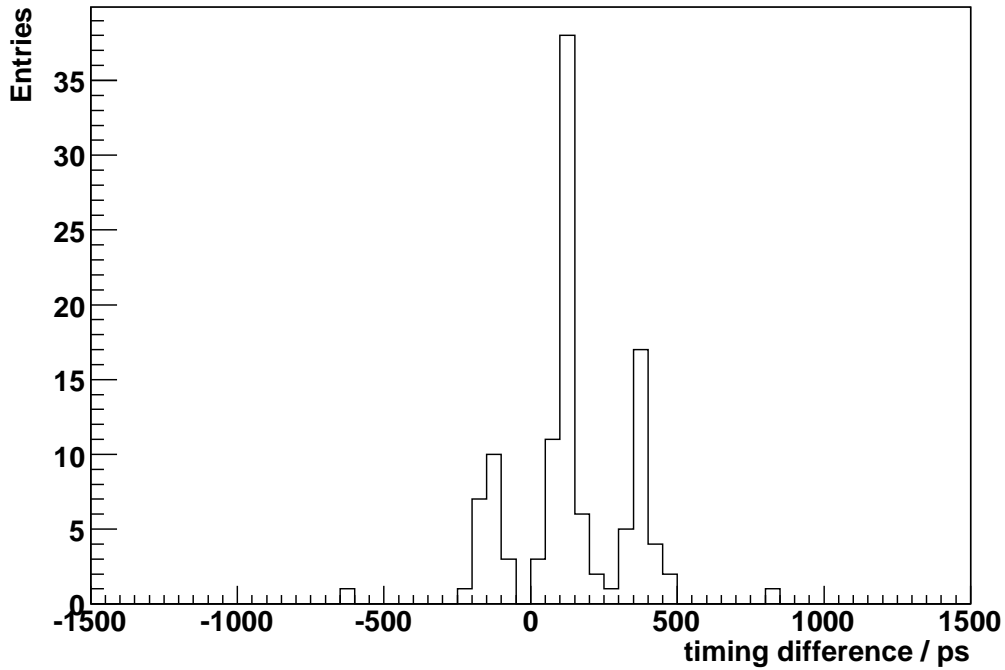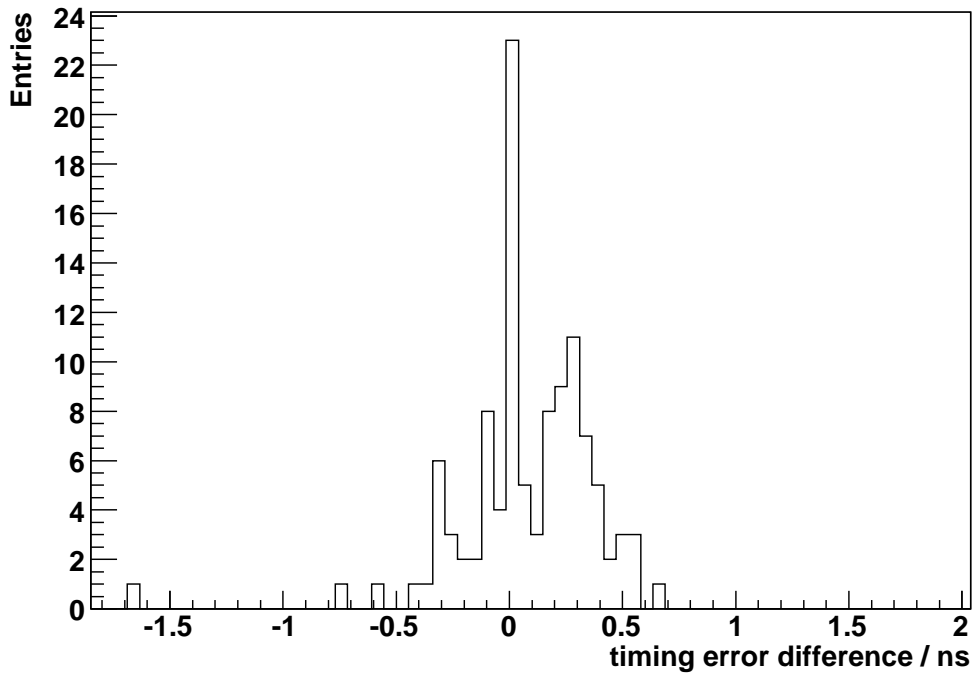
(a) Coarse intermediate binning performed with 0.5 ns-wide bins.
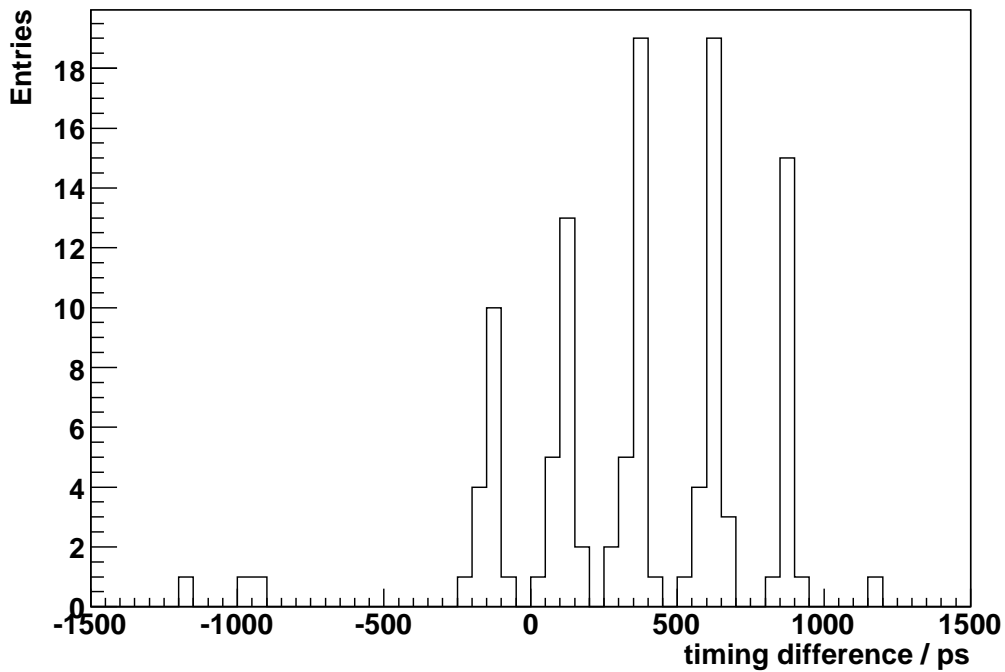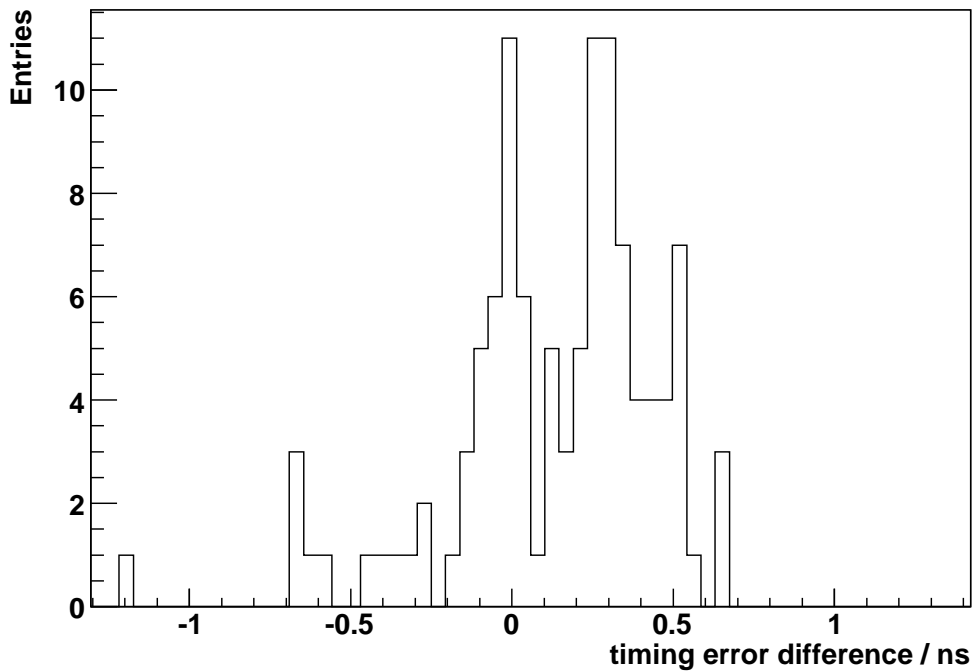

(b) Coarse intermediate binning performed with 1.0 ns-wide bins.

Figure 4.14: Dependence of the fit result on the intermediate bin-width of the finely binned LVL1A distribution from the simulation. The differences between the timing results from a coarse intermediate binning and the 0.25 ns-wide initial binning are shown.

(a) Coarse intermediate binning with 0.5 ns-wide bins.

(b) Coarse intermediate binning with 1.0 ns-wide bins.

Figure 4.15: Dependence of the errors of the fit results on the intermediate bin-width of the finely binned LVL1A distribution from the simulation. The difference between the timing results from a coarse intermediate binning and the initial 0.25 ns-wide binning is shown.

4.2.3 Summary of the Minuit-based Fit Algorithm

This version of the fit algorithm used standard routines of Minuit for the determination of the timing, by finding the position of a χ^2-minimum and for the calculation of the error on the timing parameter. Both calculations revealed problems: the coverage of the lowest levels in the χ^2-function by the MIGRAD algorithm was insufficient. The spread of the bin width of the lowest χ^2-level can be seen in Figure 4.17(a). This caused an underestimation of the width of the lowest levels and the central values calculated will deviate from the true central values. Each central value needs to have the uncertainty $\sigma_{\text{centre}} = 0.072$ ns assigned for statistical reasons (Equations 4.3). Nevertheless, the minimum χ^2-level could be detected reliably.

The ensuing error calculation, performed by Minuit, did not converge in most cases. Both of the algorithms, HESSE and MINOS, were tested with the same result. In order to determine the error matrix, these algorithms need to calculate the second derivative of the χ^2-function [42]. In the case of a step function, this is not possible and the error calculation fails. As an estimate for the error, the errors of two fit runs with different seeds in the random generator of the SEEK algorithm were compared and it was observed, that they differ from each other by up to 0.75 ns for most modules. Consequently, $\sigma_{\text{syst.}} = 0.75$ ns is added quadratically to any error σ_{Minuit}, calculated by Minuit's algorithms. After this process, the Pixel Module timing is given in Equation 4.4, where the error is heavily dominated by $\sigma_{\text{syst.}}$:

$$\text{timing} = t_{\text{centre}} \pm \sqrt{\sigma_{\text{centre}}^2 + \sigma_{\text{Minuit}}^2 + \sigma_{\text{syst.}}^2}. \tag{4.4}$$

4.3 Revised Calculation of the Pixel Module Timing

The fit algorithm using only standard Minuit routines had certain disadvantages for solving this specific problem, which were mainly due to the step function shape of the χ^2-function. The algorithm was therefore revised, as described in this section.

The revised fit algorithm searches for the position of the lowest χ^2-level with the SEEK algorithm of Minuit (up to 100 calls). Then, in an adjustable region (set to 2 ns) around that coarsely determined minimum, the χ^2-function is evaluated in small steps (set to 100 steps in the interval) and the centre-finding algorithm is run on these data points. In this way, it is ensured, that the lowest levels are fully covered and evaluated. Figure 4.17(b) illustrates the distribution of the calculated widths of the lowest levels. The spread of the distribution is dramatically decreased and the peak is located close to 0.25 ns compared to the distribution in Figure 4.17(a). The central value is found at its true position independently of the random seed used in the SEEK algorithm, which is proved by Figure 4.16. The distribution of the differences between the central values of two runs (each with different random seed) of the revised fit algorithm is shown. With about half the width, the distribution is considerably smaller than that shown in Figure 4.12(b), in which the central values of two fit runs of the Minuit-based algorithm were compared. The centre-position of the lowest χ^2-level is taken as the timing $t_{\text{centre, revised}}$.

After the precise evaluation of the χ^2-function around the minimum and the determination of the centre at $t_{\text{centre, revised}}$, the centre-coordinates of the two levels above and the two levels below the minimum are calculated. This is done by evaluating the χ^2-function at
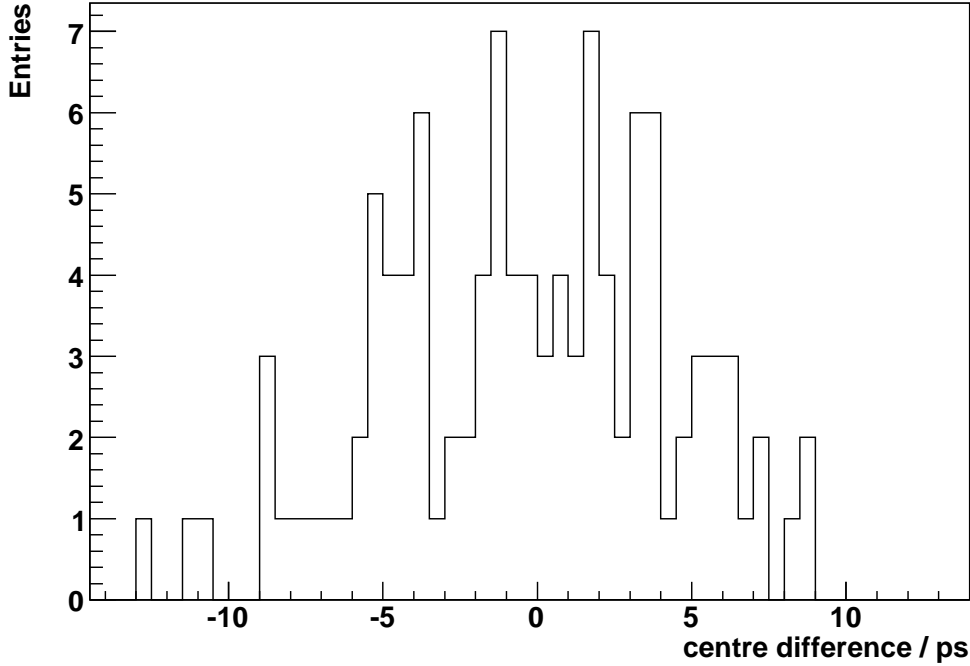
Figure 4.16: Differences of the central values of the lowest χ^2-levels between two runs with different seeds, calculated by the revised fit algorithm. This uncertainty is negligibly small.

$t_{\text{centre, revised}} \pm 0.50$ ns and $t_{\text{centre, revised}} \pm 0.25$ ns. A parabola is fitted to these five centre-coordinates, which were given equal weights

$$\chi^2_{\text{parabola}} = (p_0 \cdot t - p_1)^2 + p_2, \tag{4.5}$$

where t is the timing and p_0, p_1 and p_2 are parameters. The coordinate of the minimum of the parabola can easily be calculated as $\chi^2_{\text{par., minimum}} = p_2$ at the minimum position $t_{\text{par., minimum}} = p_1/p_0$. The error on the timing parameter is now calculated by looking for the value of t at which the parabola takes the value $\chi^2_{\text{par., minimum}} + 1$. The interval $\sigma_{\text{par.}}$ to the minimum position p_1/p_0 is equivalent to one standard deviation for t, resulting from Equation 4.2. Practically, this is exactly what Minuit tries to do in the HESSE algorithm, but reduced to a few datapoints from the χ^2-function. The distribution of the errors calculated from the parabolic fits is shown in Figure 4.20. The comparison to Figure 4.11 reveals, that most of the very small errors given by Minuit, which appeared unphysical, have now increased to reasonable values. In Figure 4.18 the result of the parabolic fit for module 511665 is shown. It can be seen, that all χ^2-levels are well covered and that the parabola describes the χ^2-function around the minimum.
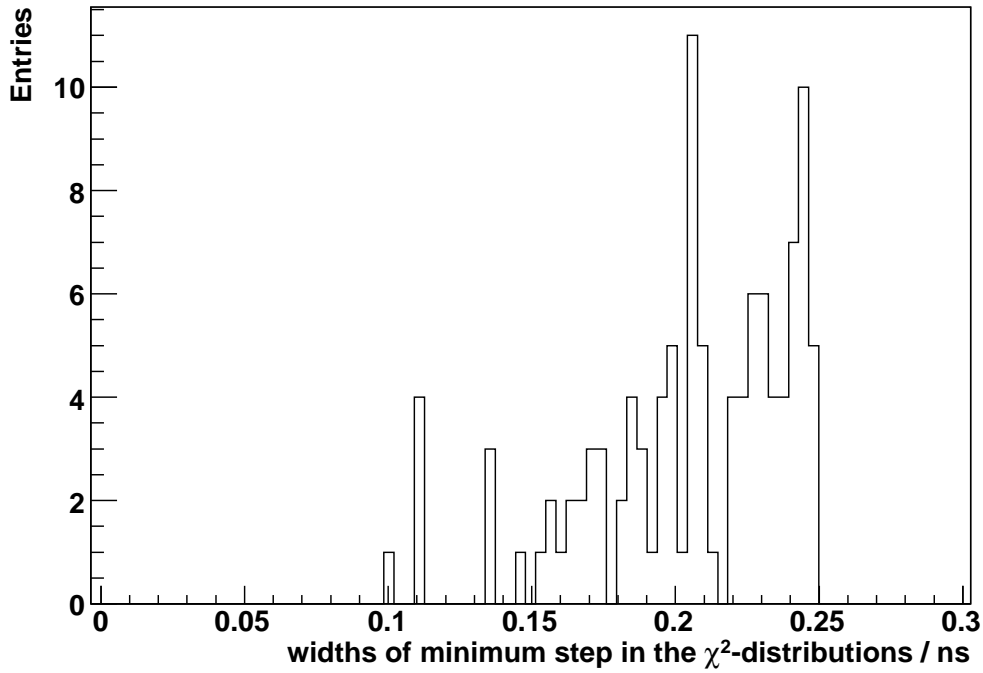
(a) Distribution of the widths of the minimum levels in the χ^2-functions as determined by the Minuit-based algorithm (run with random seed of 450 000 000).
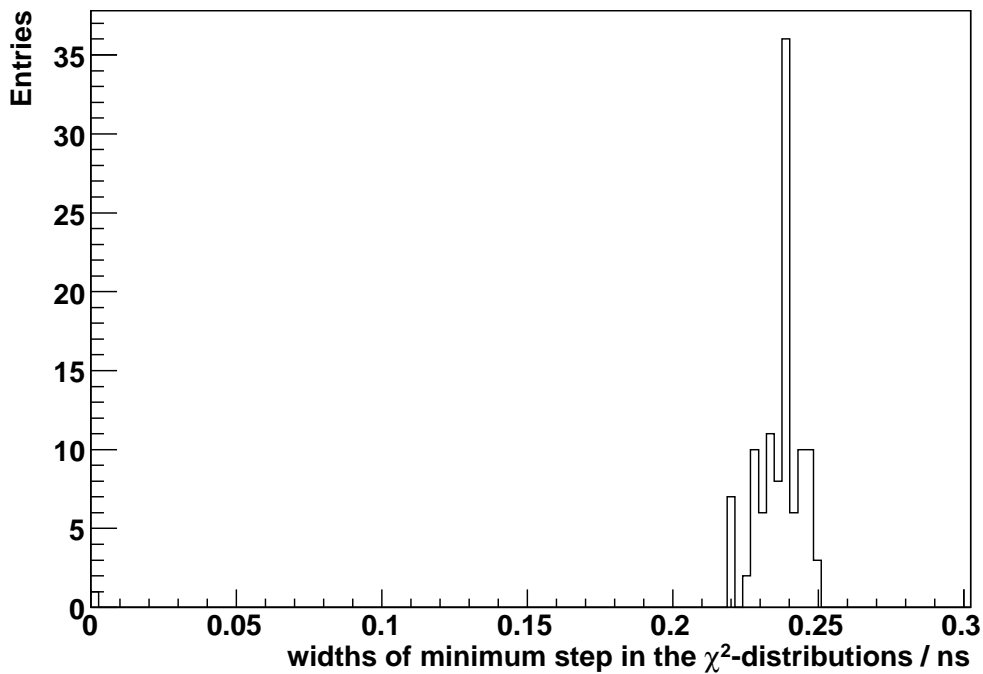
(b) Distribution of the widths of the minimum levels in the χ^2-functions as determined by the revised fit algorithm (run with random seed of 450 000 000).

Figure 4.17: Determination of the width of the lowest level of the χ^2-function in the two algorithms.
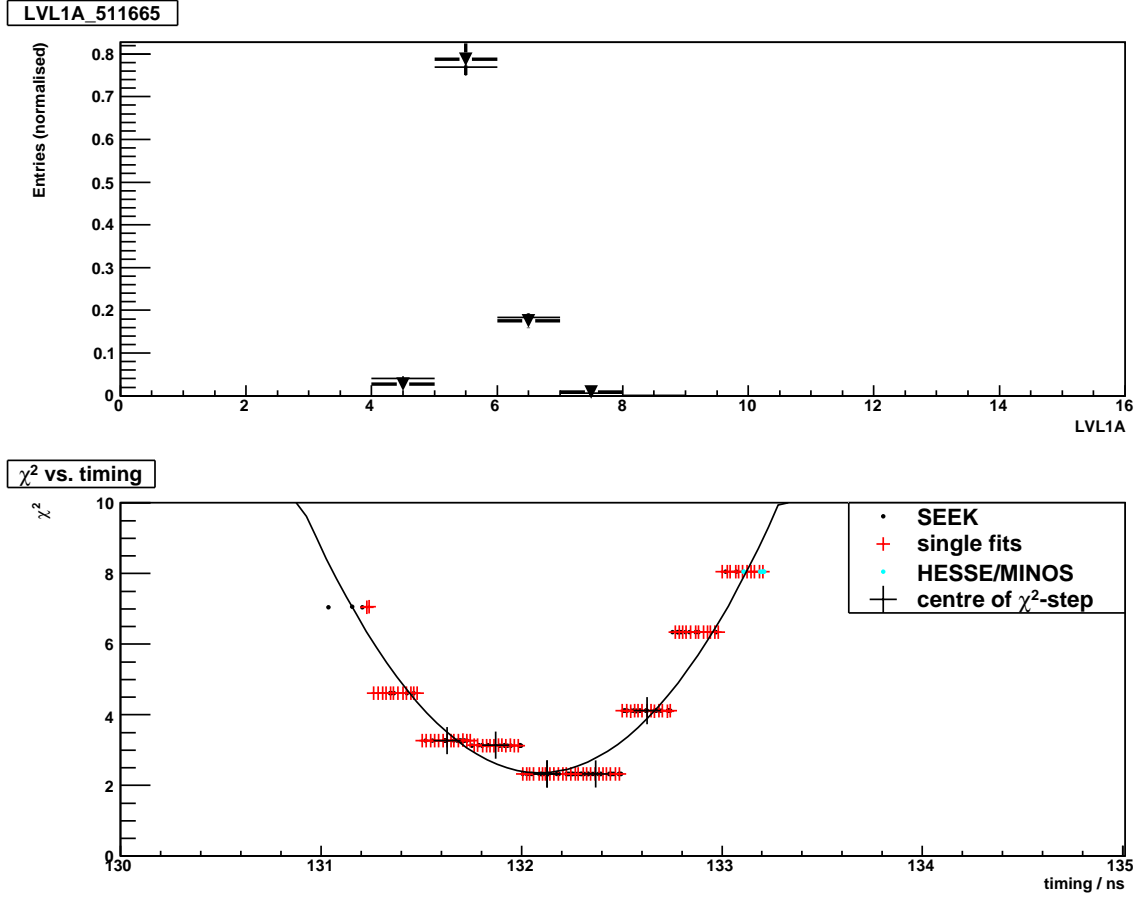
Figure 4.18: Fit result of the revised algorithm for module 511665. The LVL1A distribution from the data overlayed with the best fit function in the upper plot. Zoomed view into the χ^2-minimum in the lower plot. A parabolic fit was performed on the central values of the four χ^2-levels around the minimum and the minimum level itself.

The difference $\sigma_{\text{diff.}} = t_{\text{centre, revised}} - t_{\text{par., minimum}}$ between the minimum, calculated with the parabola, to the central value of the lowest χ^2-level is taken as another uncertainty and is added quadratically to $\sigma_{\text{par.}}$. If a χ^2-distribution is strongly asymmetrical, the parabola may not describe it very well and the minimum is fitted in a distance to the lowest χ^2-level. This uncertainty, caused by an asymmetric shape, is taken into account by $\sigma_{\text{diff.}}$. The distribution of these differences is presented in Figure 4.19. It spreads to up to 0.6 ns. The final timing value from the revised algorithm yields:

$$\text{timing}_{\text{revised}} = t_{\text{centre, revised}} \pm \sqrt{\sigma_{\text{centre}}^2 + \sigma_{\text{par.}}^2 + \sigma_{\text{diff.}}^2}. \tag{4.6}$$

As with the Minuit-based algorithm, the dependence of the timing results on the bin width of the finely binned LVL1A distribution has been studied. Therefore, a fit run has been performed with a coarse intermediate binning of 1.0 ns instead of 0.25 ns. Since the centre-finding algorithm is much more precise in the revised version, the Gaussian smearing of the peaks in Figure 4.14(b) is likely to sharpen now. Figure 4.21 shows the differences of the
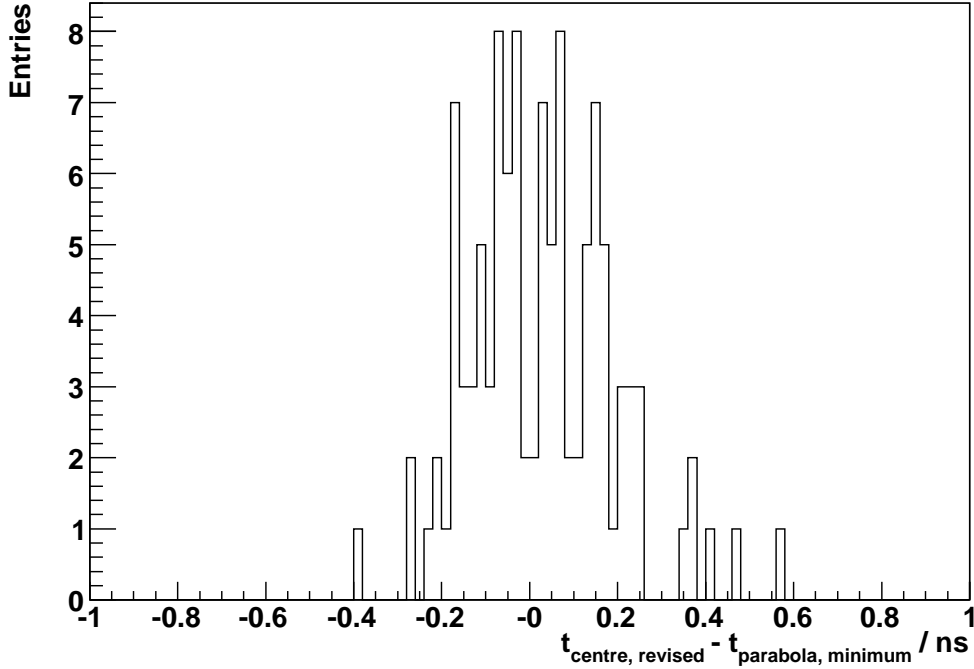
Figure 4.19: Differences between the minimum of the parabola and the central value of the lowest χ^2-level. This difference $\sigma_{\text{diff.}}$ is part of the uncertainty given to the timing results.

timing results, confirming the expectations. The timing results calculated with the coarse intermediate binning are also shifted to larger values as already observed in Section 4.2.2 with the Minuit-based algorithm. Since the scanning of the parameter space is no more left to Minuit, but is done manually in equally spaced steps, this cannot be the reason for the shift. The fit results for a set of modules (modules 510155, 510409, 510461, 510837, 513169, 513103) with a shift larger than 0.75 ns were looked at and it was found, that they all had a strongly asymmetric χ^2-distribution with the slope of the right-hand branch being less steep than the left-hand one. This explains the shift to larger results when binning more coarsely.

The timing results calculated with the revised algorithm need to be compared with the theoretical value of 130 ns given in Section 3.1.2 in Equation 3.1. Figure 4.22 illustrates the spread of the timing results around that value. In Appendix A, the Figures A.1, A.2 and A.3 reflect the results and their uncertainties separated for each disc of the endcap. Tables A.1, A.2 and A.3 summarise the calculated timing values and the errors assigned.
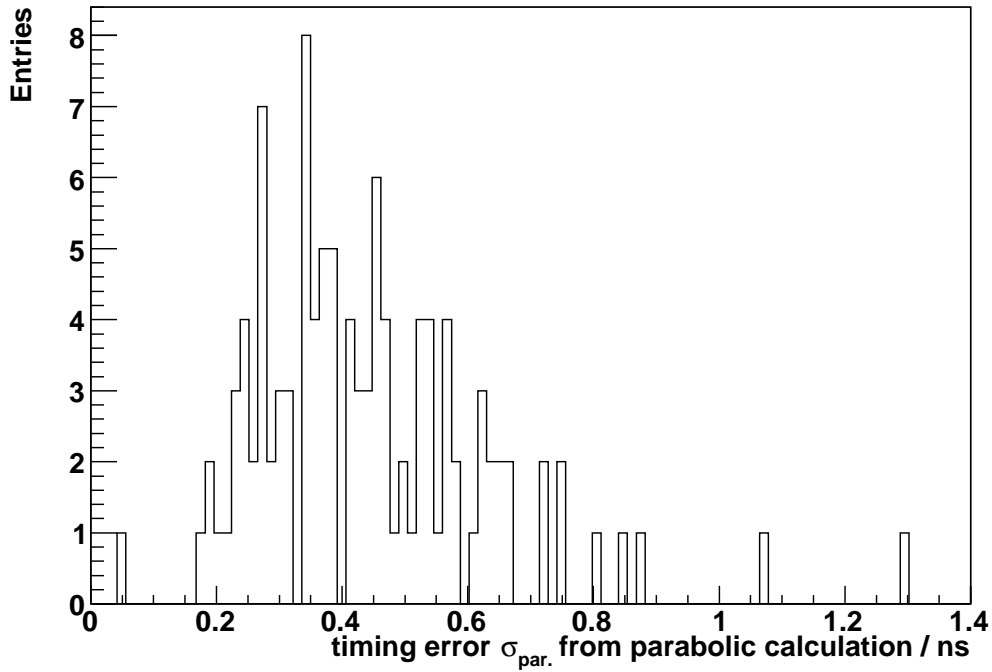
Figure 4.20: Distribution of the error $\sigma_{\mathrm{par.}}$ on the timing as calculated by the revised fit algorithm from the fit of a parabola.
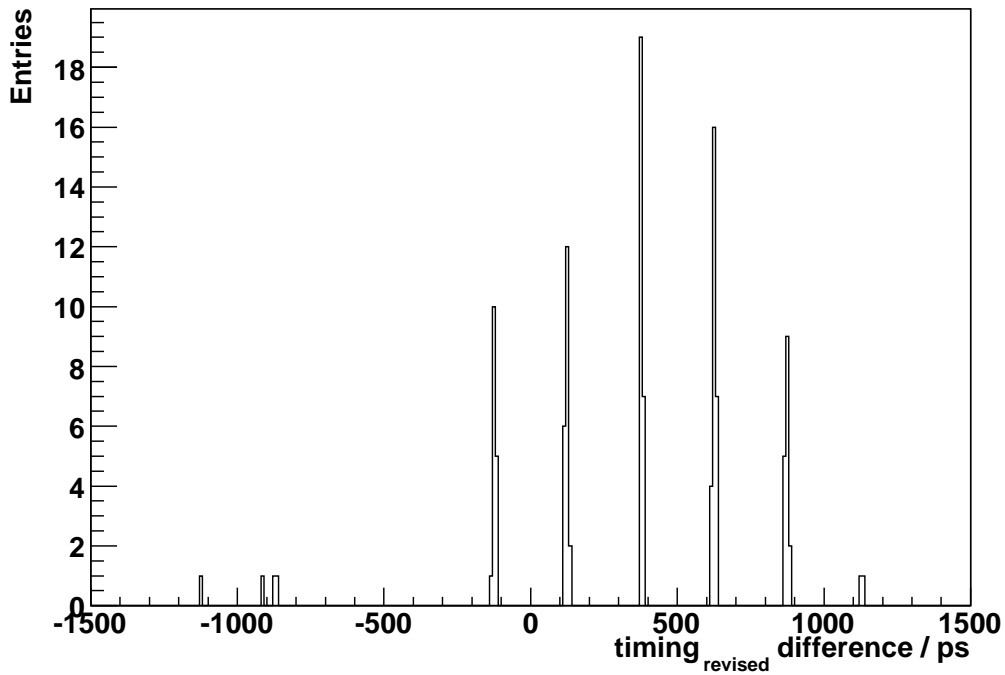

Figure 4.21: Distribution of the differences in the timing results for 1.0 ns-wide intermediate binning and the 0.25 ns-wide initial binning of the finely binned LVL1A distribution in the revised algorithm.
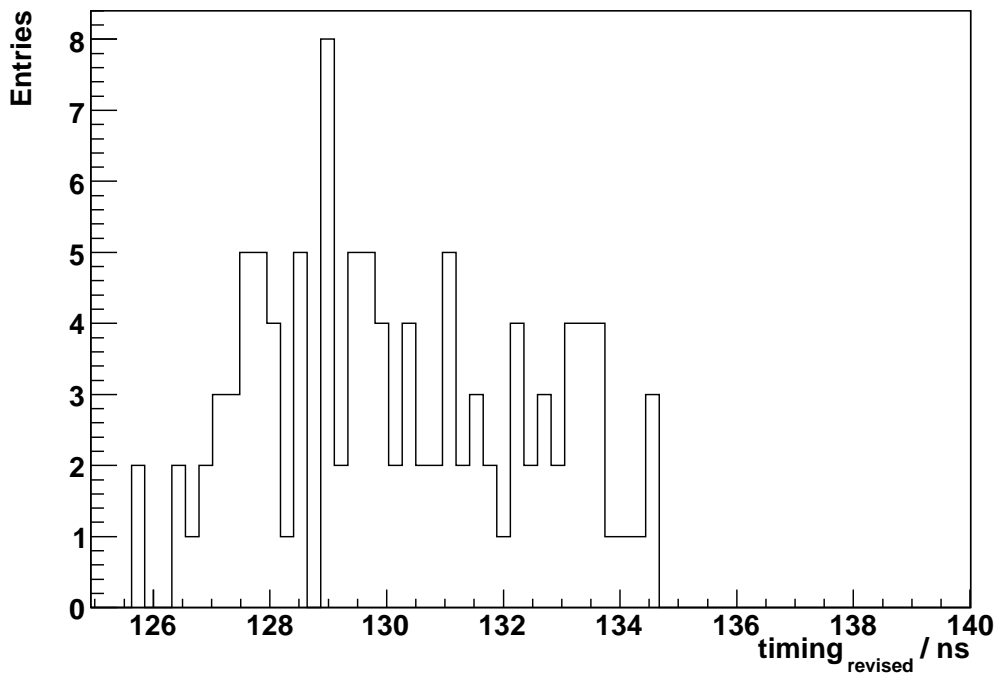
Figure 4.22: Distribution of the fit results for the Pixel Module timing (central value of the lowest χ^2-level as calculated in the revised algorithm).

4.3.1 Comparison of the Results with Existing Analyses

The current analysis should result in the same values for the timing as in previous analyses [15]. The differences in the results are presented in Figures 4.23, 4.24 and 4.25. The errors presented were calculated by combining the errors from both analyses through quadratic addition. The combined error from Equation 4.6 was used.
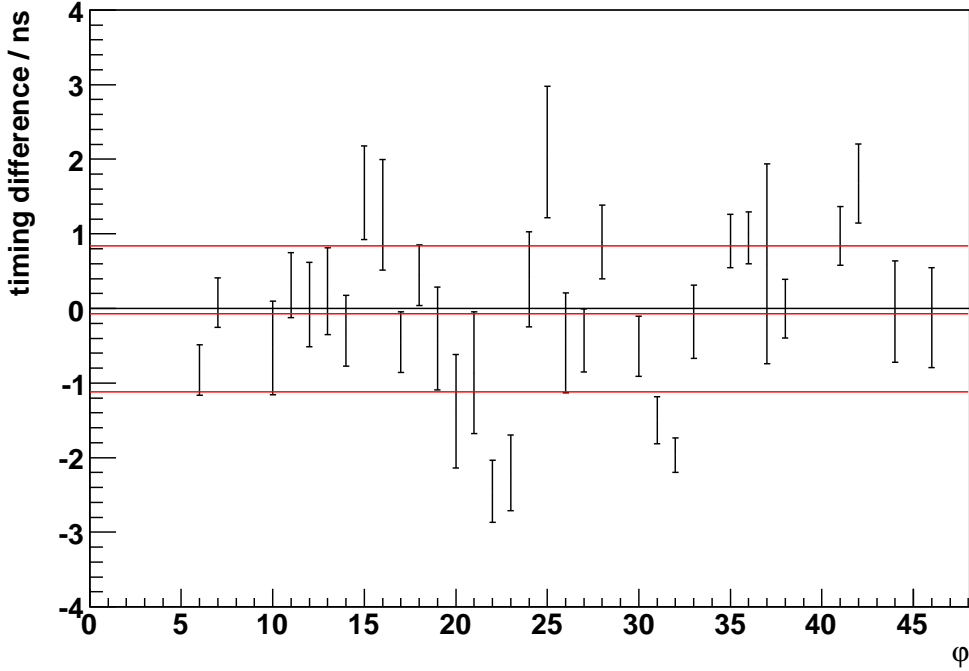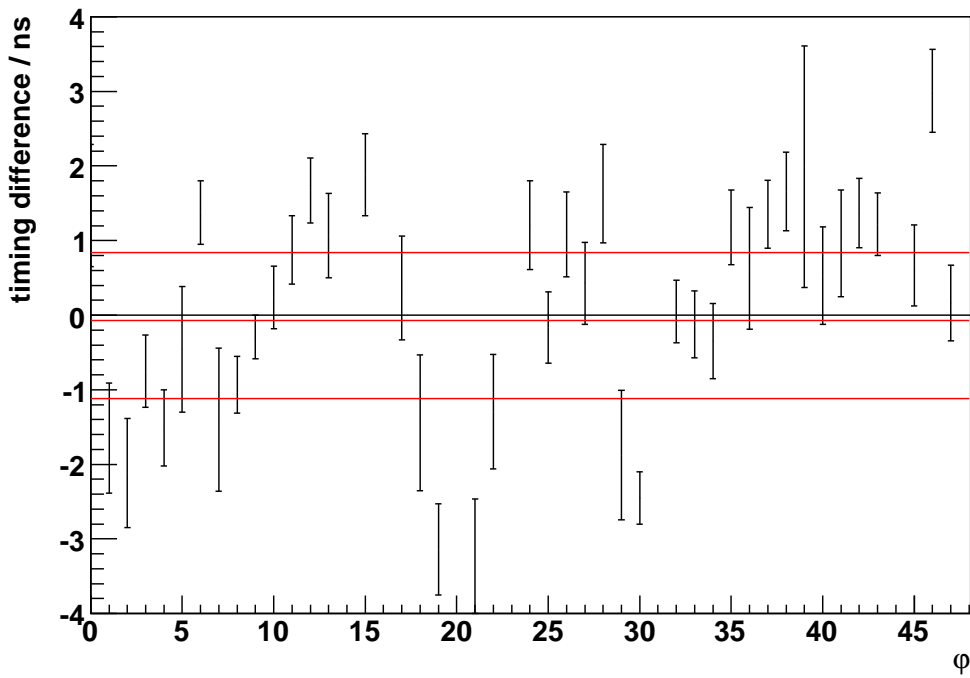

Figure 4.23: Differences between the reconstructed TimeZero for Disc 0 from this analysis and from [15]. The horizontal lines reflect the mean differences $\bar{d}^{+}$, $\bar{d}^{-}$ and the overall mean value $\bar{d}$ given in Equation 4.7.

The mean difference was calculated by evaluating $\bar{d} = \frac{\sum_i w_i d_i}{\sum_i w_i} \pm \sigma_{\bar{d}}$, where d_i describes the difference of the results for datapoint i, the weights are $w_i = \sigma_i^{-2}$ and the error is $\sigma_{\bar{d}} = \sqrt{\frac{\sum_i \sigma_i^2 w_i}{\sum_i w_i}} = \frac{1}{\sqrt{\sum_i w_i}}$. The error on the mean difference was calculated under the assumption that all errors are uncorrelated and may therefore be added quadratically. The same calculation was done separately for those differences above ($\bar{d}^{+}$) and below ($\bar{d}^{-}$) the overall mean value $\bar{d}$:

$$
\begin{aligned}
\bar{d}^{+} &= 0.84 \pm 0.06 \text{ ns}, \\
\bar{d} &= -0.07 \pm 0.05 \text{ ns}, \\
\bar{d}^{-} &= -1.12 \pm 0.07 \text{ ns}.
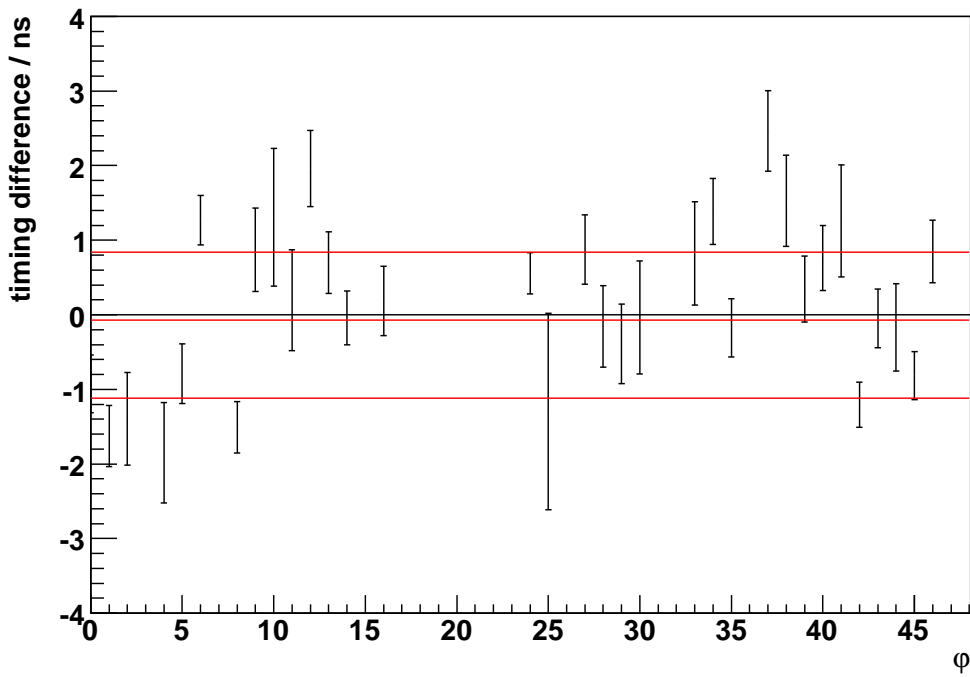\end{aligned}
\tag{4.7}
$$

Figure 4.24: Differences between the reconstructed TimeZero for Disc 1 to from this analysis and from [15]. The horizontal lines reflect the mean differences $\bar{d}^+$, $\bar{d}^-$ and the overall mean value $\bar{d}$ given in Equation 4.7.


Figure 4.25: Differences between the reconstructed TimeZero for Disc 2 from this analysis and from [15]. The horizontal lines reflect the mean differences $\bar{d}^+$, $\bar{d}^-$ and the overall mean value $\bar{d}$ given in Equation 4.7.

Deviant from the expectation, the differences vary in a region of about ± 1 ns around zero. This demands further investigations of the differences between the two analyses: As now understood, former analyses [15] did not use a track-based data sample, but all the hits in the data files. The three noise maps, mentioned in Section 3.1.2, were not used for real data. In the simulation, the random noise and the thermal noise were not set to 0 as described in Section 3.2.2. Furthermore, a continuous function was used [15] instead of the finely binned LVL1A histograms, that are described in this thesis. The exact hit recognition times were written out from the Athena algorithm directly to a log-file, that was then read out afterwards. There is no information about how the fit was performed or about the quality of the fits [15].

The method presented here, for which this thesis should also serve as detailed documentation, is based on tracks. Therefore, it is more noise-immune than [15]. Also, due to the way the fits are performed, it is better suited for a future implementation in the Athena framework.

4.3.2 Method of Minimum TOT

To check the computed TimeZero values, a correlation to a second method was employed. The minimum TOT, that can be measured in the first bin with physics data of a LVL1A distribution, depends on the timing of the Pixel Module as discussed in Section 2.2.3. Therefore, a correlation between the recorded minimum TOT and the computed TimeZero is expected. In Figure 4.26(a), the minimum TOT values are plotted against the calculated TimeZero. No correlation can be observed. Figure 4.26(b) represents only those data pairs for which the LVL1A fits result in a low χ^2. Since typical LVL1A distributions provide no more than four populated bins and there is one fit parameter, the number of degrees of freedom should be three or fewer. Nevertheless, Figure 4.26(b), which contains only those entries with a χ^2 less than 5 and which should therefore include only the best fits, does not show any correlation either.

Even though, the two methods are supposed to give strongly correlated results no correlation can be seen in these plots. The reason is, that the minimum TOT entry is taken from distributions such as 4.1(a). They are highly sensitive to only one entry in a low TOT bin even though this one entry might not be statistically significant. In [25], another method for finding the minimum TOT is discussed, which leads to a clear correlation in data taken with the test setup (Toothpix) in CERN's laboratories.
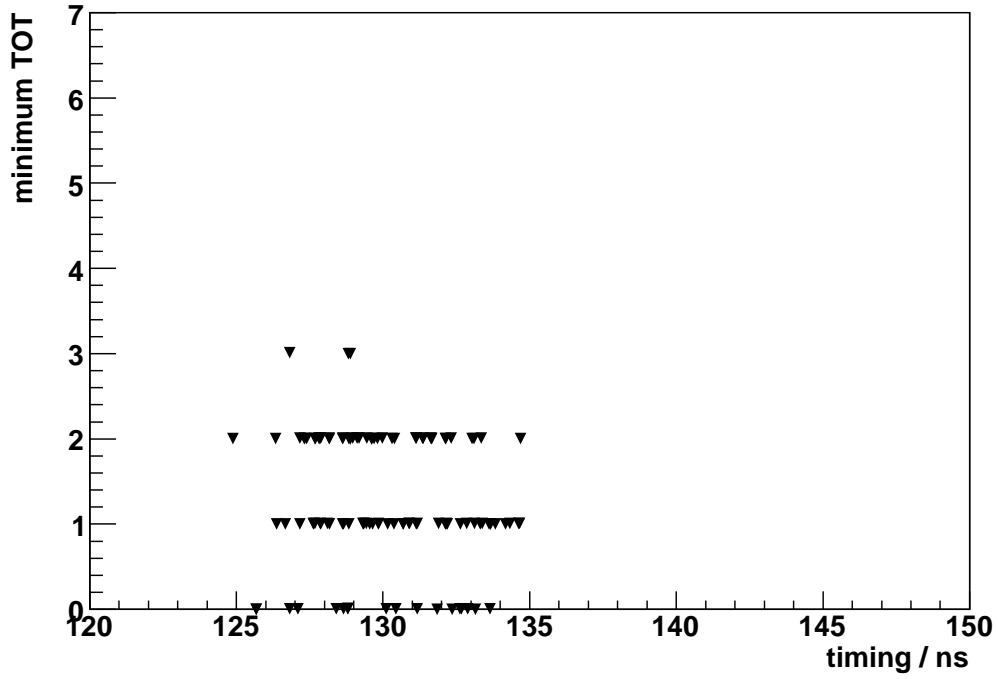
(a) Correlation for all modules.
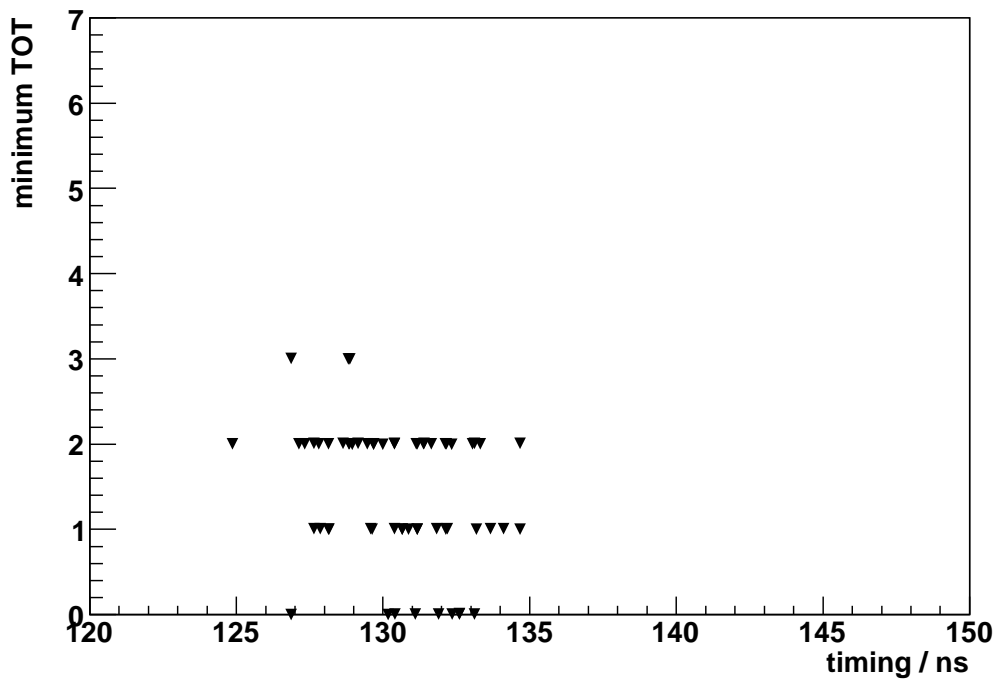
(b) Correlation for modules with $\chi^2 < 5$ in the LVL1A fit.

Figure 4.26: Correlation between TimeZero and minimum TOT.

Chapter 5

Conclusion and Outlook

The subject of this thesis was to determine the timing of the Pixel Modules from the data of the endcap cosmics run in 2006. The starting point has been a previous analysis [15]. As the amount of energy deposited by a particle increases, the signal rises earlier. The effect is strong enough that hits would even be assigned to the following bunch crossing by the Front End electronics. The time, that passes until a high-charge signal rises within a bunch crossing interval, can be adjusted in a device in the readout chain of the Pixel Modules: the Back of Crate card as described in Chapters 4 and 7 of [19]. The adjustment is performed by delaying the BPM decoded clock and the command signal, sent to the modules from the Back of Crate cards, which is possible in steps of 280 ps for each module. So, the ratio of bin entries in the nominal and the next LVL1A window depends on the time that passes until a high-charge signal rises within a bunch crossing interval (the timing). This property can be used, if the digitisation step in the simulation is modified such, that a higher readout frequency is simulated for the Pixel Modules and thus, the simulated LVL1A distribution is more finely segmented. Rebinning this distribution into the nominal 25 ns-wide bins at different points and comparing this to the measured LVL1A distribution results in a timing determination with a precision below 1 ns. The results were compared to the optimum value, that was expected considering the hardware adjustments on the system setup. It was found, that the timing was adjusted in a range of 4 ns around this optimal value of 130 ns (Figure 4.22).

The timing results of the analysis differ from the results that were determined earlier [15] by up to 3 ns. The mean deviation is 1 ns, taking into account the errors of both analyses as weights. Differences in the algorithms employed (mentioned in Section 4.3.1) are most probably responsible for the discrepancies in the results but need further investigation.

The uncertainties presented in this analysis are determined under the assumption that the conversion between the liberated charge Q and the TOT value is exact (the parameters in Equation 4.1). Also, the parameters, that were taken from the calibration database, for calculating the timewalk had to be used as being exact. It was not possible to implement uncertainties at these stages into the software framework, which is worth another investigation. By contrast, the statistics in the simulation and recorded data were included in the calculations.

The anlysis presented here constitutes an important crosscheck of a previously performed analysis [15]. In addition, due to the selection of data based on tracks and the refined fit procedures, it is well suited for a direct implementation into the ATLAS computing framework Athena.

For the future, the method employed and investigated seems to be adequate to determine

the timing from recorded data with a precision far better than the period of the bunch crossing clock, that drives the pixel electronics at 40 MHz. Nevertheless, the determination of the Pixel Module timing requires the reading out of data assigned to two or more consecutive bunch crossings. Due to the low event rate, when working with cosmics, there is no problem in doing so. Difficulties might occur for a data taking of cosmics with the full built-in Pixel Detector in the ATLAS cavern in modules that are aligned vertically. Those modules are located in both the discs and the barrel layers.

Nonetheless, it will be possible to use this method on data from future collision runs, if there are empty clock cycles between the collisions allowing the reading out of several consecutive LVL1A windows per event: this will be the case in the commissioning period of the experiment.

Appendix A

Results from the Analysis

The assignment of module IDs to their coordinates expressed in disc and φ was done with the table `Pixels_Cosmics_IdMapping_3.dat` in the Athena package `InDetCabling` of the Inner Detector. In the data, the module IDs 510932 and 511849 could be found, which do not exist in the software package. Instead, the module IDs 510923 and 510849 exist there. It is assumed, that these are just typing errors. Nevertheless, this was not clarified from the beginning and hence, data from these two modules were not analysed.

Finally, the analysis was run on 112 out of 144 module, where the following 32 modules did not deliver any data in run 1129: 510349, 510398, 510435, 510482, 510498, 510522, 510564, 510705, 510932 (alias 510923), 511807, 511849 (alias 510849), 511910, 512314, 512315, 512694, 512763, 512779, 512797, 512831, 512848, 512867, 512884, 512901, 512902, 512969, 513014, 513017, 513078, 513112, 513119, 513128, 513165. Modules 510853 and 512876 showed a noisy LVL1A distribution with all bins populated, which is typical for a measurement without the high voltage switched on for the Pixel Module. These two modules were also excluded from the analysis. The results of the timing determination are given in the plots and the tables below.
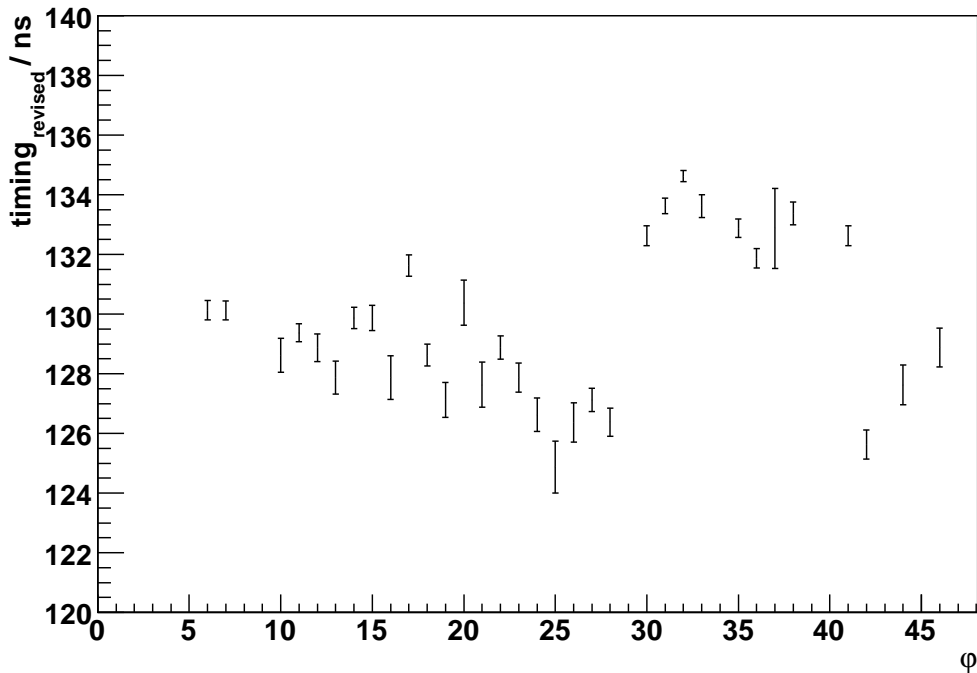

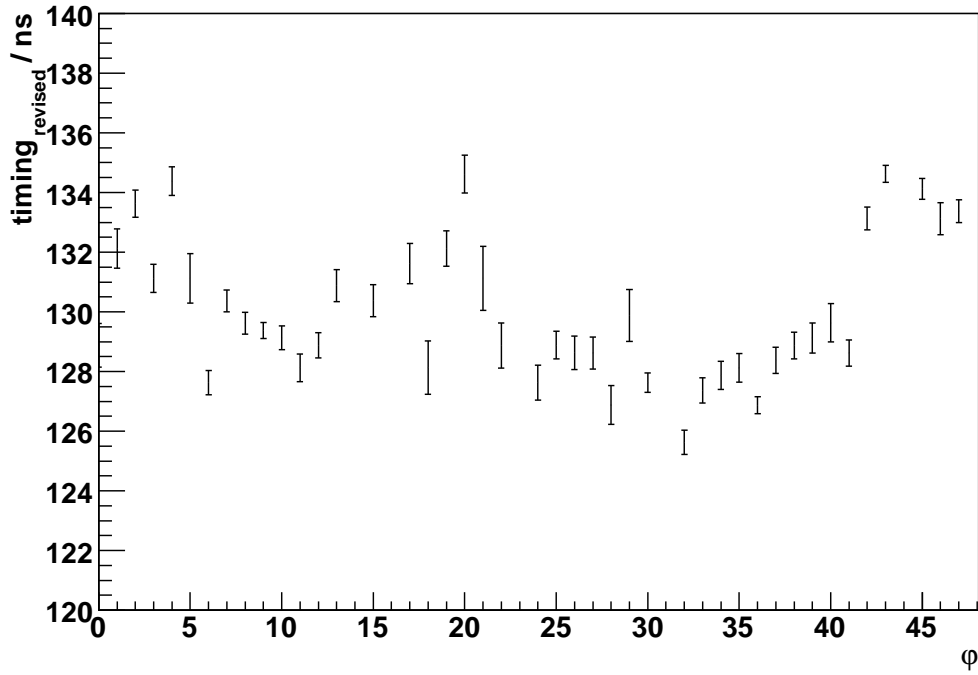**Figure A.1:** Fit results for the Pixel Module timing from the revised algorithm for Disc 0.

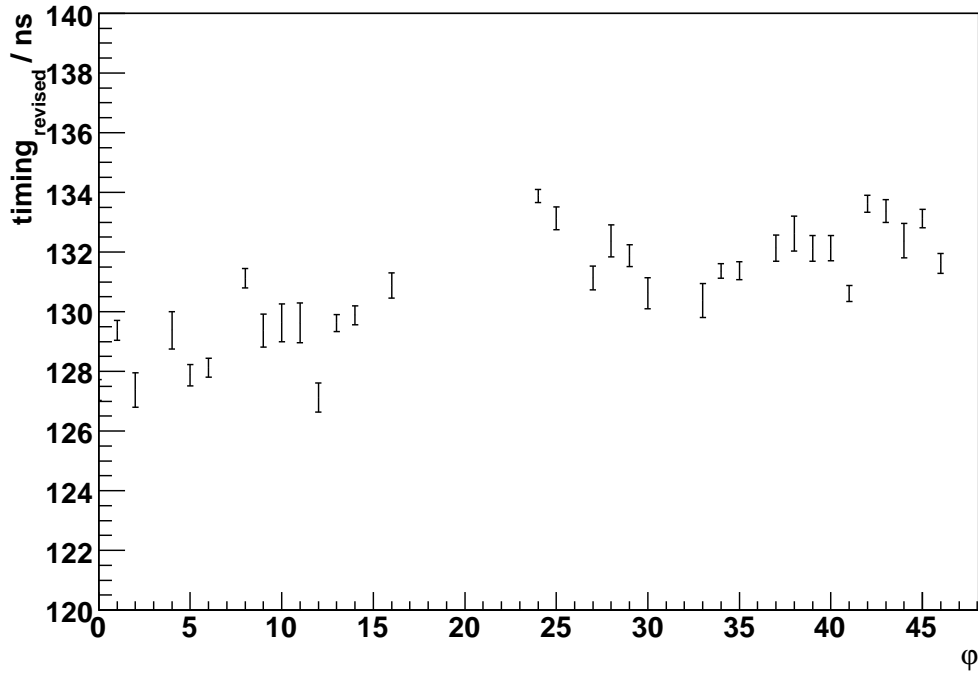**Figure A.2:** Fit results for the Pixel Module timing from the revised algorithm for Disc 1.

Figure A.3: for the Pixel Module timing from the revised algorithm for Disc 2.

φ	Module	timing$_{revised}$ / ns			$\sigma_{\text{par.}}$ / ns	$\sigma_{\text{diff.}}$ / ns	timing$_{Minuit}$ / ns			χ^2	ndf
0	513119										
1	513014										
2	513017										
3	512867										
4	513078										
5	510564										
6	510282	130.13	±	0.32	0.28	0.15	130.13	±	0.76	7.37	3
7	511885	130.12	±	0.32	0.30	-0.07	130.13	±	0.76	3.26	3
8	510349										
9	510849										
10	510418	128.63	±	0.57	0.57	-0.03	128.64	±	0.76	22.77	3
11	510776	129.37	±	0.30	0.27	-0.11	129.40	±	0.75	9.52	3
12	512697	128.88	±	0.46	0.46	0.03	128.85	±	0.77	11.09	3
13	511865	127.88	±	0.55	0.52	0.16	127.87	±	0.76	12.99	3
14	512862	129.87	±	0.36	0.31	0.16	129.90	±	0.75	7.37	3
15	512972	129.88	±	0.42	0.41	-0.06	129.91	±	0.78	1.03	4
16	511876	127.88	±	0.73	0.72	0.07	127.90	±	1.02	9.33	3
17	511251	131.63	±	0.36	0.35	0.03	131.65	±	0.80	5.91	3
18	513103	128.63	±	0.37	0.36	0.06	128.63	±	0.76	4.30	3
19	510541	127.12	±	0.58	0.53	0.22	127.12	±	1.00	3.01	3
20	513155	130.38	±	0.76	0.75	-0.07	130.38	±	0.78	2.56	3
21	511369	127.63	±	0.75	0.74	0.11	127.64	±	1.17	1.74	3
22	510511	128.88	±	0.39	0.34	0.16	128.88	±	0.82	2.46	3
23	511973	127.87	±	0.49	0.48	0.07	127.86	±	0.78	1.69	3
24	511519	126.63	±	0.57	0.52	-0.20	126.63	±	0.87	8.58	4
25	510305	124.88	±	0.87	0.85	0.16	124.88	±	0.79	4.44	3
26	510945	126.38	±	0.66	0.63	0.17	126.38	±	1.00	5.73	3
27	511959	127.12	±	0.40	0.39	0.03	127.14	±	0.76	12.82	4
28	511747	126.38	±	0.48	0.47	-0.06	126.36	±	0.78	10.87	4
29	511910										
30	510409	132.63	±	0.33	0.24	0.22	132.62	±	0.76	2.53	3
31	510254	133.62	±	0.26	0.25	-0.04	133.63	±	0.78	7.99	4
32	510830	134.63	±	0.19	0.17	-0.04	134.63	±	0.76	15.70	5
33	510963	133.63	±	0.38	0.27	-0.26	133.65	±	0.77	11.34	5
34	510853										
35	510389	132.88	±	0.31	0.25	0.16	132.88	±	0.76	5.77	4
36	510354	131.87	±	0.33	0.32	0.03	131.89	±	0.76	1.30	3
37	510889	132.87	±	1.34	1.29	0.34	132.89	±	0.78	11.11	4
38	510490	133.38	±	0.38	0.38	-0.03	133.39	±	0.77	7.12	6
39	510285	133.42	±	94.35	0.04	-94.35	132.12	±	0.85	25.48	4
	510285*	132.12	±	0.33	0.29	0.13	132.12	±	0.85	25.48	4
40	510435										
41	510519	132.63	±	0.34	0.29	-0.16	132.63	±	0.84	5.81	3
42	512846	125.63	±	0.49	0.45	-0.18	125.62	±	0.89	8.70	3
43	512969										
44	512699	127.63	±	0.66	0.54	0.38	127.64	±	0.80	2.23	3
45	512902										
46	512991	128.88	±	0.65	0.64	0.11	128.88	±	0.88	5.50	4
47	512694										

Table A.1: Fit results for Pixel Modules of Disc 0. Module 510285 was reanalysed with an increased number of calls of SEEK (set to 300 instead of 100) in the revised algorithm, since the χ^2-minimum was not found in the first fit run and the parabola was fitted to the wrong χ^2-levels.

φ	Module	timing$_{revised}$ / ns			$\sigma_{\text{par.}}$ / ns	$\sigma_{\text{diff.}}$ / ns	timing$_{Minuit}$ / ns			χ^2	ndf
0	512678	128.88	$\pm$	0.73	0.61	0.40	128.89	$\pm$	0.76	3.93	3
1	512789	132.12	$\pm$	0.66	0.66	0.05	132.11	$\pm$	0.80	0.60	3
2	511802	133.63	$\pm$	0.45	0.43	-0.10	133.63	$\pm$	0.75	2.55	4
3	511965	131.12	$\pm$	0.47	0.39	0.26	131.14	$\pm$	0.76	3.08	3
4	512629	134.38	$\pm$	0.48	0.46	-0.14	134.36	$\pm$	0.78	6.88	3
5	510783	131.13	$\pm$	0.83	0.81	-0.17	131.15	$\pm$	0.78	0.23	3
6	511949	127.63	$\pm$	0.41	0.31	0.26	127.63	$\pm$	0.89	11.64	4
7	511560	130.37	$\pm$	0.37	0.34	-0.12	130.35	$\pm$	0.88	0.65	3
8	512482	129.63	$\pm$	0.36	0.35	-0.05	129.62	$\pm$	1.91	9.95	3
9	512420	129.38	$\pm$	0.27	0.24	0.07	129.40	$\pm$	0.75	10.69	3
10	511469	129.13	$\pm$	0.40	0.38	-0.12	129.10	$\pm$	0.80	0.16	3
11	511060	128.13	$\pm$	0.46	0.45	0.01	128.14	$\pm$	0.82	2.46	3
12	512705	128.88	$\pm$	0.43	0.41	0.07	128.90	$\pm$	0.77	3.68	3
13	512726	130.88	$\pm$	0.53	0.46	0.26	130.88	$\pm$	0.76	3.85	4
14	512831										
15	511655	130.38	$\pm$	0.54	0.53	-0.03	130.37	$\pm$	0.79	2.10	3
16	512797										
17	512792	131.62	$\pm$	0.68	0.67	-0.07	131.62	$\pm$	0.84	2.19	3
18	512350	128.13	$\pm$	0.89	0.87	-0.18	128.12	$\pm$	0.80	7.22	3
19	512690	132.12	$\pm$	0.60	0.52	-0.28	132.13	$\pm$	0.93	4.34	3
20	512564	134.62	$\pm$	0.63	0.62	-0.09	134.66	$\pm$	0.83	2.20	3
21	512676	131.13	$\pm$	1.07	1.07	-0.04	131.12	$\pm$	0.82	0.30	2
22	513071	128.88	$\pm$	0.76	0.72	0.23	128.88	$\pm$	1.09	0.43	2
23	512779										
24	512455	127.63	$\pm$	0.58	0.58	0.03	127.62	$\pm$	0.97	7.32	3
25	512835	128.88	$\pm$	0.46	0.46	-0.02	128.84	$\pm$	0.77	2.82	3
26	512469	128.63	$\pm$	0.56	0.55	-0.07	128.63	$\pm$	0.78	6.35	5
27	512711	128.63	$\pm$	0.54	0.53	0.01	128.65	$\pm$	0.77	12.31	4
28	512452	126.88	$\pm$	0.65	0.44	0.47	126.88	$\pm$	0.75	2.54	3
29	512594	129.88	$\pm$	0.87	0.65	0.58	129.86	$\pm$	0.81	8.56	3
30	512501	127.63	$\pm$	0.33	0.32	-0.01	127.64	$\pm$	0.81	9.54	4
31	511807										
32	512343	125.63	$\pm$	0.40	0.39	0.07	125.62	$\pm$	1.06	12.12	3
33	512351	127.37	$\pm$	0.43	0.38	0.18	127.37	$\pm$	0.89	5.01	3
34	511476	127.88	$\pm$	0.47	0.27	0.38	127.87	$\pm$	0.75	11.09	4
35	511559	128.12	$\pm$	0.48	0.47	0.06	128.13	$\pm$	0.78	1.81	3
36	512374	126.87	$\pm$	0.28	0.23	0.15	126.88	$\pm$	0.76	4.27	3
37	512661	128.37	$\pm$	0.44	0.36	-0.23	128.38	$\pm$	0.77	19.11	4
38	512493	128.87	$\pm$	0.45	0.45	0.03	128.85	$\pm$	0.88	5.19	4
39	512951	129.13	$\pm$	0.51	0.45	0.22	129.10	$\pm$	0.77	19.01	3
40	512383	129.63	$\pm$	0.64	0.62	0.16	129.62	$\pm$	0.78	2.19	4
41	513038	128.62	$\pm$	0.44	0.43	0.05	128.64	$\pm$	0.87	11.58	3
42	512746	133.13	$\pm$	0.39	0.37	-0.11	133.12	$\pm$	0.76	2.91	3
43	512750	134.62	$\pm$	0.29	0.21	-0.18	134.64	$\pm$	0.89	4.72	4
44	512763										
45	512733	134.13	$\pm$	0.35	0.34	0.03	134.12	$\pm$	0.85	4.72	4
46	512686	133.12	$\pm$	0.54	0.50	0.20	133.09	$\pm$	1.01	3.00	4
47	512786	133.38	$\pm$	0.38	0.37	-0.07	133.38	$\pm$	0.84	1.75	3

Table A.2: Fit results for Pixel Modules of Disc 1.

φ	Module	timing$_{revised}$ / ns			$\sigma_{\mathrm{par.}}$ / ns	$\sigma_{\mathrm{diff.}}$ / ns	timing$_{Minuit}$ / ns			χ^2	ndf
0	510421	127.38	$\pm$	0.36	0.35	0.05	127.38	$\pm$	0.76	11.89	3
1	510943	129.37	$\pm$	0.34	0.28	-0.17	129.41	$\pm$	0.75	0.50	3
2	510160	127.38	$\pm$	0.58	0.57	-0.03	127.37	$\pm$	0.75	4.01	3
3	510482										
4	510365	129.38	$\pm$	0.63	0.62	-0.05	129.39	$\pm$	0.75	5.14	4
5	510651	127.88	$\pm$	0.36	0.34	0.10	127.87	$\pm$	0.76	3.74	3
6	510540	128.13	$\pm$	0.31	0.28	0.13	128.12	$\pm$	0.76	3.87	3
7	510398										
8	510787	131.12	$\pm$	0.32	0.27	-0.17	131.13	$\pm$	0.76	4.47	3
9	510518	129.37	$\pm$	0.55	0.54	0.07	129.40	$\pm$	0.75	11.28	4
10	510946	129.63	$\pm$	0.63	0.59	0.22	129.62	$\pm$	0.77	2.88	3
11	510155	129.63	$\pm$	0.67	0.65	0.14	129.60	$\pm$	0.77	3.84	3
12	510392	127.12	$\pm$	0.49	0.47	0.14	127.14	$\pm$	0.77	9.80	4
13	510837	129.63	$\pm$	0.28	0.26	0.09	129.62	$\pm$	0.79	4.32	3
14	510944	129.88	$\pm$	0.32	0.24	0.21	129.88	$\pm$	0.75	5.12	3
15	510705										
16	510900	130.88	$\pm$	0.42	0.37	0.18	130.88	$\pm$	0.92	14.80	3
17	510522										
18	512884										
19	512848										
20	512315										
21	512314										
22	513165										
23	513112										
24	513091	133.88	$\pm$	0.22	0.20	-0.06	133.88	$\pm$	0.76	15.35	6
25	510464	133.13	$\pm$	0.38	0.35	-0.12	133.11	$\pm$	0.77	2.26	5
26	512901										
27	511818	131.12	$\pm$	0.40	0.39	0.05	131.12	$\pm$	0.77	4.19	4
28	510366	132.37	$\pm$	0.54	0.52	-0.13	132.38	$\pm$	0.88	2.33	3
29	511945	131.87	$\pm$	0.37	0.35	-0.10	131.89	$\pm$	0.76	2.58	4
30	513169	130.62	$\pm$	0.52	0.50	0.13	130.62	$\pm$	0.79	4.18	4
31	513128										
32	512876										
33	513111	130.38	$\pm$	0.57	0.57	-0.03	130.41	$\pm$	0.77	2.18	3
34	512961	131.37	$\pm$	0.24	0.23	-0.05	131.38	$\pm$	0.80	2.62	3
35	511357	131.37	$\pm$	0.30	0.29	-0.08	131.39	$\pm$	0.75	2.31	3
36	510923										
37	511665	132.12	$\pm$	0.44	0.43	-0.03	132.14	$\pm$	0.87	2.32	4
38	512950	132.62	$\pm$	0.58	0.43	-0.39	132.63	$\pm$	0.77	2.36	4
39	510781	132.12	$\pm$	0.43	0.42	-0.10	132.12	$\pm$	0.76	0.64	3
40	510680	132.13	$\pm$	0.42	0.41	-0.07	132.19	$\pm$	0.77	6.20	5
41	512429	130.62	$\pm$	0.27	0.20	0.16	130.63	$\pm$	0.83	1.91	3
42	510346	133.62	$\pm$	0.28	0.18	-0.21	133.64	$\pm$	0.75	11.94	4
43	510461	133.38	$\pm$	0.38	0.35	0.14	133.38	$\pm$	0.76	10.64	3
44	510559	132.38	$\pm$	0.57	0.56	0.07	132.38	$\pm$	0.92	2.61	3
45	510513	133.13	$\pm$	0.31	0.25	-0.17	133.13	$\pm$	0.76	4.77	4
46	510311	131.62	$\pm$	0.34	0.30	-0.14	131.62	$\pm$	0.76	5.37	3
47	510498										

Table A.3: Fit results for Pixel Modules of Disc 2.

List of Figures

Bibliography

[1] CERN, *LHC Project Homepage*, June 2008, `http://lhc.web.cern.ch/lhc/`.

[2] Y. Baconnier, G. Brianti, P. Lebrun, A.G. Mathewson, R. Perin, *LHC: The Large Hadron Collider Accelerator Project*, CERN, 1993.

[3] O.S. Brüning, P. Collier, P. Lebrun, S. Myers, R. Ostojic, J. Poole, P. Proudlock, *LHC Design Report*, CERN-0000024513, 2004.

[4] ATLAS Collaboration, *ATLAS: Letter of Intent for a general-purpose pp Experiment at the Large Hadron Collider at CERN*, Letter of Intent, CERN-LHCC-92-004, 1992.

[5] ATLAS Collaboration, *ATLAS Pixel Detector Technical Design Report*, Technical Design Report ATLAS, CERN/LHCC 98-13, 1998.

[6] W.-M. Yao et al., *Review of Particle Physics*, Journal of Physics G, *vol. 33*, 2006:1+, `http://pdg.lbl.gov`.

[7] see e.g.: D. W. Perkins, *Hochenergiephysik*, Addison-Wesley, München, 1990, and the references therein.

[8] see e.g.: M. E. Peskin, D. V. Schroeder, *An Introduction to Quantum Field Theory*, Westview Press, Boulder, Colo., 2004, and the references therein.

[9] ATLAS Collaboration, *ATLAS Detector and Physics Performance II: Technical Design Report*, Technical Design Report ATLAS, CERN/LHCC/99-15, 1999.

[10] P. Teixeira-Dias on behalf of The LEP Higgs Working Group, *Higgs Boson Searches at LEP*, arXiv:0804.4146v1, April 2008.

[11] see e.g.: C. Grupen, *Astroparticle Physics*, Springer, Berlin, Germany; New York, U.S.A., 2005, and the references therein.

[12] M. Keil, *Pixeldetektoren aus Silizium und CVD-Diamant zum Teilchennachweis in ATLAS bei LHC*, Ph.D. thesis, Universität Bonn, October 2001, BONN-IR-2001-13, CERN-THESIS-2007-035.

[13] see e.g.: C. Grupen, *Teilchendetektoren*, BI-Wissenschaftsverlag, Mannheim, 1993, and the references therein.

[14] K. Einsweiler, *private communication*, 2007.

[15] F. de Lorenzi, *Timing Characteristics of the ATLAS Pixel Detector*, Università Degli Studi Di Milano, 2007.

[16] ATLAS Pixel Collaboration, *Pixel Offline Analysis for EndcapA Cosmic Data*, December 2007.

[17] ATLAS Collaboration, *The ATLAS Experiment at the CERN Large Hadron Collider*, submitted to JINST, 2008.

[18] ATLAS Collaboration, *ATLAS Detector and Physics Performance I: Technical Design Report*, Technical Design Report ATLAS, CERN/LHCC/99-14, 1999.

[19] T. Flick, *Studies on the Optical Readout for the ATLAS Pixel Detector*, Ph.D. thesis, Universität Wuppertal, July 2007.

[20] M. Moll, *Radiation Damage in Silicon Particle Detectors - Microscopic Defects and Macroscopic Properties*, Ph.D. thesis, Universität Hamburg, 2007.

[21] M. Garcia-Sciveres, *The ATLAS Pixel Detector*, *Tech. rep.*, March 2003, from Pixel 2002 conference, Carmel, California, USA, 9-12 Sept. `http://pixel2002.lbl.gov/` Proceedings have been published in `http://www.slac.stanford.edu/econf/`.

[22] D. Dobos, C. Gössling, and R. Klingenberg, *Commissioning Perspectives for the ATLAS Pixel Detector*, Ph.D. thesis, Universität Dortmund, September 2007.

[23] F. Hügging, *Der ATLAS Pixelsensor*, Ph.D. thesis, Universität Dortmund, June 2001, CERN-THESIS-2001-027, http://hdl.handle.net/2003/2350.

[24] K. Einsweiler, *ATLAS On-detector Electronics Architecture*, LBNL, 2003, draft V3.0.

[25] M. Köhler, *Studies of the Timing Behaviour of the ATLAS Pixel Detector*, Universität Siegen, August 2008.

[26] J. Colas, M. Pripstein, W. A. Wenzel, *The Electrostatic Transformer*, Nuclear Instruments and Methods in Physics Research A, *vol. 294*, 1990:583–590.

[27] J. Wotschack, *ATLAS Muon Chamber Construction Parameters for CSC, MDT, and RPC chambers*, *Tech. rep.*, April 2008, back-up document for the ATLAS Detector Paper.

[28] ATLAS Collaboration, *ATLAS Level-1 Trigger Technical Design Report*, Technical Design Report ATLAS, CERN/LHCC/98-14, 1998.

[29] T. Pauly et al., *Pixel Data Taking Log*, December 2006, `https://twiki.cern.ch/twiki/bin/view/Atlas/PixelDataTakingLog`.

[30] ATLAS Pixel Collaboration, *Cosmics run 1129 data files*, December 2006, `/castor/cern.ch/atlas/testbeam/pixel/2006/daq_Appl_PixelEB01_daqdev2_0001129_fileNN.data` with NN = 01 to 12.

[31] S. Lloyd et al., *The ATLAS Computing Workbook*, February 2008, `https://twiki.cern.ch/twiki/bin/view/Atlas/WorkBook`, version r114, ATLAS TWiki.

[32] G. Folger, G. Cosmo, *Geant4*, 2002.

[33] M. Zdrazil et al., *How to Run Pixel EndCap C Cosmics Simulation*, May 2007, `https://twiki.cern.ch/twiki/bin/view/Atlas/HowToRunPixelEndCapCCosmicSimulation`, ATLAS TWiki.

[34] A. Andreazza et al., *How to Run Pixel EndCap C Cosmics Reconstruction*, May 2007, `https://twiki.cern.ch/twiki/bin/view/Atlas/HowToRunPixelEndCapCCosmicReconstruction`, ATLAS TWiki.

[35] D. Constanzo, G. Gorfine, *PixelGeoModel package documentation on ATLAS TWiki pages*, May 2005, `https://twiki.cern.ch/twiki/bin/view/Atlas/PixelGeoModel`, ATLAS TWiki.

[36] M. Gallas, A. Dell'Acqua et al, *GEANT4 ATLAS detector Simulation Applications*, October 2006, `http://atlas-computing.web.cern.ch/atlas-computing/packages/simulation/geant4/G4AtlasApps/doc/index.html`, ATLAS TWiki.

[37] O. Oye et al., *InDetCosmicSimAlgs simulation package documentation on ATLAS TWiki pages*, June 2005, `https://twiki.cern.ch/twiki/bin/view/Atlas/InDetCosmicSimAlgs`, ATLAS TWiki.

[38] R. Brun, F. James, *TMinuit*, March 2008, `http://root.cern.ch/root/html/TMinuit.html`.

[39] ATLAS Pixel Collaboration, *Pixel Offline Calibrations, Connectivity and Conditions Database*, November 2007, `https://twiki.cern.ch/twiki/bin/view/Atlas/PixelCOOLoffline#Calibrations`.

[40] F. James, *MINUIT - Function Minimization and Error Analysis v94.1*, August 1998.

[41] F. James, *The Interpretation of Errors*, June 2004.

[42] F. James, M. Winkler, *Minuit User's Guide*, June 2004.

Acknowledgements

Erklärung

Hiermit erkläre ich, daß ich die vorliegende Masterarbeit selbständig verfaßt und keine anderen als die angegebenen Quellen und Hilfsmittel benutzt, sowie Zitate und Ergebnisse anderer kenntlich gemacht habe.

Siegen, Donnerstag, den 21. August 2008   Unterschrift: